PRECURSORY VOLCANIC ACTIVITY AND CULTURAL RESPONSE TO THE LATE BRONZE AGE ERUPTION OF SANTORINI (THERA), GREECE

A THESIS SUBMITTED TO THE GRADUATE DIVISION OF THE UNIVERSITY OF HAWAIʻI AT MĀNOA IN PARTIAL FULFILLMENT OF THE REQUIREMENTS FOR THE DEGREE OF

MASTER OF SCIENCE
IN
GEOLOGY AND GEOPHYSICS

MAY 2020

By
Krista Jaclyn Evans

Thesis Committee:

Floyd W. McCoy, Chairperson
Bruce Houghton
Robert Littman

Acknowledgements

Thank you to my advisor, committee chair, and mentor, Dr. Floyd McCoy, for his support and dedication for the completion of this project. Dr. McCoy has pushed me to attend several conferences which has led to a press conference at AGU's Fall 2019 meeting. I am truly grateful to him for making me a better student and scientist. I have learned a lot from Dr. McCoy and hope to continue working with him in the future.

My committee members, Drs. Bruce Houghton and Robert Littman have been truly gracious and generous with their time during the development of this work. Bruce has especially contributed not only as part of my committee, but through his classes and field trips.

Laboratory processing was done on both the Manoa and Windward campuses of the University of Hawaii. At the latter campus, Lisa Hayashi is thanked for her assistance and help. Laboratory work in Greece was accomplished at the INSTAP Center for East Crete, courtesy of Dr. Tom Brogan, Director. Dr Thomas Shea, at the University of Hawaii, allowed me to use his picking scope to look at some of the samples when it came to the componentry, for which I extremely thankful.

Field permits were provided by the Institute of Geology and Mineral Exploration (IGME). Field efforts on Thera were aided by Professor Paraskevi Nomikou, University of Athens, and two undergraduate students, Nerissa Barling and Christine Colvin. The fieldwork and collection of samples would not have gone as smoothly without them and it was a privilege to share this experience with them.

Thank you to my parents' continued love and support. If it were not for them and the cruise they took me on so many years ago, I do not think I would be working on this thesis. They have supported my every decision in life and have pushed me to reach for my dreams. I would also like to thank the rest of my family and friends for their never-ending love and support. And a special thanks goes to my fluff ball, Princess Zoey, for conducting her role as an emotional support animal well and keeping me sane throughout this entire process.

Abstract

The Late Bronze Age (LBA) eruption (*ca.* 1650 B.C.) of Thera (Santorini) was one of the largest known in history, burying and destroying a thriving Theran culture that occupied the island and surrounding islands. The consequent thick tephra deposit provides detailed information on the eruptive sequence and vent mechanics – it also provides details on that culture through burial of towns, farmsteads, and landscapes, the most prominent being the town of Akrotiri on the south coast of Thera. Here stratigraphic relationships between volcanic and archaeological deposits/constructions clearly indicate this eruption was signaled by seismic and minor eruptive events precursory to the main Plinian eruption. Because no casualties have yet been found beneath the tephra, inhabitants had advance notice of the impending diaster by a precursory eruption whose deposits are well preserved both within the archaeological site and in geological exposures throughout southern Thera island – and escaped by boat. Yet archaeological sites on nearby islands rarely record an influx of new arrivals at the time of the eruption. Accordingly, it is suggested here that those escaping were incinerated at sea by pyroclastic density currents (PDCs) that traversed across the ocean surface during the second phase of the catastrophic eruption.

Table of Contents

List of Figures

List of Tables

1.0 Introduction

Precursory phenomena frequently provide advance warning of explosive volcanic eruptions via tectonic and landscape disruptions, effusive volcanic activity, seismicity, and alterations to existing geothermal systems. Today, such phenomena are used as predictive indicators of impending eruptions and as advance warnings for societal consideration and response. Yet, in the historic past, precursory volcanic activity was not understood (Pompeii, A.D. 79), ignored (Krakatau, 1883), or disregarded by political dictate (St. Pierre, 1903).

In antiquity, the Southern Aegean witnessed one of the largest volcanic eruptions in history when Santorini erupted. Precursory activity preceding this catastrophic Plinian eruption stimulated wholescale evacuation of inhabitants from the island. In a matter of hours to days, Santorini discharged a large quantity of gas-charged silicic magma, burying a contemporary town and landscape, and sending ash, aerosols and tsunamis across the Eastern Mediterranean region. At the time, Santorini was a wealthy maritime trading port, blessed with fertile soil and sheltered harbors such as at Akrotiri on the southern coast. Since its discovery by Spyridon Marinatos in 1967, archaeological excavations have revealed a wealth of stunning frescos, multi-story houses and buildings, an advanced sanitation system, and a rich assortment of household goods that suggests an advanced culture. Akrotiri is a prehistoric town, frozen at a moment in time, preserved and destroyed by one of the most cataclysmic events in volcanology, and is one of the most important archaeological sites in the world. Continuous archaeological excavations have not yet uncovered victims from this disaster at either Akrotiri or at other towns and farmsteads. The inference is that (a) the precursory activity was so unusual and intense, the inhabitants were adequately stunned and left; and (b) the precursory activity continued almost unabated into the main catastrophic eruption, not allowing wholescale return and reoccupation of the island, though some residents returned but left again immediately prior, or during, the opening phase of the main eruption. Excellent geoarchaeological and tephra chronological records at the archaeological site provides a basis for reconstructing the events of this eruption and its consequences to ancient culture.

Volcanic eruptions can leave evidence that allows reconstruction of eruptive histories and inferences for future activity. The objective of this thesis focuses applying both the geological and

archaeological aspects on the Late Bronze Age (LBA) eruptive chronology and cultural response. This thesis is separated into two sections, the first section describes the eruption dynamics during each phase of the precursory activity. The second section of this thesis deduces the response of the Theran culture to the precursory phenomena, a chronology of events during the precursory through the catastrophic eruption, and the cultural response to the catastrophic eruption. Included in this second part, this thesis proposes an answer to the question of what happened to Theran evacuees after they left Santorini, since archaeological evidence on nearby islands indicates no population increase at the time of the eruption.

2.0 Background

2.1 Tectonic and Geologic Setting

Santorini is an active volcanic complex consisting of five islands located in the southern Aegean Sea, 120 km north of Crete (**Figure 1**). Santorini is one of several volcanic centers active during the Quaternary along the Hellenic Volcanic Arc (HVA). The islands of Thera, Therasia, and Aspronisi form a partial ring around a flooded caldera with two central islands, where contemporary volcanic activity is concentrated, Nea Kameni and Palea Kameni (**Figure 1**). Thera, Therasia, and Aspronisi are remnants of one large island, Stronghyle, destroyed during the LBA eruption.

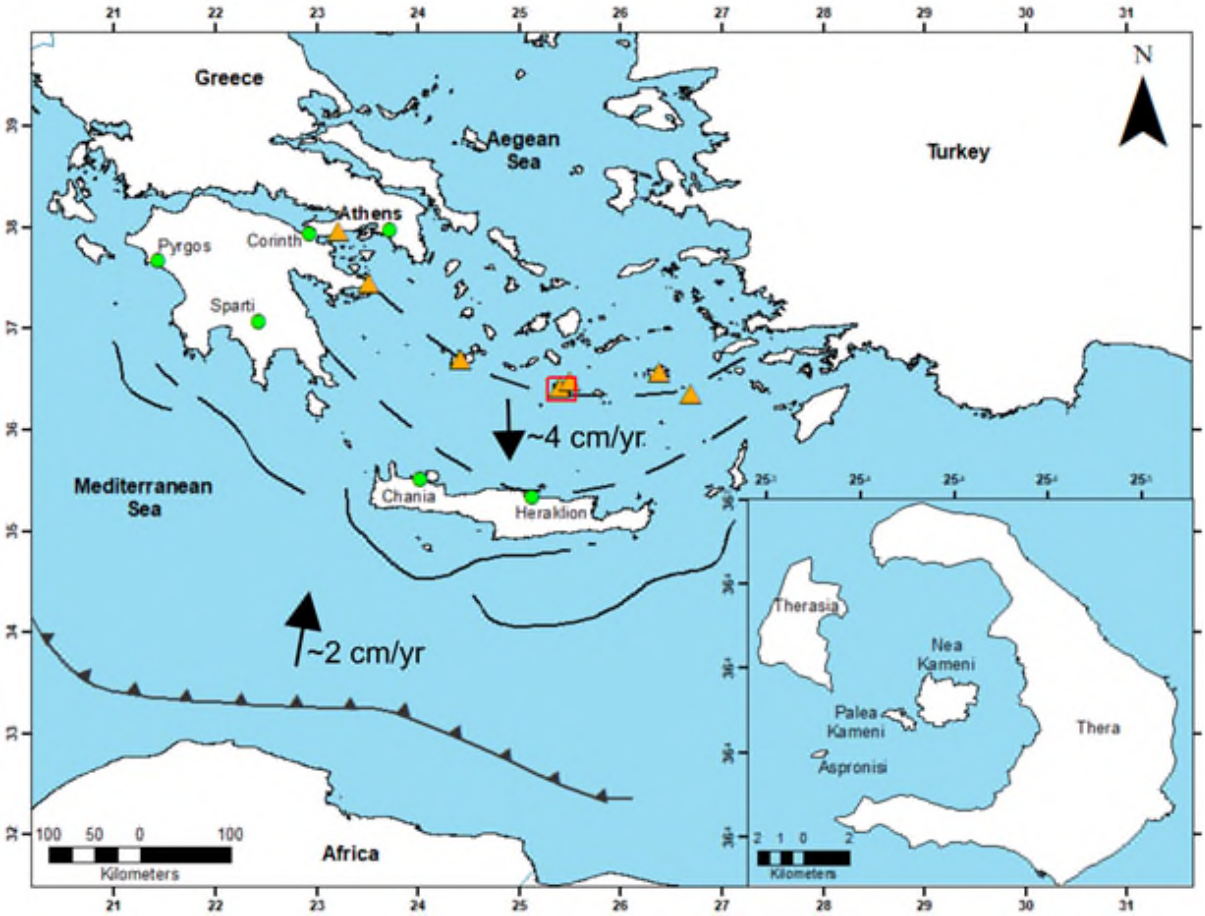

Figure 1 Tectonics of the southern Aegean and eastern Mediterranean Seas. Line with sawtooth pattern traces the approximate position at the sea floor of the down-going slab; solid black lines delineate linear sea-floor troughs (Hellenic "trench" system); and the dashed lines denote the forearc and back arc island chains with the northern most being the Hellenic Volcanic Arc (HVA). The orange triangles indicate the volcanic centers on the HVA. Inset shows Santorini.

2.1.1 Tectonic Activity

The Aegean Sea is located at the convergence of the Aegean and African tectonic plates. The Aegean, including part of mainland Greece, Crete, Rhodes, and western Turkey, is situated on the small, southerly moving Aegean microplate (McKenzie 1970; Jackson 1994; Druitt et al. 1999). The HVA formed in response to the northward motion of the African plate beneath the Aegean plate which began 13-16 Ma (**Figure 1**: Angelier et al. 1982; Mercier et al. 1989). Current plate closure rate of Africa relative to the southwest Aegean is 35 mm/yr (Piper and Perissoratis 2003) which led to the formation of a Benioff seismic zone down to the depth of approximately 100-200 km (Dimitriadis et al. 2009). Consequent extension of the Aegean plate began in the Upper Miocene (Druitt et al. 1999) with the Aegean marine basin forming during the Pliocene in response to this stretching and foundering (Higgins and Higgins 1996). Average regional crustal thinning and extension since the early Miocene has been of the order of 20 mm/yr with Quaternary rates of 40-50 mm/yr.

Five volcanic centers characterized by explosive eruptions, Santorini, Milos, Kos, Nisyros, and Yali, are situated along the HVA (**Figure 1**). Two main phases of volcanism are recognized: Oligocene to mid-Miocene, and a second pulse starting in the late Pliocene and continuing to the present (Fytikas et al. 1984). Explosive volcanism, dating to approximately 200,000 years ago, characterized the eastern sector of the HVA. A major explosive unit, the Kos Plateau Tuff, contains ignimbrites covering several Aegean islands and western Turkey with a total estimate volume greater than 100 km^3 (Keller et al. 1990). The Kos eruption is dated to 145,000 ± 5,000 years BP. Of significant interest is the eruption of pyroclastic density currents (PDCs) crossing open stretches of sea (Keller et al. 1990).

Nisyros is a caldera volcano with many similarities to Santorini, although smaller in size. The island of Nisyros is composed exclusively of Quaternary volcanic rocks with alternating lava flows, pyroclastic layers, and lava domes, ranging in age from 200 to 25 ky (Nomikou 2003). No major explosive volcanic activity is known to have occurred on the island after the formation of the domes for at least 25,000 years, although there may have been a minor eruption here in the Neolithic. Violent earthquakes, gas detonations, steam blasts, and mudflows accompanied hydrothermal eruptions in the late 1871-1873 and 1887 (Nomikou 2003).

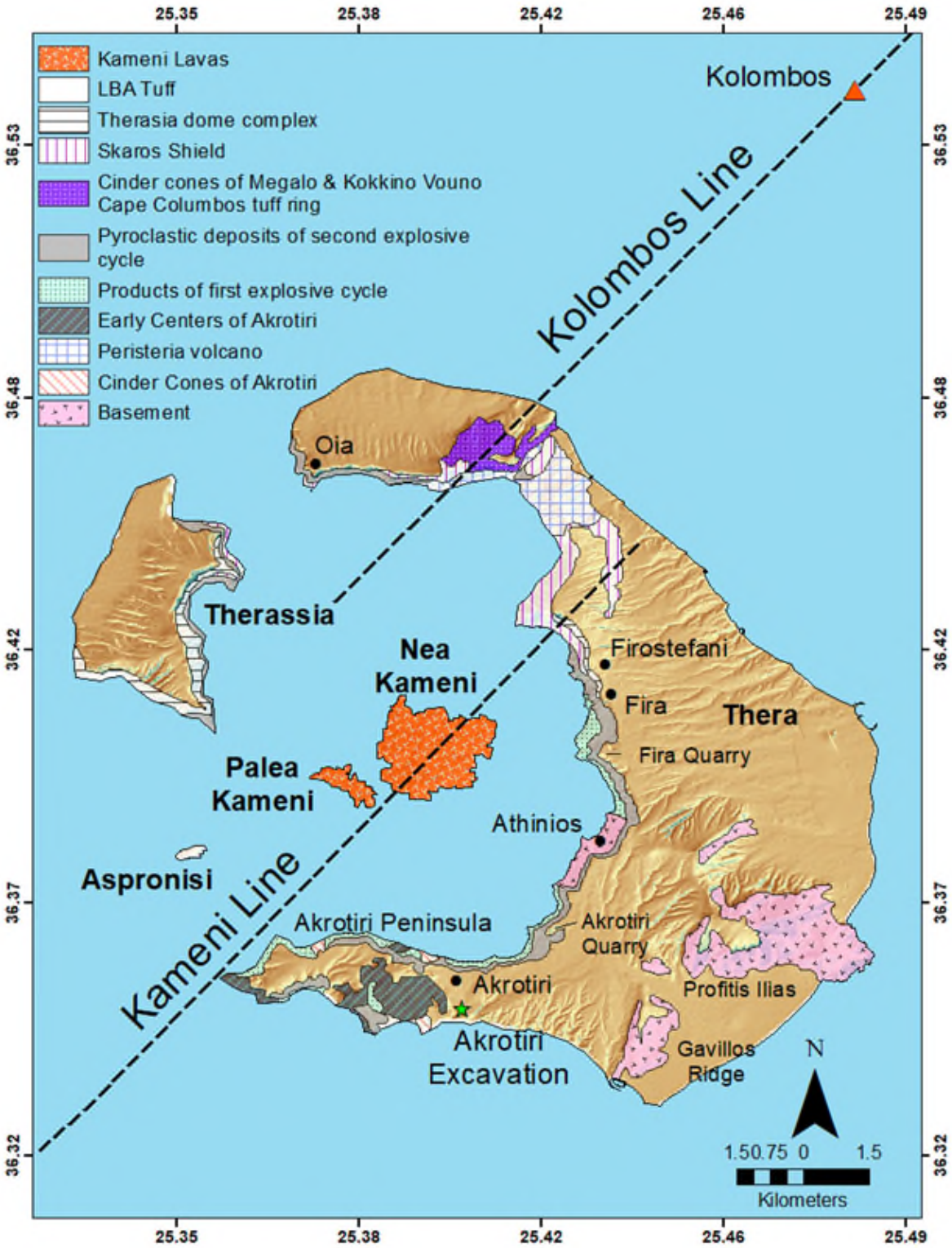

Figure 2 Geology of Santorini. The two NE-SW tectonic lineaments, Kameni and Kolombos Lines, strongly influences volcanic activity at Santorini. The submarine volcano, Kolombos, lies on the Kolombos line to the northeast of Santorini. This is a simplified geological map of Santorini based on Druitt et al. (1999). Basemap DEM from Paraskevas et al. (2019).

In the Santorini volcanic field, the Santorini-Amorgos Fault Zone is the main tectonic feature with

an ENE-WSW trend (Dimitriadis et al. 2009). This fault zone produced the two largest earthquakes in the central Aegean region during the 20th century, which occurred within 13 minutes of each other on July 9, 1956 (Dimitriadis et al. 2009).

Volcanic activity at Santorini and perhaps the siting of this volcanic field is strongly influenced by two NE-SW tectonic lineaments, the Kameni and Kolombos Lines. Nea Kameni and Palea Kameni are located on the Kameni Line (**Figure 2**). The highly active submarine Kolombos volcano northeast of Santorini is located on the Kolombos Line, which cuts through the cinder cones of Megalo Vouno and Kokkino Vouno as well as the Cape Columbos tuff ring (Vespa et al. 2006; **Figure 2**).

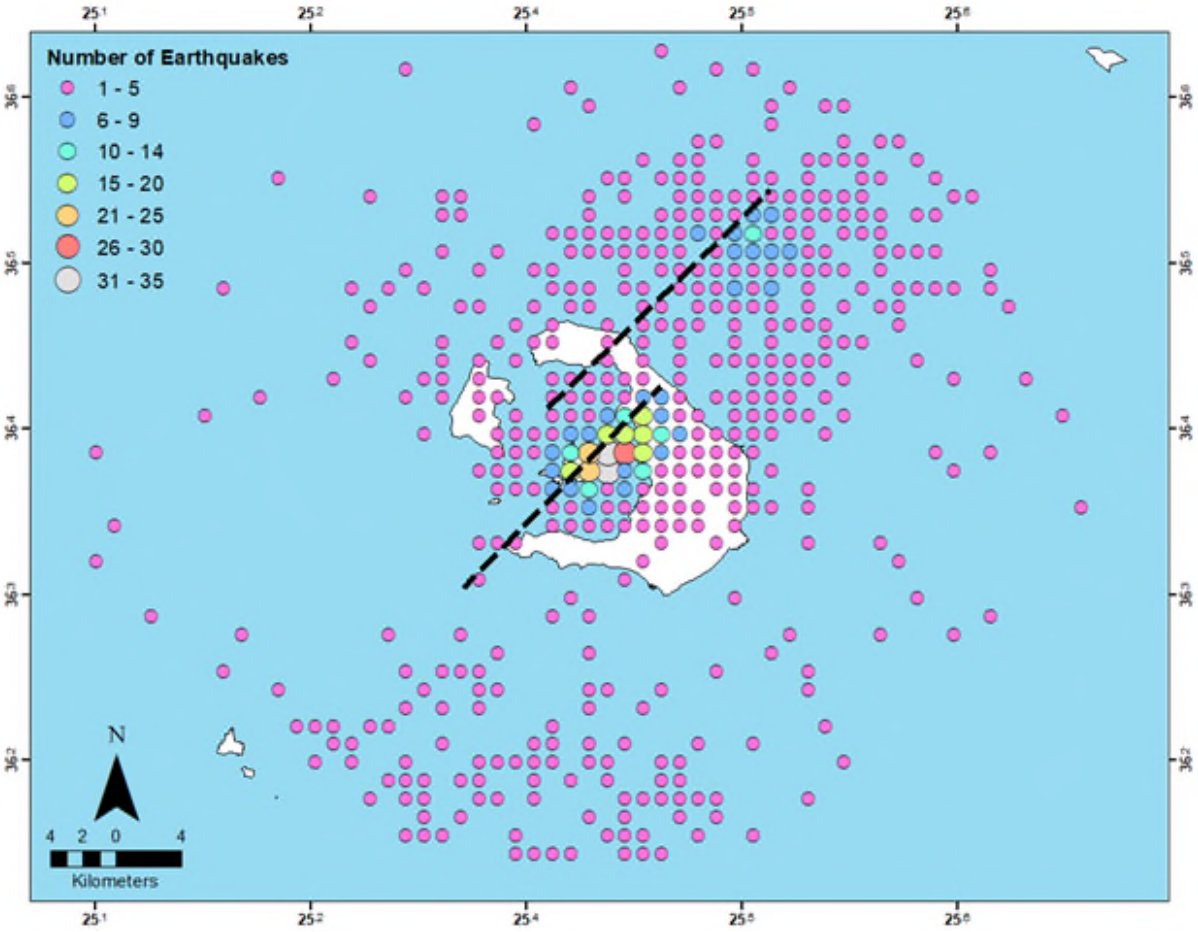

Figure 3 Earthquakes around Santorini. Approximately 1,221 earthquakes have been recorded between January 1968 and February 2020. The magnitude of these earthquakes range between 0.1 and 5.0 on the Richter Scale. The black dashed lines indicate the Kameni and Kolombos lineaments.

The Aegean and Mediterranean regions, including Santorini, are currently and have been seismically active since the Miocene. Approximately 1,221 earthquakes have been recorded

within a 25-km radius of the center of the caldera between 1968 and January 2020 (**Figure 3**). These earthquakes range in magnitude between 1 and 5 on the Moment Magnitude Scale with 209 of these earthquakes having magnitude 3 or higher. During a period of volcanic unrest at Santorini in 2011-2012, approximately 723 earthquakes were recorded ranging in magnitude between 0.2 and 3.5 (**Table 1**).

Thus, it is clear this region was seismically active during the LBA. Clearly local inhabitants in this region are familiar with seismicity and its effects, also indicated by repeated rebuilding from earthquake damage and repairs to buildings from the Neolithic through the LBA time span of the ancient settlement at Akrotiri (Doumas 1978, 1983; Palyvou 1984; Marthari 1990) and also in modern times.

Table 1 Earthquakes recorded within a 25-km radius of the center of the Santorini caldera between 1968 and 2020, including the 723 earthquakes recorded during the period of volcanic unrest in 2011-2012.

Magnitude	Year Range	Number of Earthquakes
0.1-1.0	2011-2014	111
1.0-2.0	2011-2019	593
2.0-3.0	2003-2019	308
3.0-4.0	1968-2019	194
4.0-5.0	1970-2009	15

2.1.2 Volcanic Stratigraphy of Santorini

The Santorini archipelago is composed of Pleistocene to Recent volcanic rocks (Pichler and Kussmaul 1980; Druitt et al. 1999) mantling a Mesozoic metamorphic basement of low-grade metapelites (schists and phyllites) and crystalline limestones (Druitt et al. 1999). Forming two basement massifs, Mount Profitis Ilias and Gavrillos Ridge on southeast Thera, these protruding peaks of an island that existed prior to modern volcanism and the submarine seafloor volcanics of the Akrotiri Peninsula (**Figure 2**). The metapelites are also exposed along a 2 km stretch of the caldera wall near Athinos, where it has been exhumed by caldera collapse, and in a topographic saddle between Profitis Ilias and Mesa Vouno (Pichler and Kussmaul 1980; Druitt et al. 1999; Vespa et al. 2006). Metalimestones form the massifs of Profitis Ilias, Mesa Vouno, and Gavrillos.

Volcanic activity of Santorini started with the formation of submarine lavas and cinder cones approximately 600 ka ago (Druitt et al. 1999; Vespa et al. 2006), now covered by a sequence of later Plinian pyroclastic deposits which in places exceeds a thickness of 200 m (**Figure 2**; Druitt et al. 1999). These deposits also drape over the basement massif and dominate the cliffs of

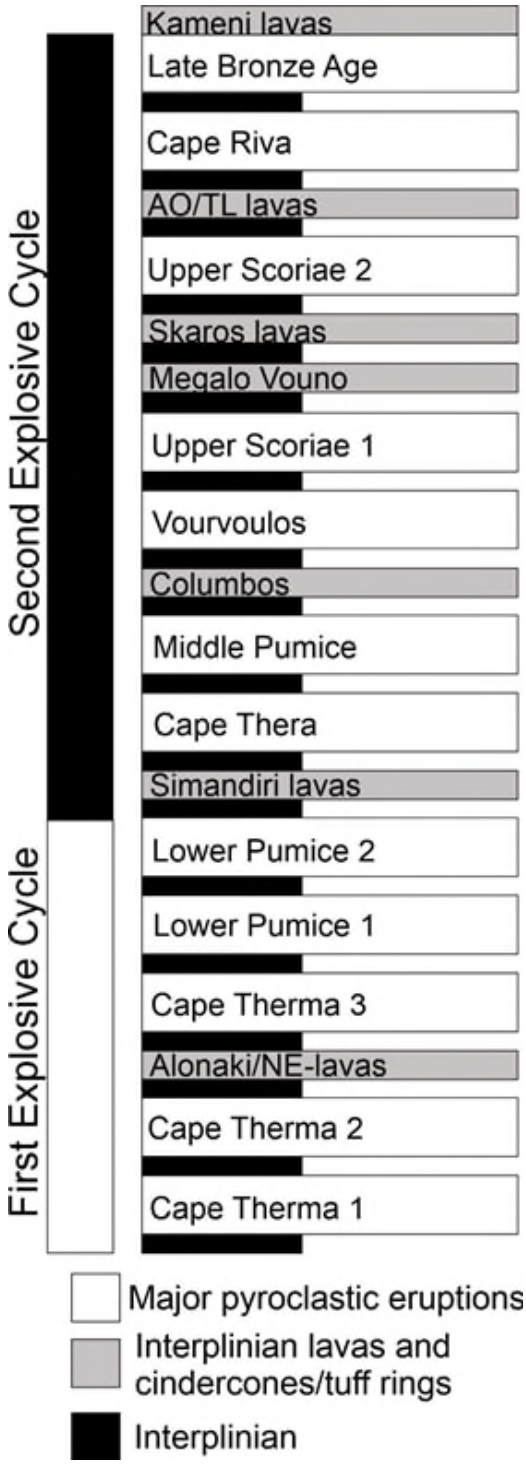

Figure 4 Schematic log of the Thera Pyroclastic Formation (TPF) of Santorini (after Druitt et al. 1999). **Table 2** describes the deposits of the 12 Plinian eruptions.

southern Thera (Druitt et al. 1999). Exposed in the cliffs of Therasia and northern Thera are the remains of four effusive centers including the Peristeria Volcano, the Simandiri shield, the Skaros shield, and the Therasia shield complex.

Between 530 and 430 ka, a stratocone complex was constructed in the northern half of the volcanic field (Druitt 2014). Major explosive activity began about 360 ka; since that time, twelve large Plinian explosive eruptions have occurred (Vespa et al. 2006; Druitt 2014) (**Figure 4**; described in **Table 2**). These eruptions are collectively referred to as the Thera Pyroclastic Formation (TPF) and are divided into two major cycles (Druitt et al. 1989, 1999). Each of the explosive cycles commenced with eruptions of mafic to intermediate magmas and terminated with a pair of major silicic Plinian eruptions and caldera collapse (Druitt et al. 1999).

Between these Plinian eruptions, smaller eruptive events produced minor ash, scoria, and pumice deposits referred to as the interplinian pyroclastic deposits (IPD) of the TPF (Vespa et al. 2006; **Figure 4**). The IPD are characterized by scoriaceous lapilli units up to several meters of thickness and several surge deposits. The prominent cones of Megalo Vouno and Kokkino Vouno belong to the IPD (Vespa et al. 2006). In general, the IPD begin with minor pumice and ash deposits followed by alternating fine and coarse ash-fall deposits (Druitt et al. 1999; Vespa et al. 2006). Interspersed between eruptions were

intervals of volcanic quiescence allowing the formation of paleosols, such as the Minoan paleosol (McCoy and Heiken 2000).

Table 2 The major explosive eruptions and their deposits (Druitt et al. 1999)

Age (ka)	Cycle	Eruption	Unit	Deposit	Average Thickness (m)
3.6	2	Minoan	D (Bo4)	Non-welded ignimbrite, lithic breccias, debris flows	40
			C (Bo3)	Massive phreatomagmatic tuff	55
			B (Bo2)	Base surges, pyroclastic flows	12
			A (Bo1)	Plinian pumice	6
21	2	Cape Riva	D	Incipiently welded ignimbrite	2
			C	Non-welded ignimbrite and lithic-lag breccia	25
			B	Incipiently to densely welded ignimbrite	12
			A	Pumice fall	4
79±8; 54±3	2	Upper Scoriae 2	D	Scoria flow with agglomerate and lithic-rich lag facies	12
			C	Scoria flow and pyroclastic surge	16
			B	Pyroclastic surge	3
			A	Pumice fall	1
	2	Upper Scoriae 1	D	Scoria flow	1
			C	Agglomerate and lithic-rich lag facies	12
			B	Scoria flow	4
			A	Scoria fall with base surge	4
	2	Vourvoulos	B	Ignimbrite and base surge	3
			A	Pumice fall	2
c. 100	2	Middle Pumice	C	Pumice fall, in part welded	1
			B	Lithic-rich and agglomerate lag facies, minor ignimbrite	60
			A	Plinian pumice, in part welded	6
	2	Cape Thera	B	Scoria flow and base surge	60
			A	Pumice fall	1
c. 180	1	Lower Pumice 2	D	Lithic-rich lag breccia	10
			C	Massive phreatomagmatic deposit	20
			B	Base surges	7
			A	Pumice fall	25
203±24	1	Lower Pumice 1	C	Non-welded ignimbrite and lithic-rich lag breccia	14
			B	Non-welded ignimbrite	14
			C	Pumice fall	5
	1	Cape Therma 3	B	Scoria flow with agglomerate and lithic-rich lag facies	20
			A	Pumice fall	1
	1	Cape Therma 2		Pumice fall	2
	1	Cape Therma 1	B	Scoria flow, incipiently welded	60
			A	Pumice fall and base surge	2

Currently, Santorini is within an interplinian effusive phase with dacitic volcanism focused on the Kameni islands. These rise 500 m above the caldera floor and represent the sub-aerial peak of a shield volcano constructed on a cone of hyaloclastites and submarine lava (Jenkins et al. 2015). The Kameni islands have been constructed by eruptions beginning in 197 BC; Palea Kameni last erupted in A.D. 726 (Jenkins et al. 2015) and the most recent eruption of Nea Kameni occurred in A.D. 1950. Nea Kameni has erupted seven times in the past 500 years, each involving extrusion of viscous lava to form domes and thick block flows accompanied by intermittent explosive explosions (Jenkins et al. 2015). Effusive volcanism is associated with seismicity, thermal springs, ground deformation, etc., and likely has been a characteristic of extrusive activity in this volcanic field since perhaps the Pliocene.

2.1.3 Pre-Late Bronze Age Eruption Topography

Numerous studies (Pichler and Friedrich 1980; Pichler and Kussmaul 1980; Heiken and McCoy 1984; Druitt and Fancaviglia 1990; Druitt 2014; Athanassas et al 2016; Druitt et al. 2019) have attempted to reconstruct the pre-LBA eruption topography – still a topic of debate. Santorini is the remnant of a clustered complex of several volcanic centers, which up to the LBA formed a large island apparently called Stronghyle, as noted by various Classical period writers (Pichler and Friedrich 1980; Pichler and Kussmaul 1980). This predecessor island was mainly built up by the products of at least ten volcanoes (Pichler and Friedrich 1980). The LBA paroxysmal eruption and consequent caldera subsidence destroyed Stronghyle island, leaving a flooded caldera with the ring-islands of Thera, Therasia, and Aspronisi as remnants. Studies of caldera formation (Druitt and Francaviglia 1992; Druitt 2014; Nomikou et al. 2016) suggest the present-day caldera is a complex structure formed by at least four collapses over 180 ky, the last of which was associated with the LBA eruption.

Early reconstructions of pre-LBA eruption Santorini conceived of a tall central volcanic cone, reaching a height of approximately 500-800 m (Bond and Sparks 1976). This was disproven by Heiken and McCoy (1984) and Druitt and Francaviglia (1990). Field data on stromatolites in Phase 3 indicates a shallow, flooded caldera, smaller than the present-day caldera, existed prior to the eruption (Eriksen et al. 1990). The northern caldera wall was formed from the products of the last major Plinian eruption, the Cape Riva eruption, about 21,800 ± 400 years ago (Druitt 1985; Fabbro et al. 2013; Karatson et al. 2018). This eruption is thought to have collapsed the pre-

existing Skaros-Therasia lava shield (Druitt and Francaviglia 1992). Evidence for this ancient caldera is:

(1) inward dips into the caldera as part of the LBA topography buried by the LBA eruption (Heiken and McCoy 1984);

(2) LBA Plinian deposits plastered in situ on the present-day caldera wall at some locations, indicating those cliffs existed prior to the LBA eruption (Druitt and Francaviglia 1992; Druitt 2014);

(3) Phase 3 deposits that contain abundant fragments of stromatolites, and travertines with gastropods and foraminifera characteristic of shallow brackish- to- saline water, consistent with the existence of a shallow, flooded caldera with poor circulation prior the LBA eruption (Eriksen et al. 1990; Anadon et al. 2013).

(4) surface exposure dating of the northern cliffs of the present-day caldera which has been dated using the ^{36}Cl exposure-dating method, indicating they existed prior to the LBA eruption (Athanassas et al. 2016).

(5) abundant fragments of a chemically distinctive black glassy andesite, interpreted as fragments of the 45-23 ka Therasia lavas (Heiken and McCoy 1984), in phase 3 tuffs believed to be pieces of an intracaldera edifice that was present inside the ancient caldera, but was destroyed during the LBA eruption. One fragment of this rock type has been dated at 20,020 ± 1000 years old, consistent with this hypothesis (Karatson et al. 2018). The estimated volume of this andesite in the tuffs is 2.5 km^3 (Karatson et al. 2018), a minimum volume for this lost shield.

Rates of current volcanic construction of the Kameni Islands (about 1 km^3 per 1,000 years), if extrapolated to a significant fraction of the period from 21,800 to 3,600 years, would suggest a central island of greater volume prior to the LBA destruction (Druitt et al. 2019).

2.2 Bronze Age Culture and Remnants - Akrotiri

2.2.1 Excavation History

Excavations at the Akrotiri archaeological site began in 1967, following a hiatus from 1939 due to WWII (Marinatos 1999) with the digging of trenches at various points along the ravine-pathway leading from the modern village of Akrotiri southwards towards the sea. Excavations continue (Doumas 2010; Paliou 2011; and others), and in 43 years have uncovered a largely intact Bronze Age seaport village that flourished for perhaps five millennia until its burial and partial destruction

by the LBA Plinian eruption. Almost intact are the remnants of a culture and its infrastructure from ~1600 BCE, a Pompeii of the Aegean (Doumas 1983b) except in this case the town is almost twice as old as the Roman town. Geological observations have accompanied archaeological work and reported in various excavation publications (Marinatos 1999; Doumas 1978, 1983a, 1983b), and in the archaeological literature (Thrope-Scholes 1978; Marthari 1990; Sotirakoupoulou 1990). Geological, geophysical, and geoarchaeological mapping within the archaeological site has been reported by Heiken and McCoy (1984, 1990); additional unpublished data by McCoy are used here as well.

2.2.2 Inhabitance Timeline from Pottery

An archaeological, relative chronology for the Aegean Bronze Age was defined by Evans (1928) based upon ceramic criteria, mainly pot shards. Resolution of time boundaries and spans using these ceramic criteria are excellent, sometimes adequate to discern chronological differences of a generation.

As the archaeological site of Akrotiri is buried and preserved beneath several meters of tephra, excavations are largely restricted to the more recent phase (Late Cycladic IA) of inhabitance, however, deep pits dug for building support pillars have given archaeologists insight of earlier inhabitance (Marinatos 1999; Doumas 1978, 1983b; Sotirakoupoulou 1990). Much of the pottery discovered here was not associated with any stratigraphic horizon (Doumas 1978; Sotirakopoulou 1990), thus, the decoration, fabric, and shape of artifacts were used to date pottery (Sotirakopoulou 1990). Some of these sporadic finds have been dated to the Neolithic, Early, and Middle Bronze Ages (Thorpes-Scholes 1978). While there are few other remains discovered with stratigraphic context, there is indirect evidence that the Cyclades, including Santorini, were in contact with the Greek mainland as early as the seventh millennium B.C. (Doumas 1983).

The earliest evidence of inhabitation at Akrotiri dates to about the third millennium B.C. or the Early Bronze Age (EBA) (Doumas 1978). A total of about 8700 pottery fragments were dated to the Early Cycladic and in some cases the Late Neolithic (Sotirakoupoulou 1990). Marinatos (1999) occasionally attributed some of the finds to the Neolithic period, but these finds were not associated with any stratigraphic horizon. During the EBA, the Therans were clearly in contact with their neighbors in southeast Aegean, specifically Crete, and other nearby islands (Thrope-Scholes 1978). Quite often, pottery discovered in the excavation pits for the roof were recognized

as belonging to the Keros-Syros and Phylakopi I cultures of the Early Cycladic period (Doumas 1978; Marinatos 1999). No stratigraphic break is evident between the Early and Middle Cycladic period. Evidence of inhabitance during the Middle Bronze Age (MBA) is also sporadic and widespread.

During the MBA and LBA transition, archaeological evidence indicates widespread destruction of Akrotiri, which is also seen at archaeological sites on Crete and elsewhere in the southern Aegean referred to as the Seismic Destruction Level (SDL: Marthari 1990; Driessen and MacDonald 1997). Most, if not all, settlements were entirely rebuilt, including Akrotiri. This seismic destruction was dated approximately 50 years before the LBA eruption (Jussert and Sintubin 2017). The Therans rebuilt Akrotiri in a more luxurious and magnificent manner after the earthquake (Doumas 1983b).

2.2.3 Maritime Trade Network

The significance and role of ancient Akrotiri in Bronze Age trade and commerce via maritime connections comes from archaeological criteria from not only Akrotiri and its adjacent Theran communities, but from excavations on surrounding islands of the Cyclades, Aegean, and eastern Mediterranean. The impact of the LBA eruption on this maritime trade was significant; the loss of Thera as a major port was huge (Driessen and MacDonald 1997). This, in conjunction with physical effects of the Plinian eruption via tsunamis, seismicity, ash plumes, pumice rafts, and other processes, was a major contribution to the demise of the cultures inhabiting Crete and the islands of the southern Aegean (Minoan, Cycladian), and the transition into the Mycenian world (Knappet et al. 2011).

From the EBA, the Cyclades, including Santorini, played the part of an intermediary between the Greek mainland, the island of Crete, and Anatolia. Being a center of sea trade, Thera quickly assumed the characteristic features of an international harbor where the Mediterranean world met, from Mycenae up to Libya (Schachermeyr 1978). Frescoes (paintings) recovered at the West House depict a flotilla (boats) and exotic animals suggesting Akrotiri and Thera had strong overseas contacts (Doumas 1983b). This abundant evidence at Akrotiri indicates it was a significant trade gateway between north Crete and the rest of the Aegean which almost certainly was disrupted by the eruption (Knappet et al. 2011).

2.2.4 Late Cycladic IA/Late Minoan IA Timeline

During the Late Bronze Age, the Theran culture was at its zenith at the time of the eruption. Santorini had become the center of a vast maritime trade network, described above, and was in close communication with Egypt, Crete, mainland Greece, and neighboring islands (Doumas 1978; Knappet et al. 2008). Currently excavated areas in Akrotiri resemble many aspects of present-day villages of Thera. The city was traversed by narrow, winding streets similar to modern villages. Streets were paved with sizeable stones (Marinatos 1999; Doumas 1978, 1983b). Beneath these paved streets, city sewers consisted of narrow stone lined ditches covered with slabs (Marinatos 1999; Doumas 1978). These sewers were connected to pits beneath the streets which received the discharge from individual buildings via clay pipes in house walls (Doumas 1978).

Excavations at the site have yet to uncover any human remains indicating a full-scale evacuation of the city, though only a fraction of the estimated total extent of the site (over 200,000 square meters) has been excavated. Archaeological evidence indicates that immediately before the final abandonment of the city, the town suffered serious damage caused by earthquakes (Doumas 1983a, 1983b). Archaeologists believe this earthquake initiated an initial evacuation of the city, after which Therans returned to clear ruins from the streets and repair buildings throughout the city (Doumas 1983a). From the archaeological evidence, Doumas (1983a, 1983b) reconstructed a sequence of events as follows:

1. Sometime before the eruption, the city suffered extensive damage, probably due to earthquakes, with evacuation of the town.
2. Systematic works were undertaken by returning residents to clear streets of rubble, repair dangerous walls, and repair buildings.
3. During restoration, the volcano started to erupt with a minor ashfall, and people left the island, possibly warned by noxious fumes and gases (pulses 1 and 2 of precursor). Prior to evacuating the city, the Therans took measures to secure food left behind in large pithoi (jars) which they secured under doors and stairs. As there is an absence of bodies as well as a lack of objects made of precious metals recovered during excavations, it is suggested the inhabitance took valuables with them as they evacuated the island.
4. A minor eruption produced fine pumice which covered the city, but not the entire island with a mantle about three centimeters thick (pulse 3 of precursor).

5. Oxidation in this layer of pumice suggests a considerable time period elapsed during which there was no further volcanic activity.
6. After this hiatus followed the main eruption, described in detail below.

2.3 Late Bronze Age Eruption

2.3.1 Eruption Sequence

The LBA eruption occurred in four major phases, with a minor precursor fifth phase (**Figure 5**). The four major stratigraphic units were designated by Reck (1936) as Bo_1, Bo_2, Bo_3, and Bo_4 ("Bo" = "bimstein oberer" or upper pumice), and later by Druitt et al. (1989) as Minoan A, B, C, and D. A fifth, thin basal unit was designated as Bo_0 by Heiken and McCoy (1990). Each of the four major phases are briefly described below, with inferences on eruptive behavior and vent placement suggested by tephra characteristics and bed forms.

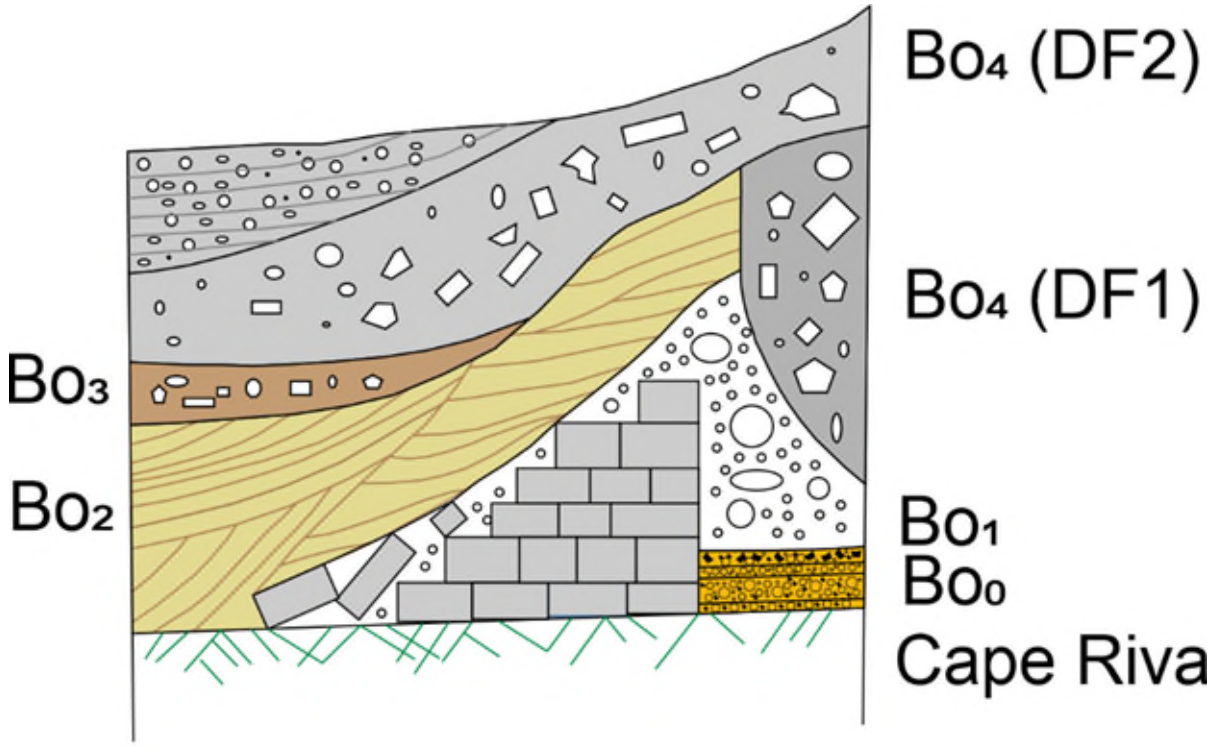

Figure 5 Stratigraphic column of full eruption sequence. The precursory (Bo_0) and first phase (Bo_1) pumice preserved buildings before phase 2 (Bo_2) destroyed exposed portions of buildings. Phase 3 (Bo_3) and (Bo_4) the eroded previously deposited layers, destroying buildings even further via debris flows (DF1, DF2) that eroded into previously deposited volcaniclastic layers.

First Major Eruption Phase (Bo_1/Minoan A): Plinian pumice fall. The first major phase generated a sustained plume at an estimated height of 36±5 km (Johnston et al. 2014). The pumice and ash deposit has a maximum thickness of 7 m south of Fira and thins rapidly to the north, south,

and west (Friedrich 2009; McCoy and Heiken 2000). Isopachs define a southeasterly dispersal axis indicative of a subaerial vent between present-day Nea Kameni and Fira (Bond and Sparks

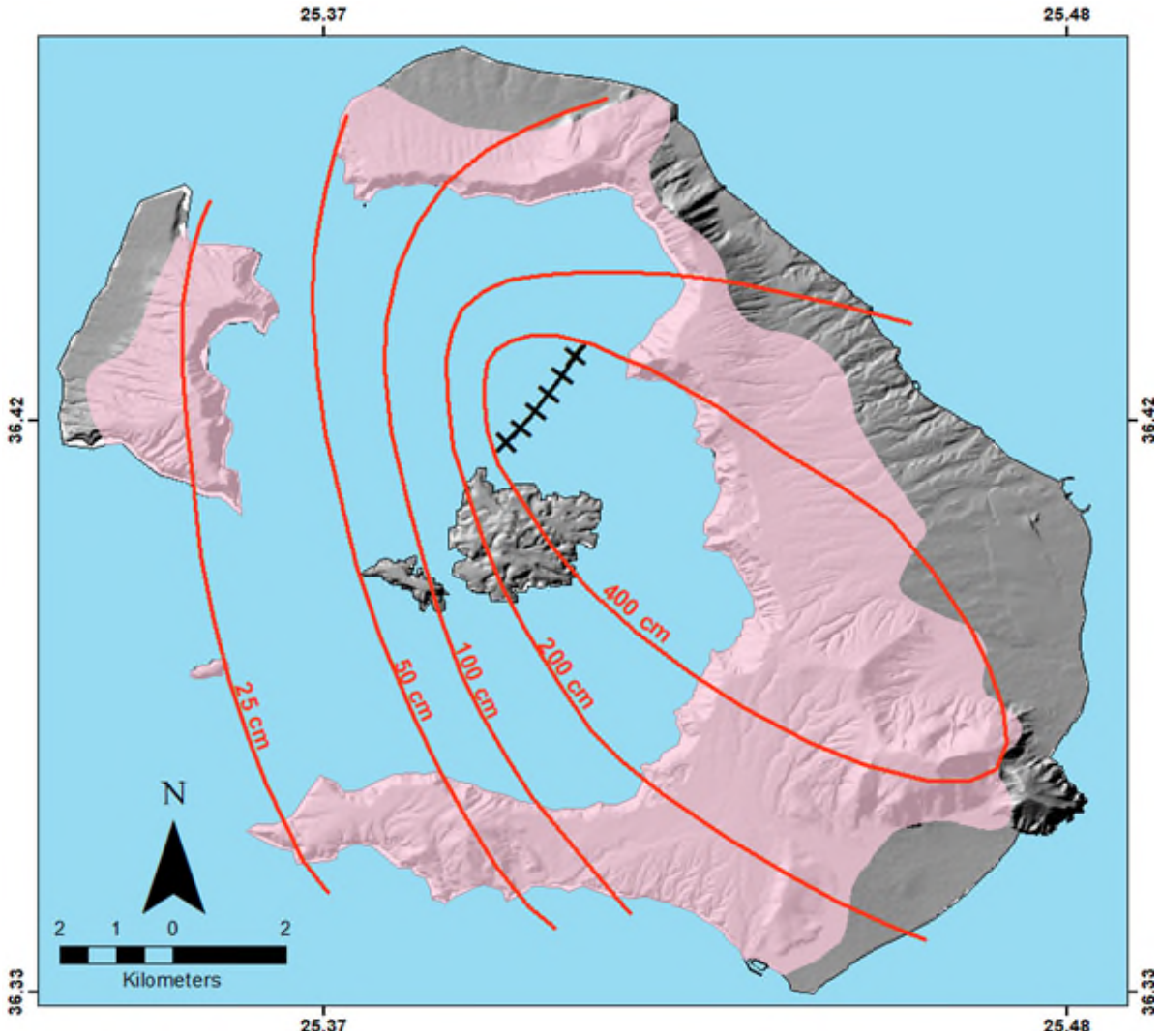

Figure 6 Plinian Phase 1. Suture line indicates the approximate vent location based on isopach lines (red contour lines); the Phase 1 deposit is depicted in the light pink overlying a hill-shade of Santorini (Bond and Sparks 1976; McCoy and Heiken 2000a, 2000b). Basemap DEM from Paraskevas et al. (2019).

1976; McCoy and Heiken 2000; Druitt 2014) (**Figure 6**). Sparks and Wilson (1990) estimated an accumulation rate of 3 cm/min and a duration of 1-8 hour(s).

Phase 1 consisted of a violent continuous discharge of gas and magma. Exsolution of dissolved gas propelled magma upwards, tearing it apart, discharging a turbulent mixture of gas, pumice, and ash into the stratosphere.

On land, the deposit is composed of white to pale-pink, angular pumice clasts (Bond and Sparks 1976) (0.5-20 cm) with less than 10% ash and lithic fragments in an open-framework structure (McCoy and Heiken 2000). From the base upward, the deposit has a reversely graded, crudely bedded unit overlain by a coarser, non-bedded unit that is normally graded in its upper part and contains up to a few percent of andesitic scoria (Druitt 2014). The content of wall rock, lithic clasts increases towards the top of the deposit to form a lithic enriched zone making up between 5 and 40% of the total thickness (Bond and Sparks 1976). The increasing content of lithic fragments up-section, together with the coarsening of the pumice, suggests an intensification of the eruption and increased depositional rates of tephra during this first phase of activity (Bond and Sparks 1976). Lithic fragments include a highly ferruginous sandstone, altered tuffs, and some hypabyssal rocks (Bond and Sparks 1976).

Pumice deposited on the sea around Thera, likely formed enormous rafts of floating pumice, which drifted on surface currents throughout the Aegean and eastern Mediterranean. The uppermost stratigraphic interval in the Bo_1 sequence is an alternating sequence of up to three pyroclastic flow layers and two interbedded pumice falls (McCoy and Heiken 2000). McCoy and Heiken (2000) argue this represents a major change in eruption style due to vent extension allowing seawater access to the vent.

Second Major Eruption Phase (Bo_2/Minoan B): Pyroclastic flows and surges. The deposits of the second phase indicated a change in eruption character and vent placement (Bond and Sparks 1976; Heiken and McCoy 1984). Pyroclastic surge deposits with planar and cross-stratification indicate phreatomagmatic activity and suggesting unlimited access by water into the vent (McCoy and Heiken 2000). These deposits vary in thickness up to 12 m (Pfeiffer 2001). Isopachs of the second-phase deposit show thicker accumulations on southern Thera than on Therasia and northern Thera (2-4 m) (McCoy and Heiken 2000). The pattern of thickness variations and pyroclastic flow and surge emplacement directions implies a vent located south of the first phase vent in the water-filled embayment prominent in the LBA pre-eruption landscape (Bond and Sparks 1976; Heiken and McCoy 1984) (**Figure 7**). Sparks and Wilson (1990) calculated a duration of perhaps 1 hour for the second-phase activity with accumulation rates on the order of 3cm/min. Temperatures of emplacement were ~100-300°C (Downey and Tarling 1984; McClelland and Thomas 1990;

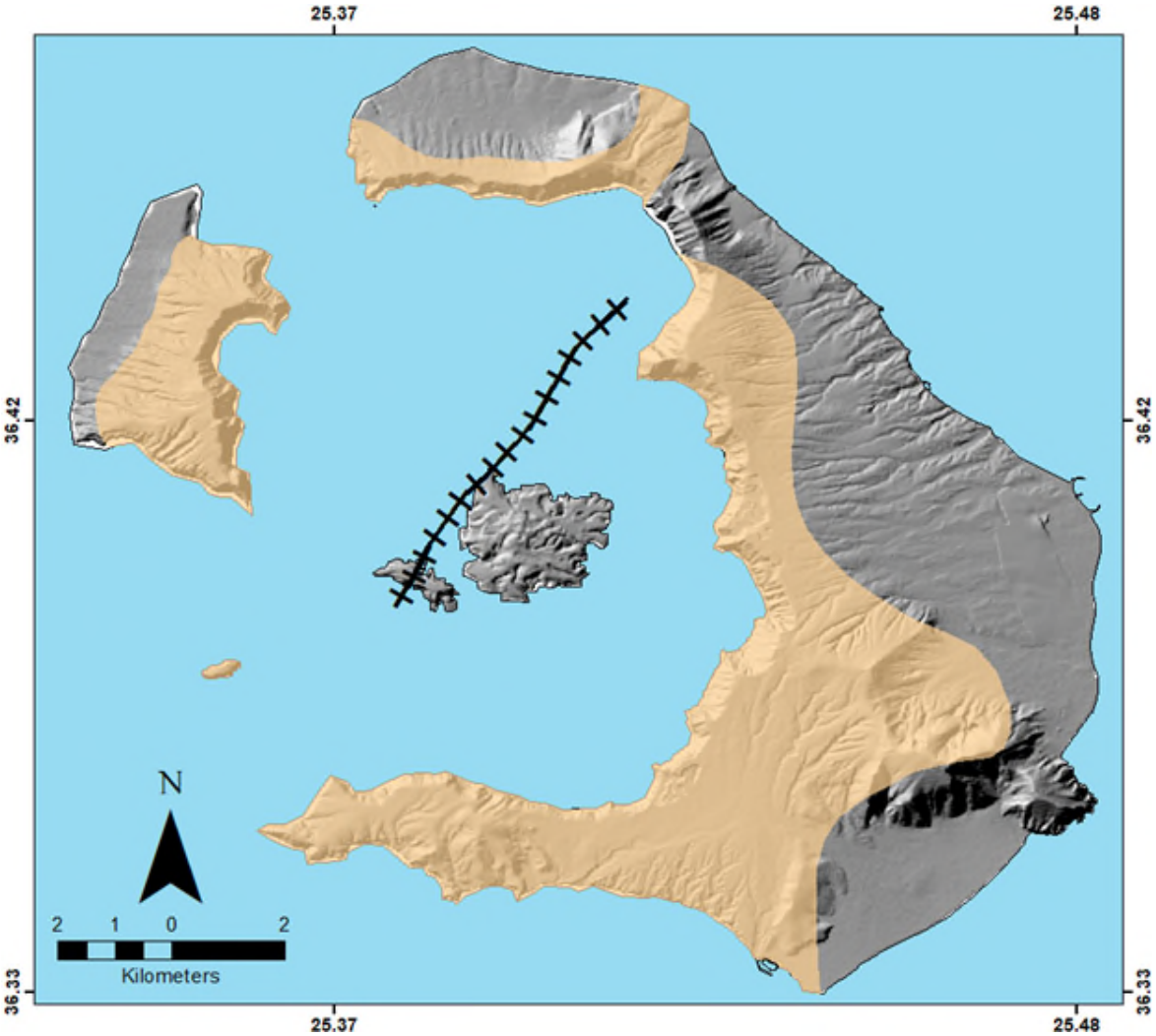

Figure 7 Phreatomagmatic Phase 2. Suture line indicates the approximate vent location; the Phase 2 deposit is depicted in the light orange overlying a hill-shade of Santorini (Bond and Sparks 1976; McCoy and Heiken 2000a, 2000b). Basemap DEM from Paraskevas et al. (2019).

Johnston et al. 2014). This phase also likely represented initial caldera collapse (Heiken and McCoy 1984).

Three units are distinctive within the second phase deposit: (1) a thicker lower unit ranging from 10-590 cm thick; (2) a thin middle unit of white ash, 1-18 cm thick; and (3) a thicker upper unit with a thickness of 16-600 cm (McCoy and Heiken 2000). The lower unit is a series of planar bed and low-angle, small amplitude (up to 0.5 m) cross beds of centimetric thickness composed of well to poorly sorted, rounded pumice lapilli, ash, and rare, small (<10 cm) lithic fragments (McCoy and Heiken 2000). The middle unit contains white ash and accretionary lapilli in sharp contact with the underlying and overlying units (McCoy and Heiken 2000). In some areas, a weak structure consists of a lower unit of accretionary lapilli mixed with small gray lithic fragments in

an open-framework texture, overlain by homogenous ash (McCoy and Heiken 2000). The upper unit is distinguished by large-scale megaripples, with amplitudes up to 2 m, and planar beds (McCoy and Heiken 2000). Individual layers consist of a poorly sorted mixture of ash, lapilli, and block-sized, subangular to rounded pumice, with an increasing lithic content up-section (McCoy and Heiken 2000).

Third Major Eruption Phase (Bo$_3$/Minoan C): Phreatomagmatic activity. The third phase was the most enigmatic and also voluminous phase of the eruption. Phreatomagmatic activity continued with this phase producing pyroclastic flows (Heiken and McCoy 1984; Sparks and Wilson 1990), and pumiceous mud flows with the final caldera collapse (Bond and Sparks 1976).

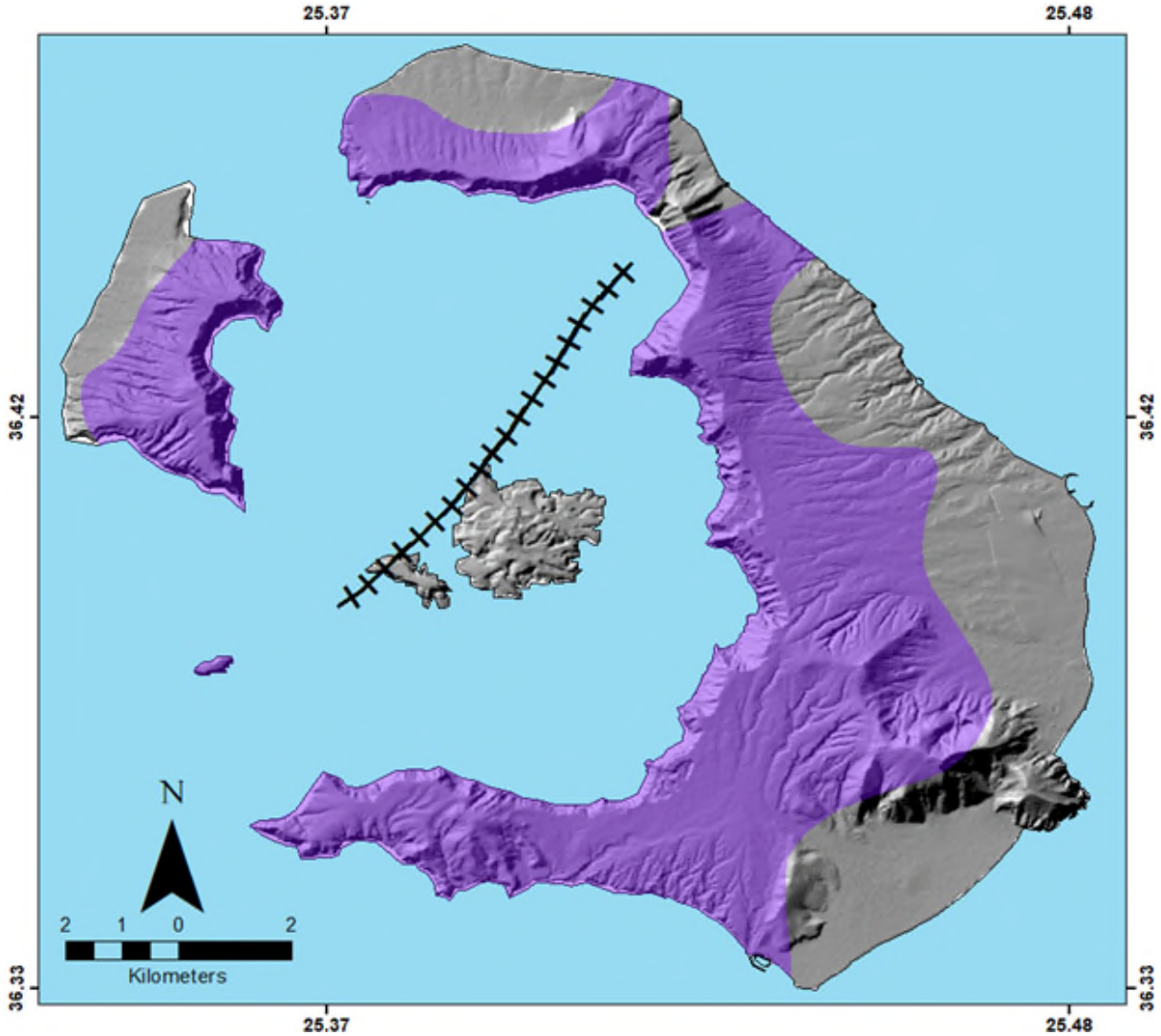

Figure 8 Phase 3. Suture line indicates the approximate vent location; the Phase 3 deposit is depicted in the purple overlying a hill-shade of Santorini (Bond and Sparks 1976; McCoy and Heiken 2000a, 2000b). Basemap DEM from Paraskevas et al. (2019).

Water-magma explosions produced dense clouds of ash that appear to have spread radially from the base of the eruption column (Sparks 1979). The third phase deposits attain their greatest thickness (up to 55 m) in topographic depressions and contain pumice up to 30 cm and lithic blocks range from 10 to +200 cm (Bond and Sparks 1976). Temperatures during emplacement were cold, for some lithic clasts, up to perhaps 400°C (Downey and Tarling 1984; McLelland and Thomas 1990).

Lithic clasts are predominantly black, glassy, porphyritic dacites and red hyaloclastites (McCoy and Heiken 2000). The absence of structures surrounding some lithic clasts, such as impact pits, suggests emplacement as suspension in a density current (McCoy and Heiken 2000). Elsewhere,

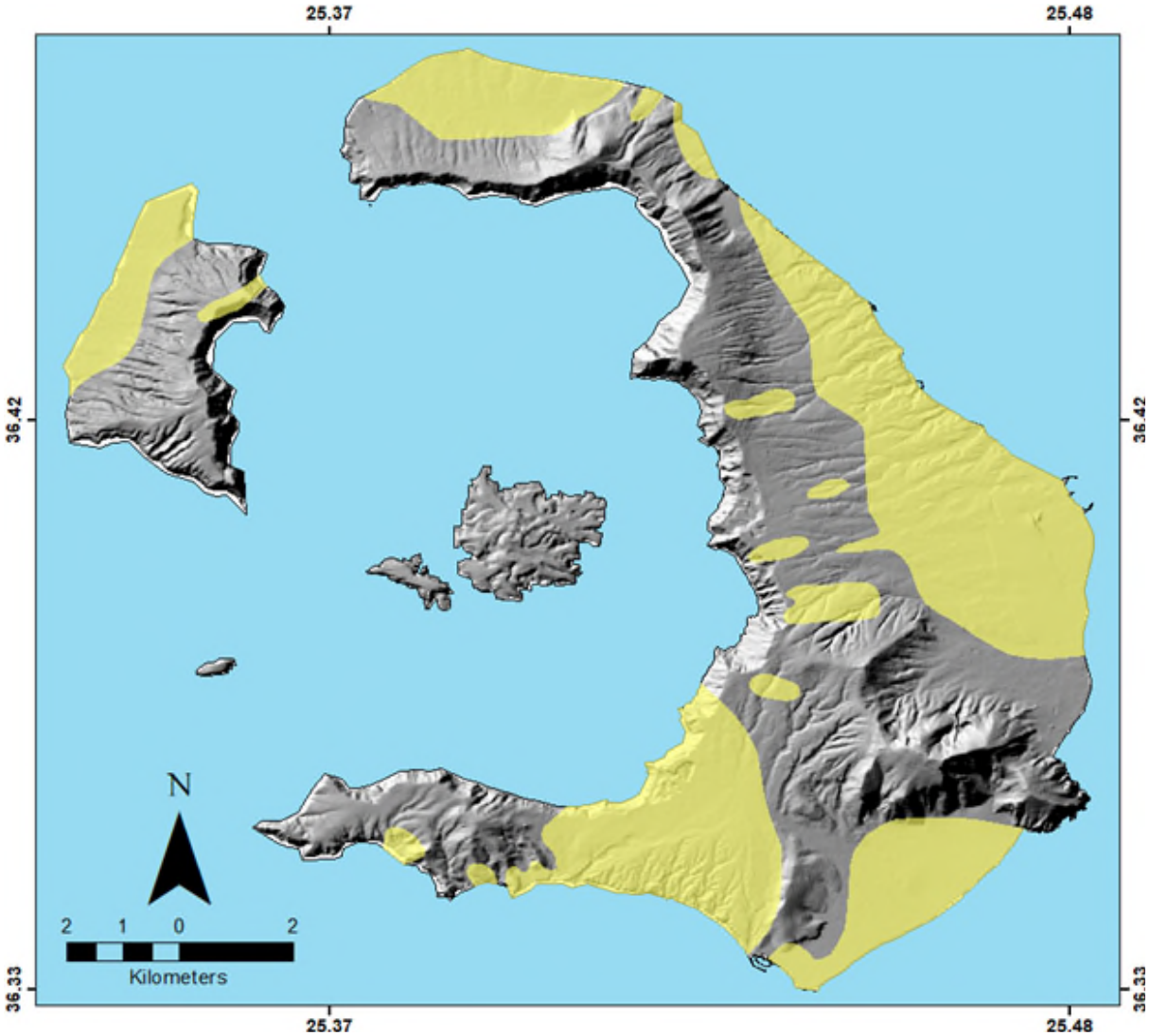

Figure 9 Phase 4 deposits are depicted in yellow overlying a hill-shade of Santorini (Bond and Sparks 1976; McCoy and Heiken 2000a, 2000b). Basemap DEM from Paraskevas et al. (2019).

bomb sags and impact pits provide evidence of ballistic emplacement and identify vent location during the third phase activity. These features, in combination with isopachs of the third phase, indicate a vent position proximal to the second phase vent, but with some extension to the northeast (McCoy and Heiken 2000; Pfeiffer 2001) (**Figure 8**).

Fourth Major Eruption Phase (Bo$_4$/Minoan D): Ignimbrites, lithic-rich base surges, lahars, and debris flows. The fourth phase was a consequence of the continued collapse of the caldera (Sparks 1979). As the eruption column lost kinetic energy, the mixture of gas, heated air, and rock fragments became less dense than the surrounding air and collapsed onto the volcano's flanks. This final phase was marked by variable phreatomagmatic activity resulting in interbedded ignimbrites, lithic-rich base surge deposits, lithic-rich and ash-rich lahars, and debris flows, with some co-ignimbrite ash fall deposits (Bond and Sparks 1976).

Along the caldera rim, the fourth phase deposits are thin, 0.7-2 m, but they form thick fan-shaped coastal plains up to 40 m thick (Pfeiffer 2001; **Figure 9**). These imply pyroclastic flow directions that were strongly influenced by topographic depressions along the caldera (McCoy and Heiken 2000). These deposits are massive, light-tan lapilli and pumice-bearing ash (Heiken and McCoy 1984). Bedding is poorly developed and visible by concentrations of small lithic fragments (Heiken and McCoy 1984). This faint layering appears due to subtle grading of lithic fragments within the individual flow deposits (Heiken and McCoy 1984). Interbedded with pyroclastic flows are tuffaceous epiclastic sediments, graded pumice layers, wedge-shaped concentrations of rounded, cobble- and boulder-size lithic fragments (Heiken and McCoy 1984), and clastic redeposited layers consequent of tsunami inundation (McCoy and Heiken 2000).

2.3.2 Explosivity and Magnitude

Previous calculations estimated the volume of tephra erupted was 36 km^3 (Pyle 1990). The volume of material involved in the collapse of the northern portion of the island to form the LBA caldera was 18-39 km^3 (Heiken and McCoy 1984). New estimates of the eruption volume, using new data from offshore geophysical surveys and prior estimates of tephra fall deposits, is 60 km^3 dense rock equivalent (DRE) (Johnston et al. 2014). Following Newhall and Self (1982) and Pyle (2000), the volcanic explosivity index (VEI) and magnitude of the LBA eruption was 6 and 6.5, respectively, although this estimate does not include material within the caldera (Johnston et al. 2014).

Johnston et al. (2014) considered, for example, the phase 3 deposits as cold pyroclastic flows and mud flows with relatively low mobility; this would have prevented them from surmounting the steep (34-60°) pre-existing 200-300 m high caldera walls. Accordingly, Johnston et al. (2014) proposed that during Phases 2 and 3, the explosive activity gradually filled the pre-existing caldera depression. While some mobile Phase 2 surges were able to surmount the caldera walls to form deposits on the caldera rim and beyond, it was only until the entire caldera was filled with the Phase 2 and 3 deposits that the low-temperature pyroclastic flows of Phase 3 were able to flow down the flanks to produce outflow sheets (Johnston et al. 2014). Thus, considering the infilling during Phases 2 and 3, the new calculated eruption volume might be between 117-129 km^3 or 78-86 km^3 DRE (Johnston et al. 2014). This new criteria raised the VEI and magnitude of the eruption to 7 and 7.3, respectively (Johnston et al. 2014).

The eruption lasted anywhere from six hours to four days (Pyle 1990; Sparks and Wilson 1990; Wilson 1990), erupting at an intensity of 1.4-4.2 x 10^8 kg/sec with an estimated accumulation rate on the order of 3 cm/min (Sparks and Wilson 1990).

2.3.3 Date of the Eruption

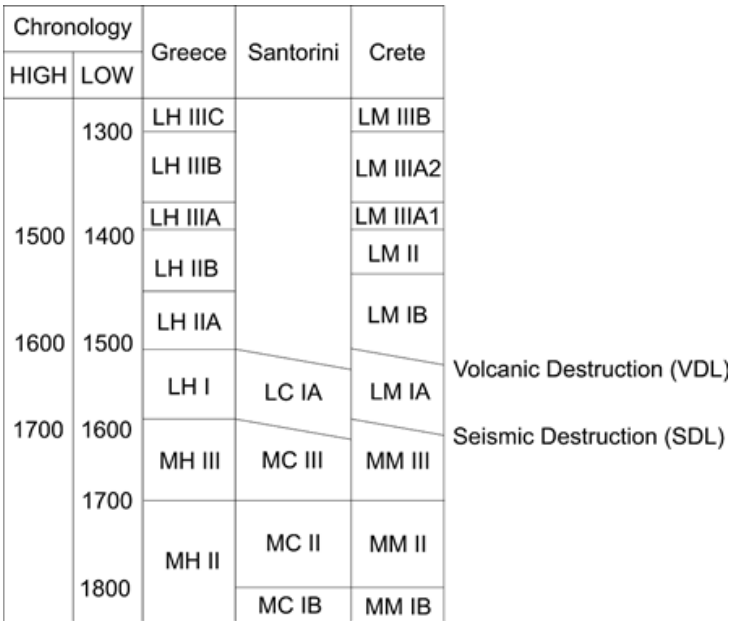

Figure 10 Simplified chronological overview (from Klontza-Jaklova 2016 and Marthari 1990).

The LBA eruption provides a geological marker that, if precisely dated, could synchronize Bronze Age histories of the Aegean, Eygpt, and the Near East and anchor a wide range of contemporary environmental data. However, dating has proved problematic because of observed discrepancies between timelines derived from archaeological evidence and those based on radiocarbon dating (Ramsey et al. 2004; Weiner 2012). Relative carbon-14, archaeological, typological and stratigraphical criteria and chronology dated the LBA eruption 1450 BCE. In the

stratigraphy of Cretan settlements, the eruption defines the transition for LMIA and LMIB (**Figure 10**; Marthari 1990; Driessen and McDonald 1997; Klontza-Jaklova 2016). This date was accepted until numerous absolute dating methods, including radiocarbon (Hammer et al. 1987; Friedrich et al. 2006; and others), dendrochronology (Kuniholm 1990; Baillie 1990; and others); ice core dating (Hammer et al. 1987); and other methods (Downey and Tarling 1984; Schoch 1995; and others) were used to date the eruption. The first calibrated radiocarbon dates suggested a date earlier than 1530 BC, while dendrochronology and ice core dating shifted the eruption closer to the mid-17th century B.C. (Klontza-Jaklova 2016). Since the mid-1980s, a date for the Minoan eruption of Santorini is 100 to 150 years higher than previously argued was suggested by radiocarbon dating and climatic events recorded in ice cores and tree rings from North America, Europe, and the eastern Mediterranean, placing the eruption at the end of the Late Minoan (LM) IA period in the second half of the seventeenth century BCE (Bentacourt 1987; Manning 1988, 1990, 1999, 2007, 2009; Friedrich et al. 1990, 2006, 2009; Friedrich and Heinemeier 2009; and others).

The most reliable radiocarbon dating results are obtained if short-lived materials (e.g. short-lived shrubs and crops harvested shortly before the eruption) directly connected with the destruction level are dated (Hammer et al. 1987). Radiocarbon dates on short-lived organic material from Akrotiri have been of limited precision. A living olive tree branch found in a Bo_1 layer was partly preserved as it was buried in tephra. Radiocarbon dates from divided sections of four consecutive groups of rings (72 rings identified) determined a calibrated age of 1621-1605 B.C. (1σ, 68% confidence) or 1627-1600 B.C. (2σ, 95% confidence) for the outermost ring (Friedrich et al. 2006). The tree-ring sequence of this olive branch has been the subject of extensive dispute (Warren 2006, 2009; Wiener 2009). Olive trees have indistinct growth boundaries that may represent multiple growth phases in a single year or may miss periods of growth (Cherubini et al. 2013). As these discussions focused on the oscillating nature of the radiocarbon calibration curve over the relevant period, which makes it impossible to distinguish on radiocarbon grounds alone between an event around 1610 BCE and one around 1525 BCE (Cherubini et al. 2014).

Other calibrated radiocarbon dates for the eruption cluster into two groups, 1500-1550 B.C. and 1615-1645 B.C. (McCoy and Heiken 2000). The younger chronology is supported by the correlation to the Egyptian archaeological and cultural chronology. The older chronology is supported by dendrochronologic criteria and radiocarbon dates in Anatolia, Ireland, and

southwestern United States (Kuniholm et al. 1996; LaMarche and Hirschboeck 1984); a pronounced acid-layer in two ice cores from the Greenland ice cap (described below) (Hammer et al. 1987); and by climatic perturbations recorded in Chinese cultural records (Pang et al. 1989). Höflmayer (2012) argues three possible scenarios to explain the difference between 14C data and archaeological synchronizations: (1) either the archaeological synchronization between the Aegean and Egypt was flawed, so that raising of the Aegean chronology would be possible without changing dates for the Egyptian New Kingdom or questioning the ^{14}C data; (2) the historically derived dates for the beginning of the New Kingdom were too low and could be raised by extending reigns of certain kings, in order to keep the ^{14}C data and the long-held Aegean-Egyptian archaeological synchronization; or (3) for some (unknown) reason ^{14}C dating offers erroneous results for the Aegean early LBA and should be dismissed as evidence for the absolute chronology.

Tree-ring records constructed from ancient wooden timbers can provide calendar-dated frameworks to underpin archaeological and paleoenvironmental chronologies beyond the reach of written evidence (Pearson et al. 2020). Pearson et al. (2018) measured ^{14}C in single tree rings of known age from high-altitude bristlecone pine from the White Mountains of California and low-altitude oak from County Kildare, Ireland. These measurements were compared with the IntCal13 raw data and IntCal13 curve (Pearson et al. 2018). While the annual data points fell within the 2σ range of the raw data underlying IntCal13, there was a clear and sustained offset in the annual measurements between 1660 and 1540 BCE when compared to IntCal13 (Pearson et al. 2018). This observed offset is of a comparable size to have resulted from regional differences in 14C uptake (Ramsey et al. 2010). Pearson et al. (2018) argues where small changes in the curve like transition periods around ^{14}C plateaus can have a large effect on calibrated ages. Radiocarbon results indicate that the LBA eruption occurred during a plateau in ^{14}C production, making current radiocarbon ranges less precise and limiting the potential of radiocarbon dating to provide an exact date for the event (Pearson et al. 2018).

Dendrochronology provides an accurate absolute date, but only if the circumstances are optimal. One obvious difficulty is the geographical limitation of the method, but it should be able to trace radical global changes across regional systems (LaMarche and Hierschboeck 1984). It is assumed explosive volcanic eruptions, like the LBA eruption, influence climate over a large region or globally, thus inducing global change in tree growth. This causes growth stresses which can be

seen in the tree ring patterns of long-lived species (Klontza-Jaklova 2016). Studies of 4000-year-old sequoias looked for growth anomalies around 1500 B.C., but the first anomalies occurred at around 1627 B.C. (Kuniholm 1990). Baillie (1990) identified a similar anomaly, in the interval of 1644 ± 20 BC, when studying Irish oaks. This anomaly was associated with the result of a powerful volcanic event (Baillie 1990).

Thermoluminescence, also referred to archaeomagnetic dating, is based on the fact that fired materials are capable of retaining a magnetic remanence so the direction and intensity of the geomagnetic field can be determined for the time that the materials were cooling (Downey and Tarling 1984). The fired objects can be dated by comparing their properties with the past record of the geomagnetic field if patterns of directional and intensity changes are known (Downey and Tarling 1984). Potsherds from Akrotiri were dated using this method to obtain an age of 3600 ± 200 years, which agrees with radiocarbon dates (Friedrich 2009).

Eruptions of large magnitude (VEI 6 or higher) are expected to show up in acidity records in the Greenland ice cores (Hammer et al. 1987). The Dye 3 deep ice core presents a complete record of annual snow layers which have been dated stratigraphically by means of seasonal variations within each annual layer (Hammer et al. 1987). Three different, seasonally varying parameters (isotopic composition, dust content, and acidity) were used in order to obtain the most accurate dating possible (Hammer et al. 1987). Climate perturbations and acid rain are presumed the result of sulfur aerosols injected into the stratosphere by the LBA eruption (McCoy and Heiken 2000). Three acidity peaks were identified, two of which were dominated by nitric acid and third being dominated by sulphric acid (Hammer et al. 1987). The sulphuric acid peak, presumed to be of volcanic origin, was dated to 1644 B.C., with an estimated standard deviation of ± 7 years and an estimated error limit of ± 20 years (Hammer et al. 1987).

3.0 Methodology

3.1 Field Methods

Field observations and measurements of the deposit of the precursory eruptions were collected at 16 outcrops, where this layer was found in exposures that were safely accessible. Additional data was taken from field notes from prior mapping by McCoy (1996-2012) and Heiken and McCoy (1990). The latter was especially significant for exposures now gone due to erosion and construction activities. Outcrops are increasingly limited due to extensive construction and over-tourism on the island. Field measurements included total tephra thickness and the thickness of

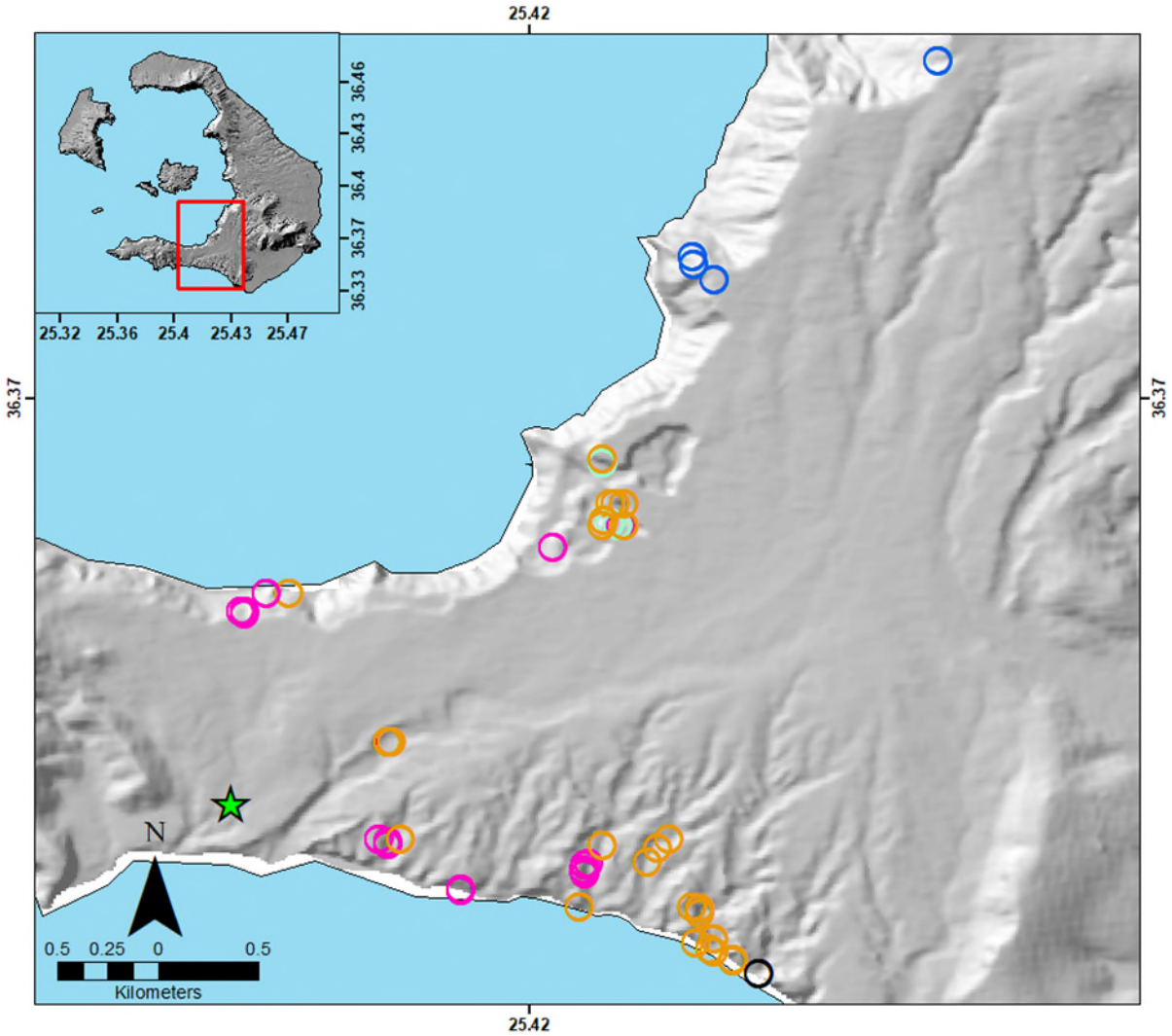

Figure 11 Exposures where the precursory deposit was observed. Pink circles indicate all four pulses were observed; orange circles indicate pulses 2 through 4 were observed; blue circles indicate pulse 3 was observed; light green circles indicate pulses 3 and 4 were observed; and black circles indicate only pulse 2 was observed. Green star indicates the location of the Akrotiri Archaeological Site. Basemap DEM from Paraskevas et al. (2019).

each internal layer. Field observations included the type of stratigraphic contact between each layer and at the boundaries of the deposit, appearance of fossils and molds/casts, and anthropogenic features (e.g. buildings, agricultural walls, pot sherds, etc.). Pulses were recognized by changing tephra componentry, qualitative grain size changes, or color in stratigraphy.

During the 2018 field season, thirty-two (32) samples were collected in situ from twenty (20) outcrops. During the 2019 field season, an additional forty-two (42) samples were collected from 16 outcrops. Samples were collected carefully from the four sub-units. Where exposures were several meters in length, three to four field measurements and samples were collected for analysis. Previously sampled 2018 exposures were resampled in 2019 (**Figure 11**) to check and validate the field and laboratory methodology. All samples were returned to the University of Hawaii for processing.

Isopach maps of each precursory subunit were hand-drawn. The most distal isopach for each map was 0 cm though there is a margin of uncertainty as the distal extent of the 0 cm isopach line could not be constrained in the field. Proximal field observations also could not be observed in the field, thus the location of the vent for each pulse is inferred based on the location of present-day Nea Kameni and Palea Kameni and the Kameni tectonic lineament. Isopach maps were further processed with ArcGIS in order to calculate isopach areas. Empirical integration of deposit thinning trends was constrained to compute tephra fall volumes using the Exponential Thinning (Pyle 1989, 1995), Power Law (Bonadonna and Houghton 2005), and Weibell method (Bonadonna and Costa 2012).

The use of various combinations of exponential segments is sensitive to the number and choice of segments. Pyle (1989) argues that thickness versus (isopach area)$^{1/2}$ plots are curved, which implies an exponential thinning law. In order to characterize the exponential decay of thickness and grainsize data for most tephra fall deposits, two quantitative parameters, thickness half distance and maximum clast size half distance, were proposed by Pyle (1989). Plotting the logarithm of thickness versus (isopach area)$^{1/2}$ allows extrapolation of deposit thickness and volume into the distal field and the elimination of complexities and uncertainties caused by distortion of isopach contours due to wind and secondary thickening processes (Pyle 1989):

$$T_{exp} = T_0 e^{-kA^{1/2}}, \quad (1)$$

where, T_{exp} corresponds to thickness calculated using an exponential approximation, A to isopach area, and T_0 and k are free parameters. T_0 represents the thickness at source, i.e., where $A=A^{1/2}=0$, and k is the slope of logarithm of thickness versus (isopach area)$^{1/2}$ plots.

The power-law method applied by Bonadonna and Houghton (2005) projects a power-law fit on semi-log plots of thickness versus (isopach area)1/2:

$$T_{power} = T_{PL}\sqrt{A}^{(-m)}, \tag{2}$$

where T_{PL} is a constant and m is the power-law coefficient. In contrast to the exponential relationship, the power-law method better reproduces the natural thinning of many tephra units, but volume calculations are strongly sensitive to the choice of the proximal and distal limits of the integration. Accordingly, when poorly constrained in these regions, the power-law method has high levels of uncertainty for volume calculations of tephra deposits (Klawonn et al. 2014). Therefore, extrapolation is generally required since the power-law fit provides neither a proximal maximum for T_{power} nor a distal limit at which T_{power} becomes zero.

The Weibull method, first proposed by Bonadonna and Costa (2012), depends on three free parameters n, Θ, and λ; n being a dimensionless shape parameter, Θ representing a thickness scale (typically expressed in centimeters) and λ being the characteristic decay length scale of deposit thinning (typically expressed in kilometers):

$$T_W = \theta\left(\frac{A^{\frac{1}{2}}}{\lambda}\right)^{n-2} e^{-\left(\frac{A^{\frac{1}{2}}}{\lambda}\right)^n} \tag{3}$$

Integration of various empirical thickness relationships over area gives volume estimates. The volume for each exponential segment defined by Eq. 1 is given by:

$$V_{exp} = \int_{A_1}^{A_2} T_{exp}\,dA = 2T_0k^{-2}\left[e^{-kA^{\frac{1}{2}}}\left(-kA^{\frac{1}{2}} - 1\right)\right]_{A_1}^{A_2} \tag{4}$$

which simplifies to $V_{exp}=2T_0k^{-2}$ when integrating from area A_1=0 to infinity (A_2=∞).

Volume for the power-law function (Eq. 2) is given by:

$$V_{power} = \int_{A_1}^{A_2} p_1(A^{1/2})^{-p_2}\,dA = 2p_1(2-p_2)^{-1}\left[A^{\frac{p_2+2}{2}}\right]_{A_1}^{A_2} \tag{5}$$

Since V_{power} yields infinity for both A1→0 and A2→∞, integration limits need to be defined to arrive at volume estimates. Bonadonna and Houghton (2005) suggested defining an integration limit for A1 as the area at which the near-vent interpolation of the power-law function reaches the thickness that is associated with the maximum thickness T0 derived with the exponential function (see Eq. 1). For the distal integration limit, A2, a limit for each pulse was defined based on the 0 isopach line which was hand-drawn based on whether precursory layers were observed between the paleosol or Cape Riva and Phase 1 of the LBA eruption.

Finally, the volume using the Weibull relationship of Eq. 3 is defined by:

$$V_w = \int_{A_1}^{A_2} T_w dA = 2\theta\lambda^2 n^{-1}[-e^{-(A^{1/2}\lambda^{-1})^n}]_{A_1}^{A_2} \quad (6)$$

which simplifies to $V_w = 2\Theta\lambda^2 n^{-2}$ for area $A_1 = 0$ and area $A_2 = \infty$.

3.2 Laboratory Methods

3.2.1 Grain Size

Size analyses were conducted for the four pulses of the precursory eruption using sieves at one phi (ϕ) intervals where $\phi = -\text{Log}_2 d$, where d is the particle diameter in mm ("b" axis of a presumed "best-fit" ellipsoid-sphere to the particle). Sieving was performed for all samples in the range -5.0 to 3.0 ϕ. Because the samples are mostly pumice, liable to be damaged by mechanical sieving, sieving was done gently by hand for 1 to 2 minutes to minimize mechanical abrasion.

Tephra fall deposit grain size was characterized using the parameters of Folk and Ward (1957), which were calculated with the Gradistat package (Blott and Pye 2001). The parameters used to describe a grain size distribution fall into four principal groups: (a) the average grain size (equation 4), and (b) the spread (sorting) of the sizes around the average (equation 5).

$$M_Z = \frac{\phi_{16}+\phi_{50}+\phi_{84}}{3} \quad (4)$$

$$\sigma_\phi = \frac{\phi_{84}-\phi_{16}}{4} + \frac{\phi_{95}-\phi_5}{6.6} \quad (5)$$

3.2.2 Tephra Componentry, Morphology, and Ratios

Analysis of componentry, morphology, and particle composition ratios were undertaken on all collected samples. Three main components as clasts within the precursory deposit were distinguished: lithics, pumice, and crystals in each sieve size. Dominant grain morphology was

noted for the grain population component. Lithic, glass, and pumice counts were determined only for clasts larger than 0.5 mm. It was determined the lithic to pumice ratio would be skewed at clasts finer than 0.5 mm. Clast counts of each sieve size were summed to obtain a percentage of each category in a sample. Lithics, pumice, and crystals were counted due to the large density difference between the pumice and lithic fragments and would be heavily skewed towards lithic fragments if done by weight.

4.0 Results

4.1 Field Mapping and Observations (tephra distribution, stratigraphy, preservation, stratigraphic contacts)

The precursory deposit is composed of four thin (1-5 cm) but distinct tephra fall layers (**Figure 12**). The classification of the four layers is based on (a) componentry; (b) tephra color; and (c) qualitative grain size changes (**Table 3**; and following sections). Each layer is in sharp stratigraphic contact with the underlying and overlying layers as is the boundary to the underlying

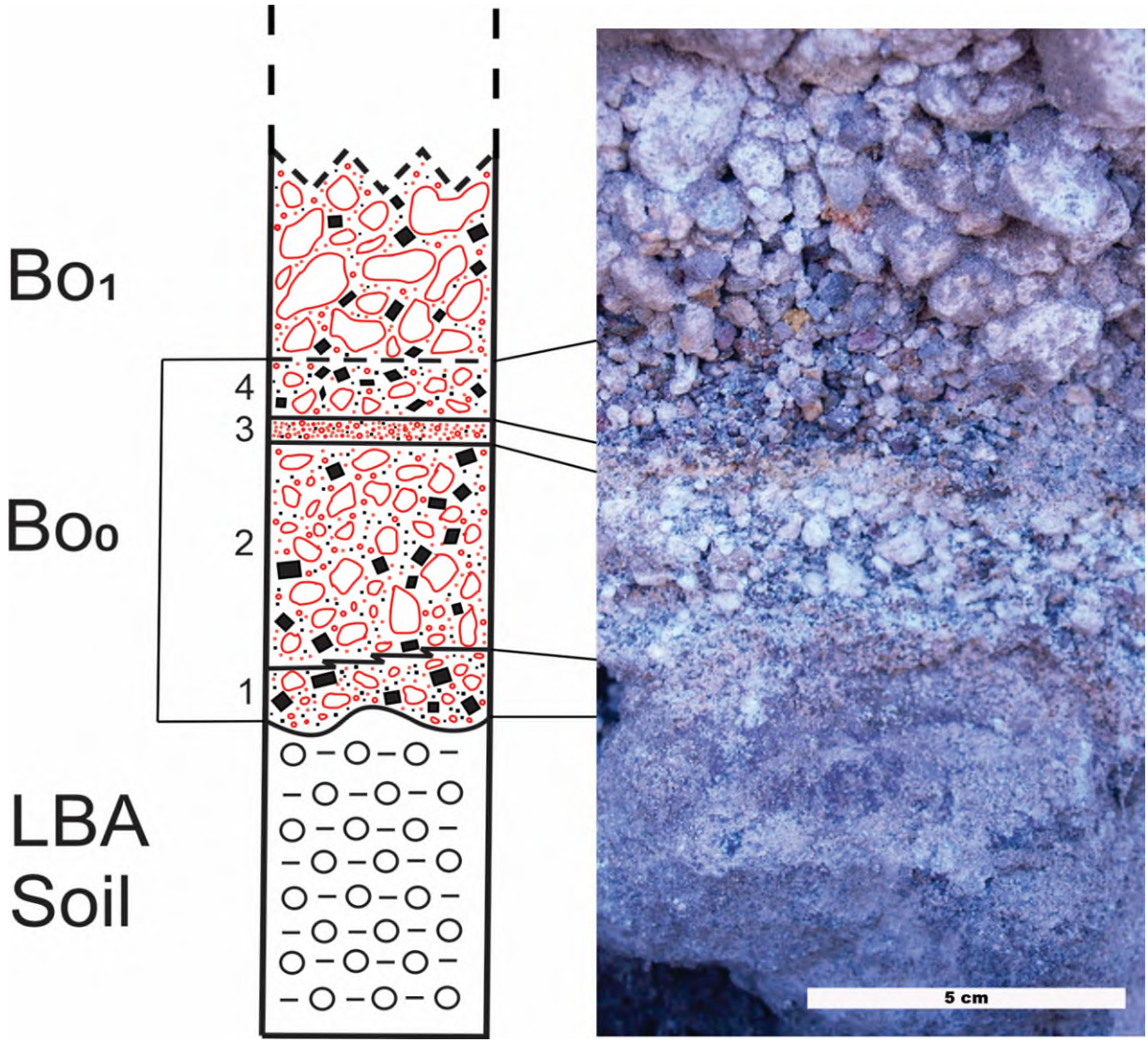

Figure 12 Precursory stratigraphic sequence. Four thin distinct layers of the precursory eruptive activity with a sharp contact with the underlying cultural soil layer and a gradual transition from pulse 4 into the first phase of the Plinian eruption (Bo1). The sharp contact between each pulse of the precursory activity indicates no significant 'time gap' between the individual pulses or the main Plinian eruption.

cultural soil layer. Precursory pulse 4 grades into Bo_1 of the larger Plinian eruption indicating a gradual shift in eruptive character with no break in activity.

Table 3 Stratigraphic layer descriptions of the precursory eruption.

Precursory Event	Sorting	Description
Pulse 4	Well	Light gray, fine lapilli to very coarse ash-rich tephra; sharp contact with pulse 3, grades into Phase 1
Pulse 3	Well	Yellowish brown, very coarse to coarse ash-rish tephra; sharp contact with pulses 2 and 4
Pulse 2	Well	White, fine lapilli to very coarse ash-rish tephra; sharp contact with pulses 1 and 3
Pulse 1	Well	Light brown, very coarse to coarse ash-rich tephra; sharp contact with underlying cultural soil and pulse 2

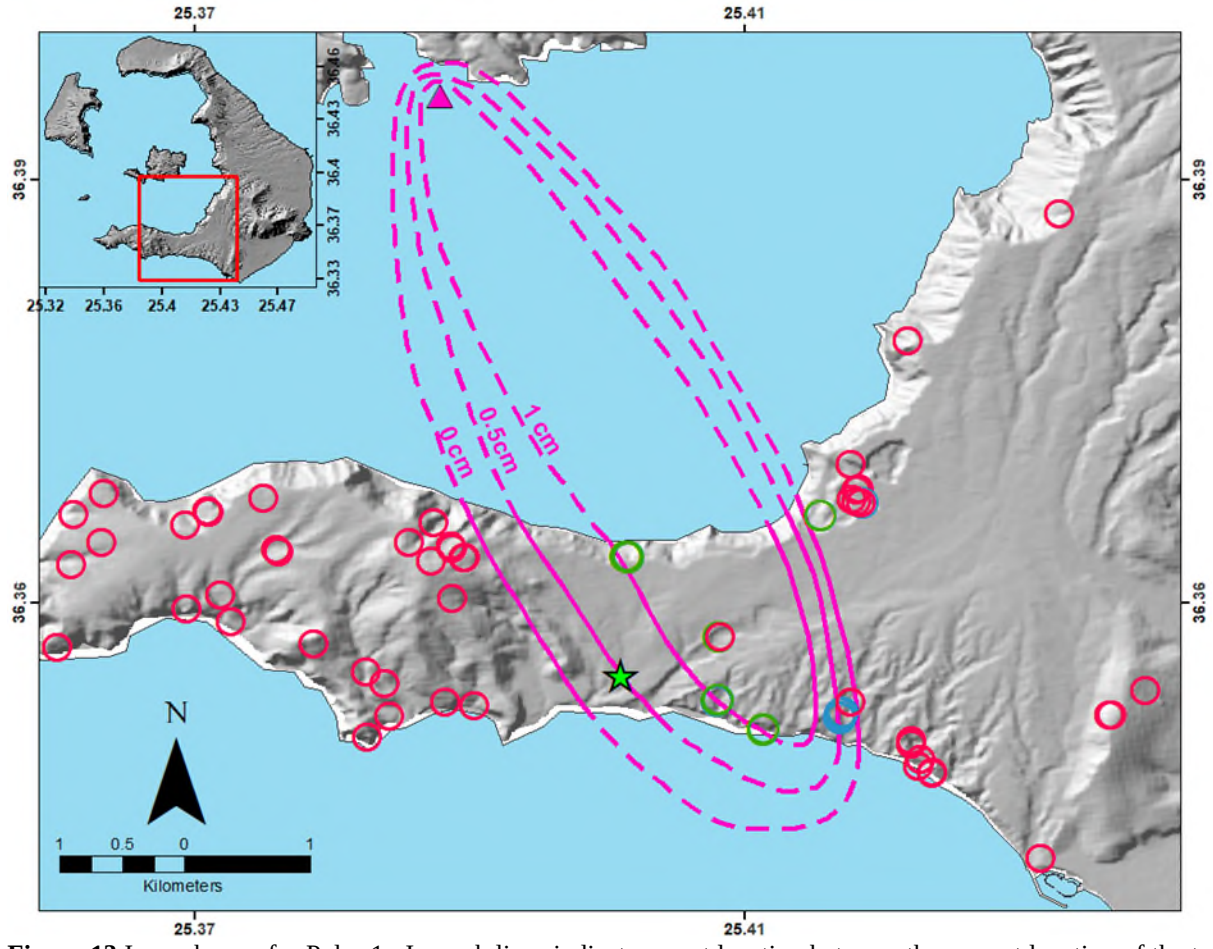

Figure 13 Isopach map for Pulse 1. Isopach lines indicate a vent location between the current location of the two Kameni islands with a deposition of tephra to the southeast. The green circles indicate a thickness measurement of 1 cm; blue circles indicate a thickness measurement of 0.5 cm; and red circles indicates Pulse 1 was not observed at that location. The dashed line of the isopachs indicate these are inferred and solid line indicates the isopach can be constrained from field data. Basemap DEM from Paraskevas et al. (2019).

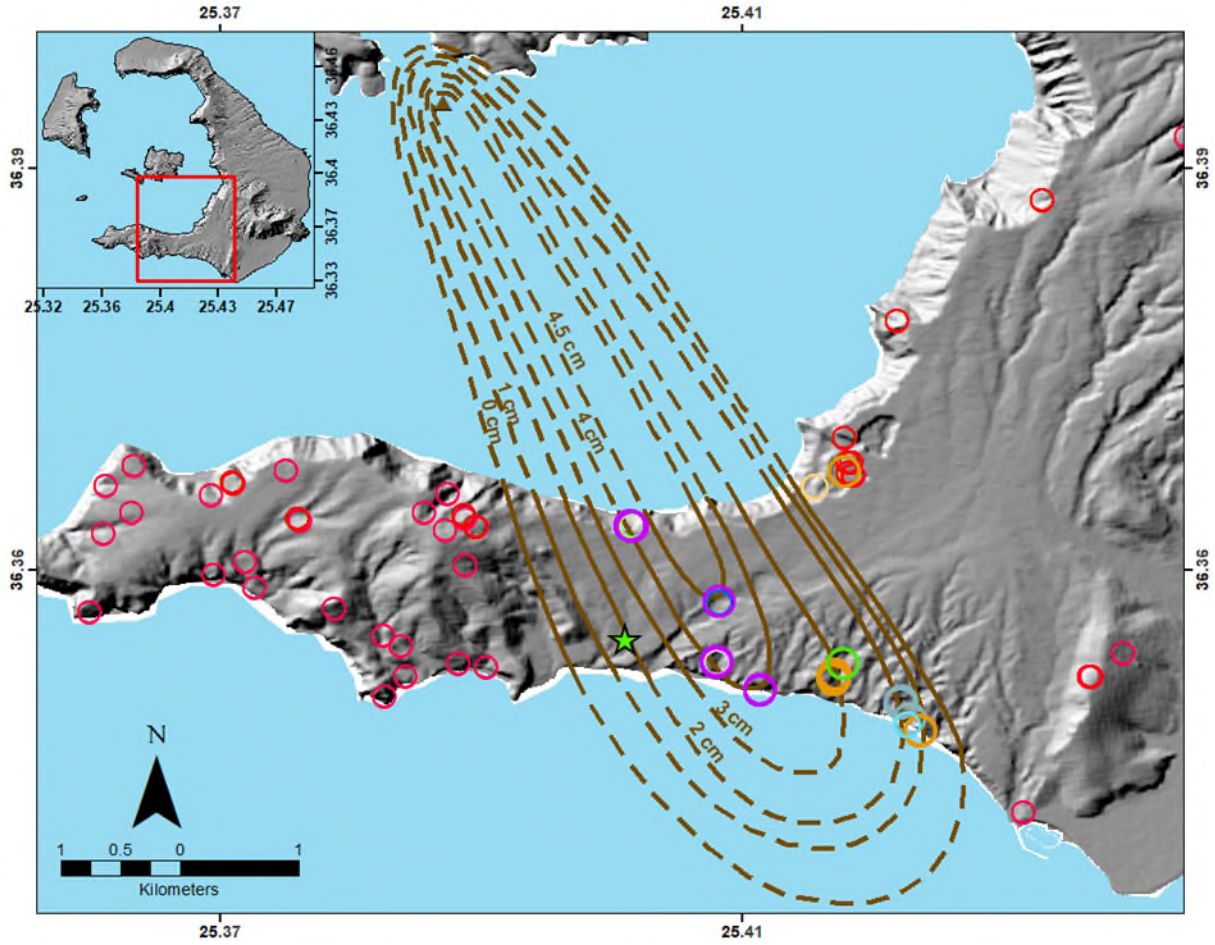

Figure 14 Isopach map for Pulse 2. Isopach lines indicate a vent location between the current location of the two Kameni islands with a deposition of tephra to the southeast. Red circles indicate Pulse 2 was not observed at that location; other circles indicate a thickness ranging between 0.5 and 4.5 cm. The dashed line of the isopachs indicate these are inferred and solid line indicates the isopach can be constrained from field data. Basemap DEM from Paraskevas et al. (2019).

Isopach maps of individual tephra fall layers show that, during the precursory eruptive activity, the first pulse is aligned on an azimuth of ~299° and extends to ~6.3 km with an elliptical depositional pattern (**Figure 13**). Pulse 1 was observed at two locations to the north of the tephra fall isopach lines at a thickness of 0.5 cm and 1 cm. These measurements were taken in the Akrotiri Quarry along the caldera rim. The thicker of the two observations, where samples were collected, was located closer to the inferred vent location and slightly to the southwest. Between these two measurements, Pulse 1 was not observed as an existing stratigraphic layer except in the back of the quarry where it was measured at 0.5 cm thick. This suggests some form of lateral deposition or lateral erosion of the deposit in this area.

Pulse 2 also has an elliptical deposition pattern along an azimuth of ~300° and extends ~7.3 km (**Figure 14**). Similarly, Pulse 2 was observed in the same region as Pulse 1 to the north of the tephra fall isopach lines at a thickness of 0.5 and 1 cm. The thinner of the two measurements was located closer to the inferred vent location and slightly to the southwest. Between these two measurements, Pulse 2 was occasionally observed as a few grains at the base of Pulse 3. At the back of the quarry is where the thicker measurement of 1 cm was collected. As sharp bedding structures suggest an ashfall deposit, varying thickness of the deposit suggests lateral deposition or erosion.

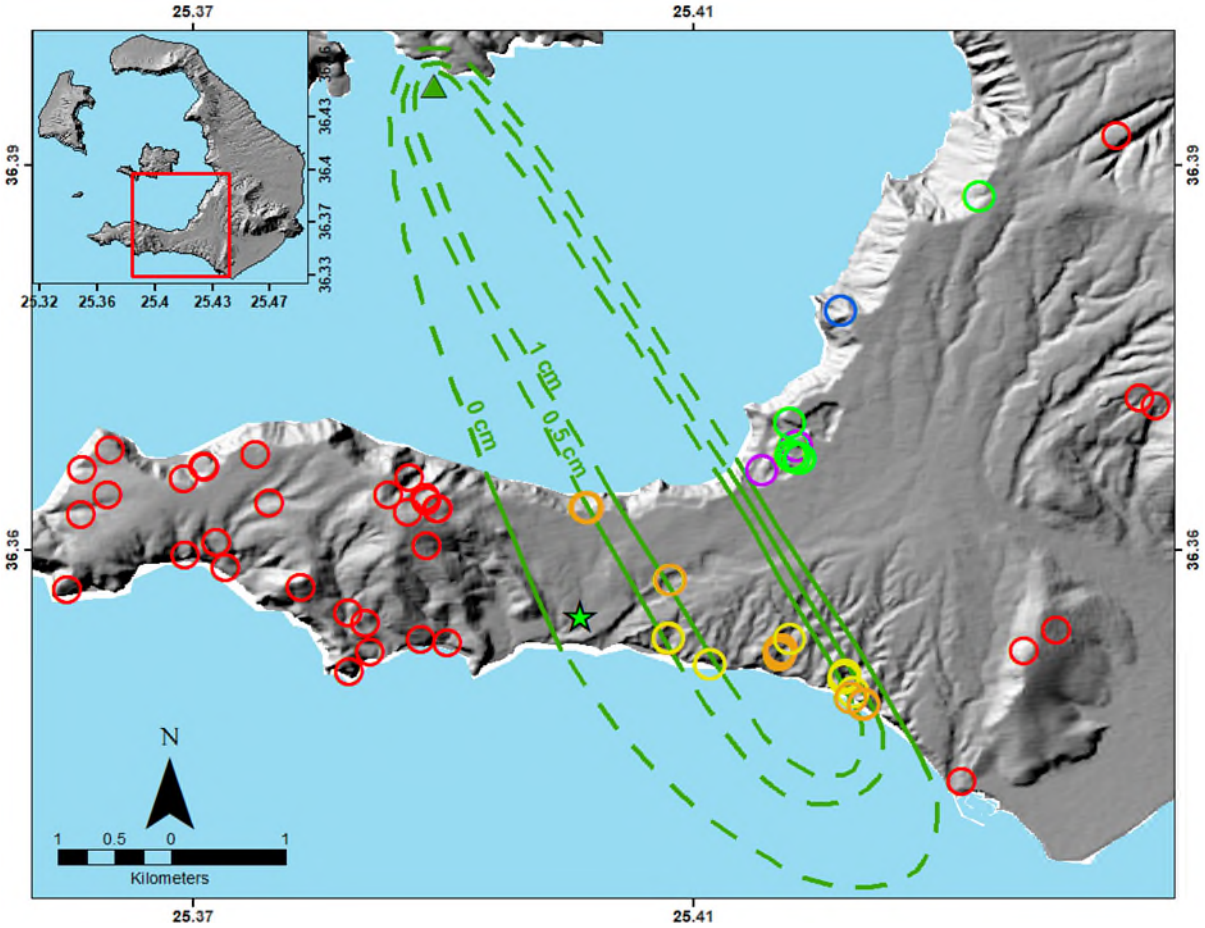

Figure 15 Isopach map for Pulse 3. Isopach lines indicate a vent location between the current location of the two Kameni islands with a deposition of tephra to the southeast. Orange circles indicate a thickness between 0.1 to 0.9 cm; yellow circles indicate a thickness between 1.0 to 1.9 cm; green circles indicate a thickness between 2.0 and 2.9 cm; purple circles indicate a thickness between 3.0 and 3.9 cm; blue circles indicate a thickness between 4.0 and 4.9 cm; and red circles indicate Pulse 3 was not observed at that location. The dashed line of the isopachs indicate these are inferred and solid line indicates the isopach can be constrained from field data. Basemap DEM from Paraskevas et al. (2019).

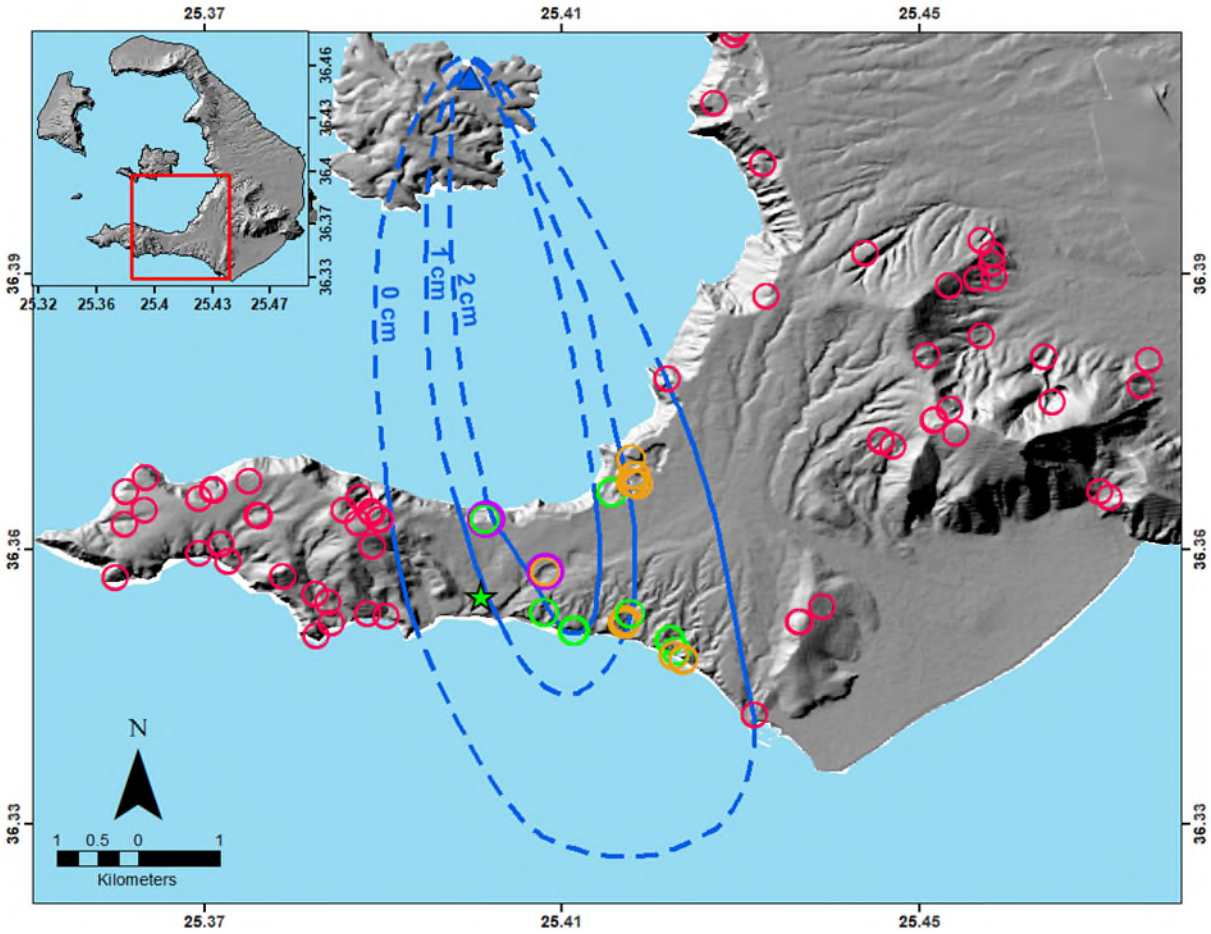

Figure 16 Isopach map for Pulse 4. Isopach lines indicate a vent location between the current location of the two Kameni islands with a deposition of tephra to the southeast. Orange circles indicate a thickness between 0.1 to 0.9 cm; green circles indicate a thickness between 1.0 to 1.9 cm; purple circles indicate a thickness between 2.0 and 2.5 cm; and red circles indicate Pulse 3 was not observed at that location. The dashed line of the isopachs indicate these are inferred and solid line indicates the isopach can be constrained from field data. Basemap DEM from Paraskevas et al. (2019).

Pulse 3 also has an elliptical deposition pattern along an azimuth of ~301° and extends ~7.7 km (**Figure 15**). Pulse 3 was mapped with significant thicknesses to the north but are not included in the isopach maps. Based on laboratory analysis, these Pulse 3 deposits located to the north do not indicate a fall deposit but deposition by a PDC. Pulse 4 has an elliptical shape along an azimuth of ~281 and extends ~9.7 km with a shift in vent location to the northeast (**Figure 16**).

Tephra volume calculations for each pulse are based on measurements of tephra fall isopach areas (**Table 4**). Because no data was obtained for individual layers in the proximal regions, it is assumed the integrated volumes only reflect medial and distal thinning trends of these deposits. Tephra volume for Pulse 1 was calculated excluding and including the 0.01 cm isopach line since this could not be constrained in the field to represent the exact area of the 0.01 cm isopach line at

the time of the eruption. In relation to the 1 cm and 0.5 cm isopach lines, the 0.01 cm isopach line is below the trend lines (**Figure 17**). The range of volume estimates, obtained from the Exponential (Pyle 1989, 1995) Power-Law (Bonadonna and Houghton 2005), and Weibull techniques (Bonadonna and Costa 2012), measured in units of 10^{-3} km^3 for Pulse 1 using 2 versus 3 isopachs is (a) 0.20 and 0.69; (b) 0.54 and 7.7; and (c) 0.70 and 0.81.

Table 4 Volume calculations for each layer as calculated using different models.

Unit	Pulse 1	Pulse 1	Pulse 2	Pulse 3	Pulse 4
Number of Isopachs	2	3	6	3	3
Erupted volume (km^3)					
Exponential Thinning*	2.0E-04	6.9E-04	4.7E-04	3.0E-04	9.40E-04
T_0	0.1573	1.7816	0.1171	0.4939	0.4678
k	1.248	2.268	0.704	1.814	0.996
Power Law**	5.4E-04	7.7E-03	8.9E-05	3.3E-04	5.00E-03
PL-coefficient (T_{PL})	0.1156	1.3229	0.0646	0.4638	3.4822
PL-exponent (m)	3.089	5.937	1.313	4.961	4.435
Proximal Limit	2.208	2.208	1.124	2.131	3.073
Distal Limit	2.276	3.203	3.125	3.410	6.134
Weibull Method***	7.0E-04	8.1E-04	3.6E-04	3.5E-04	7.3E-04
θ	1.816	69.3303	6.1579	23.075	13.9943
λ	2.5142	1.0817	2.4034	1.230	2.2868
n	0.3283	2.000	2.000	2.000	2.000

*Calculated through the combination of the volume calculated for the one segment, following the method of Pyle (1989): $T(x)=T_0e^{-k\sqrt{A}}$

**Calculated following the approach of Bonadonna and Houghton (2005). T_{PL} and m are the coefficient and exponent of the power law. Here we used both proximal (C) and distal (B) limits of integration, following the equation: $T(x)=T_{PL}A^{-0.5m}$; $V=(2T_{PL}/(2-m))[C^{(2-m)}-B^{(2-m)}]$

***Calculated as used in the Weibull function integration (Bonadonna and Costa 2012). $V=2(\theta\lambda^2/n)$

Tephra volume for Pulse 2 was calculated without including the 0.1 cm isopach line since this could not accurately be constrained in the field to represent the exact area of the 0.1 cm isopach line at the time of the relation. In relation to the remaining isopach lines, the 0.1 cm isopach line is below the trend lines (**Figure 17**). The volume estimates obtained from the Exponential (Pyle 1989, 1995), Power-Law (Bonadonna and Houghton 2005), and Weibull techniques (Bonadonna and Costa 2012), measured in units of 10^{-4} km^3 are (a) 4.7; (b) 0.89; and (c) 3.6.

Tephra volume for Pulses 3 and 4 were calculated with including the 0.01 cm and 0.1 cm isopach lines, respectively. These isopach lines fit with the exponential thinning trends of the rest of the deposit (**Figure 17**). The volume estimates obtained from the Exponential (Pyle 1989, 1995), Power-Law (Bonadonna and Houghton 2005), and Weibull techniques (Bonadonna and Costa 2012), measured in units of 10^{-4} km^3 for Pulse 3 and 4, respectively, are (a) 3.0 and 9.4; (b)

3.3 and 50.0; and (c) 3.5 and 7.3. The considerable variability of results of the Weibull method can be attributed to the lack of proximal data and poorly distributed data set, which can result in a discrepancy of 99%.

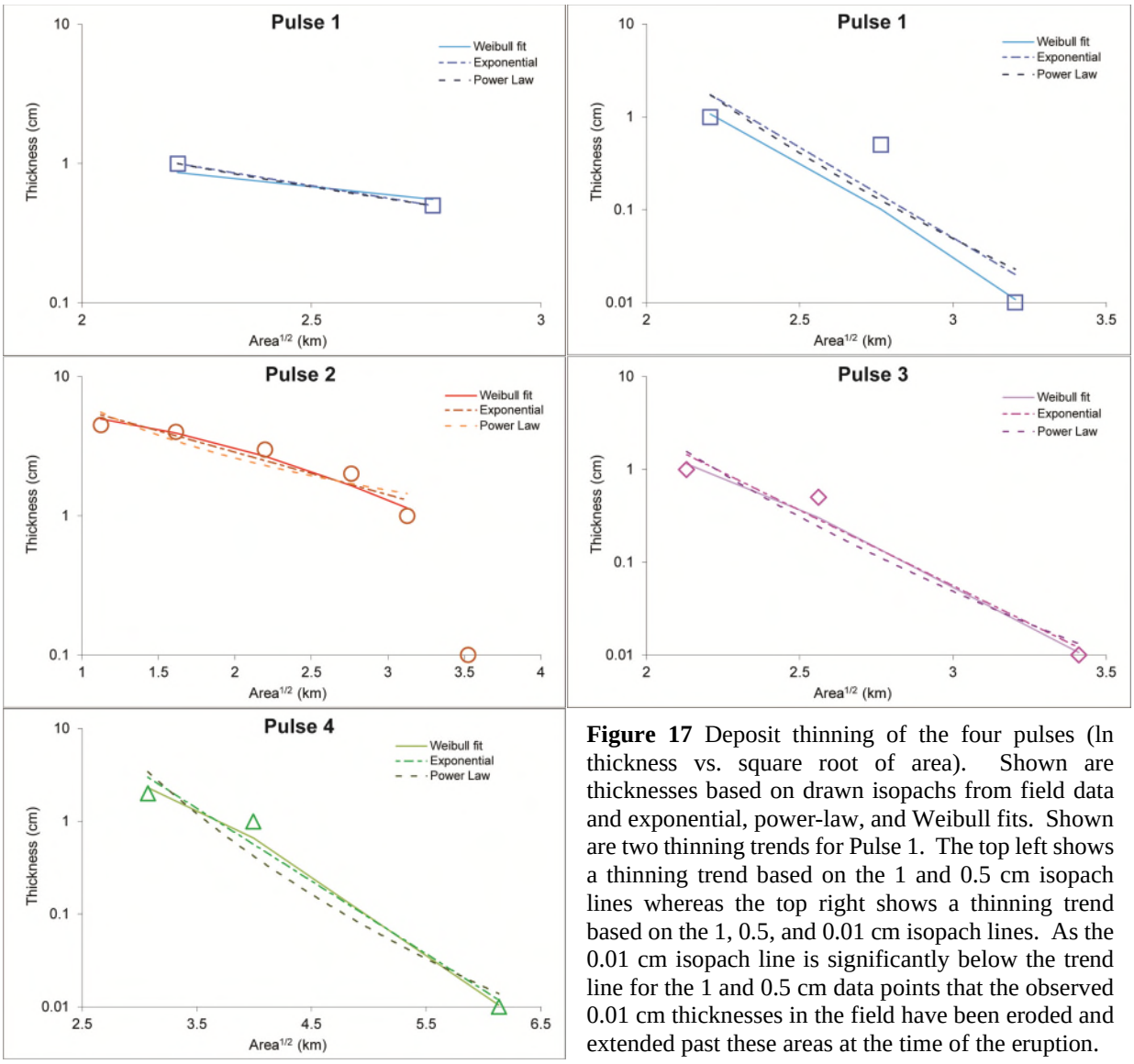

Figure 17 Deposit thinning of the four pulses (ln thickness vs. square root of area). Shown are thicknesses based on drawn isopachs from field data and exponential, power-law, and Weibull fits. Shown are two thinning trends for Pulse 1. The top left shows a thinning trend based on the 1 and 0.5 cm isopach lines whereas the top right shows a thinning trend based on the 1, 0.5, and 0.01 cm isopach lines. As the 0.01 cm isopach line is significantly below the trend line for the 1 and 0.5 cm data points that the observed 0.01 cm thicknesses in the field have been eroded and extended past these areas at the time of the eruption.

4.2 Grain Size

Sieve analyses were carried out on ten medial to distal sample deposits of Pulse 1 (**Figure 18**; **Table 5**). Grain-size distribution, median grain size, and sorting indicate eight of the samples collected from Pulse 1 were of ash-fall depositional processes (**Figures 18** and **19**). Grain-size distribution, median grain size, and sorting of the two remaining samples, collected in the Akrotiri quarry, indicate lateral deposition or syn- and post-depositional reworking. Pulse 1 deposits are generally coarse ash (median diameter -0.30 to 0.64) and very well sorted (σ_ϕ is 0.86 to 1.56)

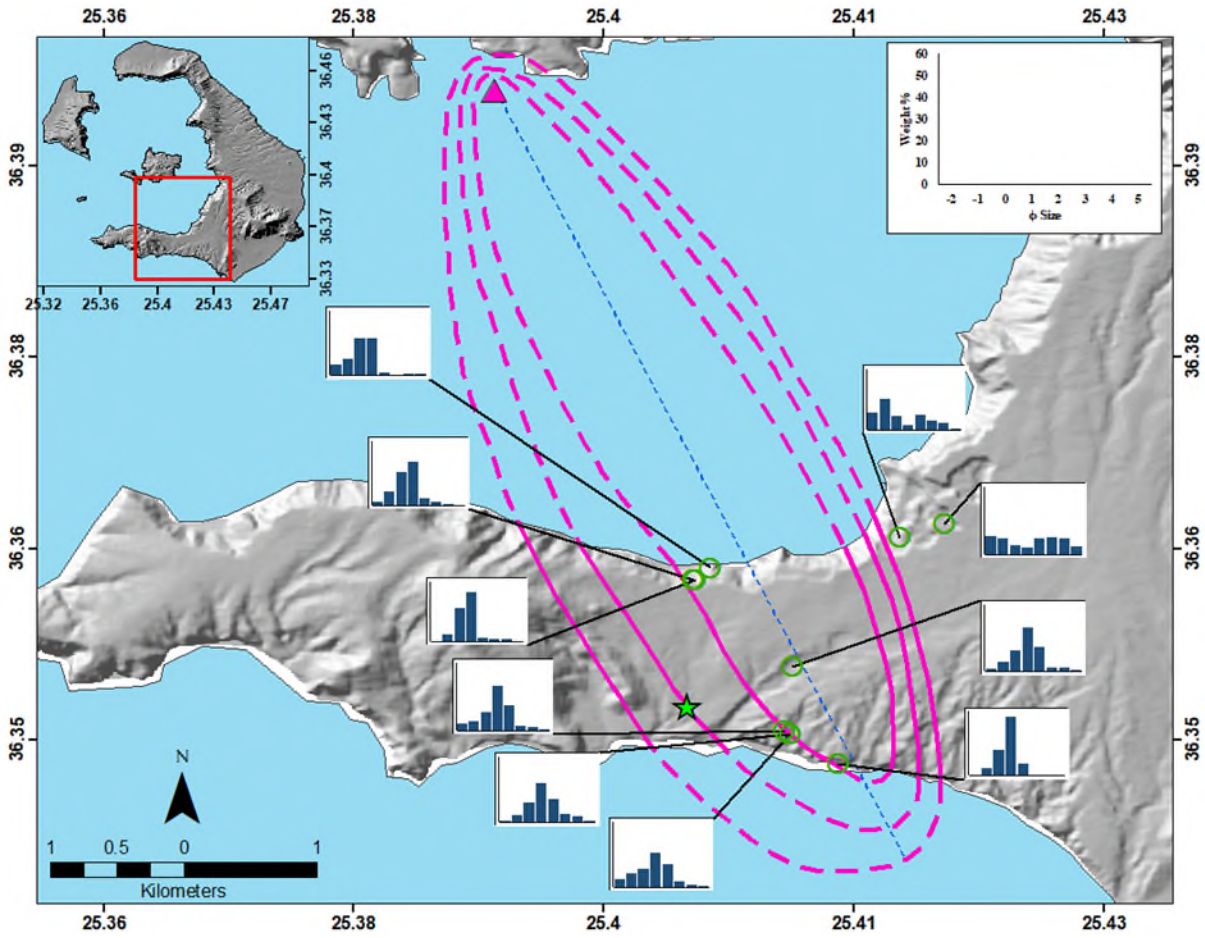

Figure 18 Grain-size distribution graphs of samples analyzed from Pulse 1. Isopach lines are denoted by the pink lines where the dashed lines being inferred. Green circles indicate sample locations with the black lines showing the grain-size distribution graph associated with the sample. Blue dashed line indicates the dispersal axis. The two samples not included in the isopach lines are suggested not to be deposited from ashfall, but from lateral deposition or erosion due to the bimodal distribution and the significant portion of fines compared to the other samples showing an origin of ashfall deposition. Basemap DEM from Paraskevas et al. (2019).

Table 5 Grain-size parameters for Pulse 1 samples.

Sample ID	Inferred Vent Distance (km)	x_ϕ	ϕ_{50}	σ_ϕ
071418-03A	3.8	-0.41	-0.3	1.16
062219-03A	3.9	0.01	0.09	1.12
062219-01A	3.9	0.11	0.18	0.99
062419-01A*	4.2	-0.19	-0.84	2.09
062419-04A*	4.2	1.07	1.6	2.51
061819-01A	4.7	-0.81	0.54	1.38
071718-02A	5.1	0.43	0.51	1.36
062319-01A	5.1	0.67	0.64	1.41
062319-02A	5.1	0.25	0.39	1.56
062319-05A	5.5	0.22	0.34	0.86

*Samples collected from Akrotiri Quarry. Sorting values ($\sigma\phi$) for these samples indicate this area of the deposit is not of tephra fall deposition.

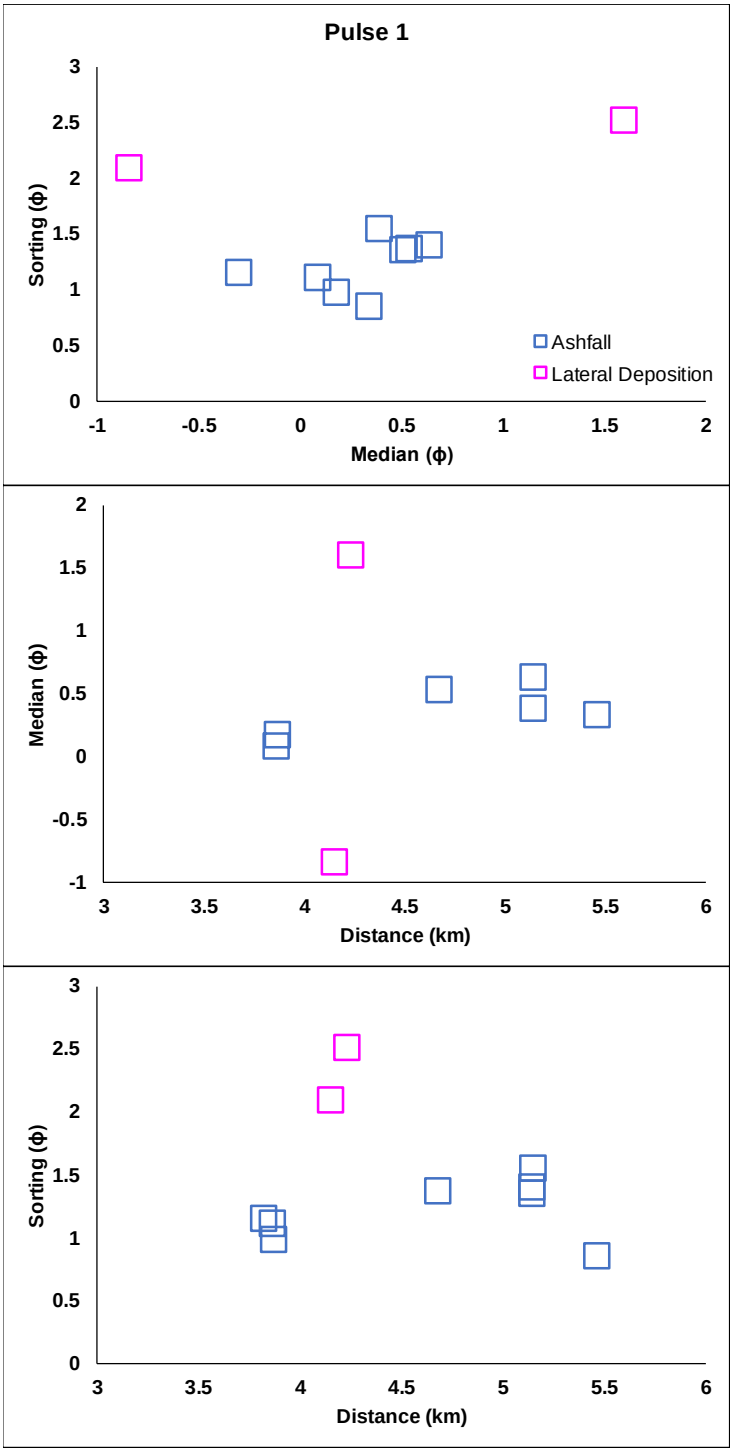

Figure 19 Grain-size characteristics of the Pulse 1 deposit. Top: Median diameter vs sorting; Middle: Distance from vent vs median diameter; and Bottom: Distance from vent vs sorting.

(Figure 19; **Table 5**). Grain-size analyses of Pulse 1 shows a unimodal distribution for eight of the samples analyzed, with a main mode ranging from 0ϕ to 1ϕ (**Figure 18**). Overall, the median grain size fines and the deposit becomes better sorted with increasing distance from the inferred vent location (**Figure 19**). These characteristics and trends of these Pulse 1 samples indicates deposition by ash-fall.

The two samples from the Akrotiri quarry (**Figure 18**) shows a bimodal distribution, with a mode ranging from-2ϕ to -1ϕ and 2ϕ to 3ϕ. The easternmost sample, collected from the back of the quarry, shows the highest bimodality and is a fine lapilli-rich (median diameter 1.60), poorly sorted (σ_ϕ is 2.51) tephra. Meanwhile, the west sample in the quarry, is a coarse ash-rich (median diameter -0.84), poorly sorted (σ_ϕ is 2.09) tephra. This west sample of the quarry samples is coarser, slightly better sorted, and shows lower bimodality than the easternmost deposit. These characteristics in this area indicates lateral deposition or erosion. The higher degree of poorly sorting, finer materials, and high bimodality of the easternmost deposit indicates a higher degree

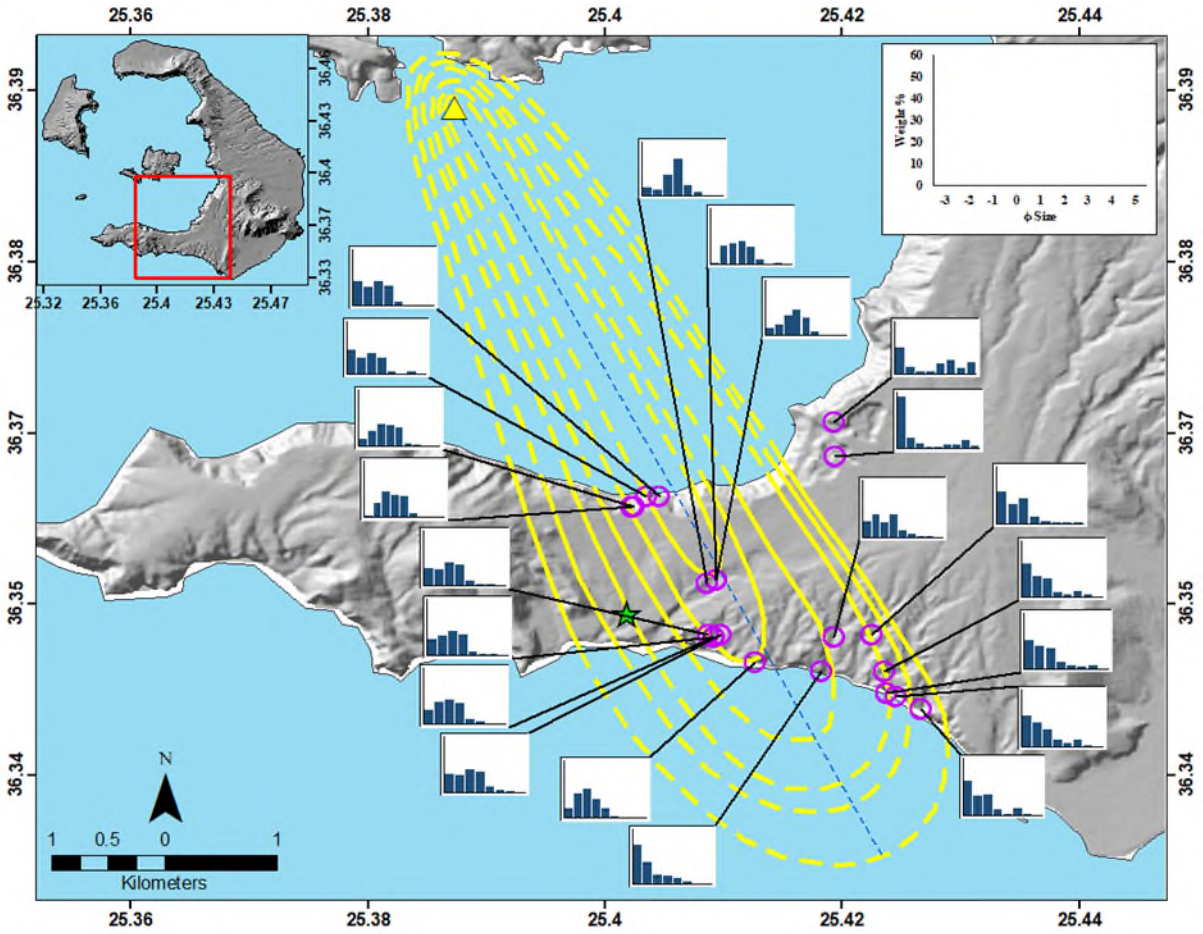

Figure 20 Grain-size distribution graphs of samples analyzed from Pulse 2. Isopach lines are denoted by the yellow lines where the dashed lines being inferred. Purple circles indicate sample locations with the black lines showing the grain-size distribution graph associated with the sample. Blue dashed line indicates the dispersal axis. Basemap DEM from Paraskevas et al. (2019).

of lateral transportation for the coarser materials to abrade as seen in the high percentages of finer material (**Figure 18**).

Sieve analyses were conduct on twenty-one samples collected from medial and distal deposits of Pulse 2 (**Figure 20**; **Table 6**). Grain size distribution, median grain size, and sorting indicate nineteen of the samples collected from Pulse 2 were of ash-fall depositional processes (**Figures 20** and **21**). For the remaining two samples, grain size distribution, median grain size, and sorting indicate lateral deposition or syn- and post-depositional reworking. These two samples were collected in Akrotiri quarry, the same region as the two Pulse 1 samples previously discussed. Pulse 2 deposits are generally medium lapilli to coarse ash (median diameter -1.69 to 0.22) and well sorted (σ_ϕ is 1.27-1.78). Grain-size analyses of Pulse 2 generally shows a unimodal distribution with some bimodality in some of the samples, with a main mode ranging from -2ϕ to

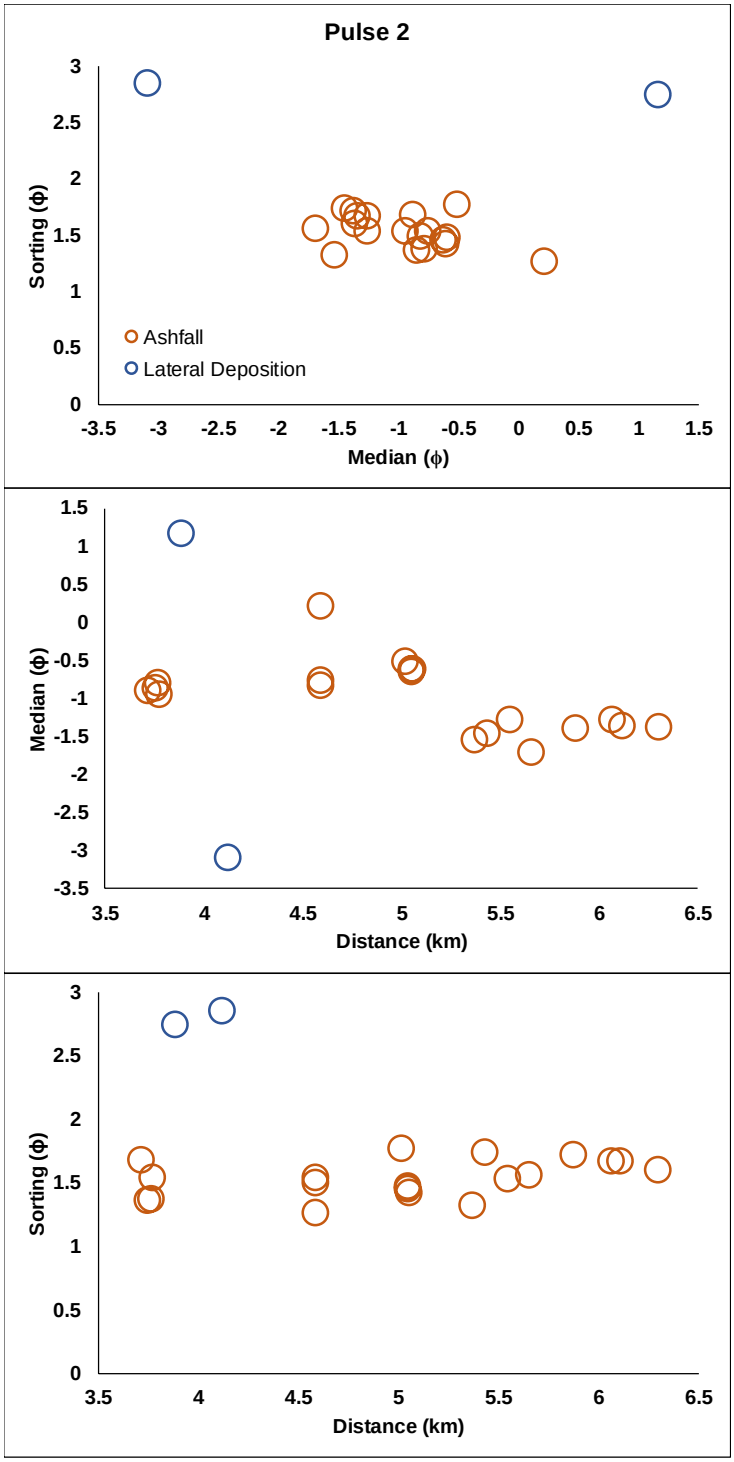

Figure 21 Grain-size characteristics of the Pulse 2 deposit. Top: Median diameter vs sorting; Middle: Distance from vent vs median diameter; and Bottom: Distance from vent vs sorting.

1ϕ. Samples that show a bimodal distribution have a main mode ranging from -3ϕ to 0ϕ and a second mode ranging from 0ϕ to 4ϕ. Overall, the median grain size fines with increasing distance from vent (**Figure 21**). Meanwhile, the sorting remains generally consistent with increasing distance from vent (**Figure 21**). These characteristics and trends of these nineteen Pulse 2 samples indicates deposition by ash-fall.

The two samples from the Akrotiri quarry (**Figure 20**) shows bimodal and trimodal distribution with a mode ranging from -3ϕ to -2ϕ, 3ϕ to 4ϕ, and 5ϕ. The northernmost sample, collected at a slightly higher elevation in the quarry, shows the trimodal distribution and is a coarse ash-rich (median diameter 1.17), poorly sorted (σ_ϕ is 2.74) tephra. The south sample of the quarry is coarser, slightly better sorted, and shows bimodal distribution. These characteristics in this area indicates lateral deposition or erosion. The higher degree of poorly sorting, finer materials, and trimodal distribution of the northernmost deposit

indicates a higher degree of lateral transportation for the coarser materials to abrade as seen in the high percentages of finer material (**Figure 20**).

Table 6 Grain-size parameters for Pulse 2 samples.

Sample ID	Inferred Vent Distance (km)	x_ϕ	ϕ_{50}	σ_ϕ
071418-03B	3.7	-0.87	-0.88	1.68
071418-04B	3.7	-0.89	-0.85	1.37
062219-03B	3.8	-0.74	-0.79	1.38
062219-01B	3.8	-0.95	-0.94	1.54
071818-01B*	3.9	0.86	1.17	2.74
062419-07B*	4.1	-1.36	-3.09	2.85
061819-02B	4.6	-0.81	-0.82	1.50
061819-01B	4.6	-0.81	-0.75	1.54
071718-01B	4.9	0.07	0.22	1.27
071718-02B	5.0	-0.58	-0.51	1.78
071718-03B	5.0	-0.67	-0.6	1.48
062319-01B	5.0	-0.66	-0.63	1.46
062319-02B	5.1	-0.61	-0.61	1.43
062319-05B	5.4	-1.47	-1.53	1.33
062319-18B	5.4	-1.40	-1.45	1.74
072018-05B	5.5	-1.2	-1.26	1.53
071718-04B	5.7	-1.23	-1.69	1.56
072018-02B	5.9	-1.04	-1.38	1.72
072018-04B	6.1	-1.05	-1.26	1.67
072018-03B	6.1	-1.01	-1.34	1.67
072018-01B	6.3	-1.14	-1.37	1.61

*Samples collected from Akrotiri Quarry. Sorting values (σ_ϕ) for these samples indicate this area of the deposit is not of tephra fall deposition.

Table 7 Grain-size parameters for Pulse 3 samples.

Sample ID	Inferred Vent Distance (km)	x_ϕ	ϕ_{50}	σ_ϕ
062419-09C*	3.5	0.3	-0.05	2.26
071818-01C*	3.9	1.2	1.06	2.21
062419-08C*	3.9	2.46	2.75	2.44
062519-01C*	4.0	4.05	1.59	4.08
062419-02C*	4.1	1.24	1.76	2.01
062419-03C*	4.1	-1.21	-1.54	2.92
071818-02C*	4.1	1.14	1.11	2.61
062419-01C*	4.1	1.33	0.8	2.45
062419-07C*	4.1	0.02	0.09	3.01
071818-04C*	4.1	0.68	0.49	2.46
062419-06C*	4.1	0.49	0.41	1.89
062419-05C*	4.2	-0.48	-1.06	2.42
062419-04C*	4.2	1	0.88	2.33
071818-03C*	4.2	0.25	-0.34	2.69
071718-01C	5.0	-0.68	-0.64	1.39
071718-02C	5.1	0.08	0.02	1.22
062319-02C	5.1	0.44	0.27	1.64

*Samples collected from Akrotiri Quarry. Sorting values ($\sigma\phi$) for these samples indicate this area of the deposit is not of tephra fall deposition.

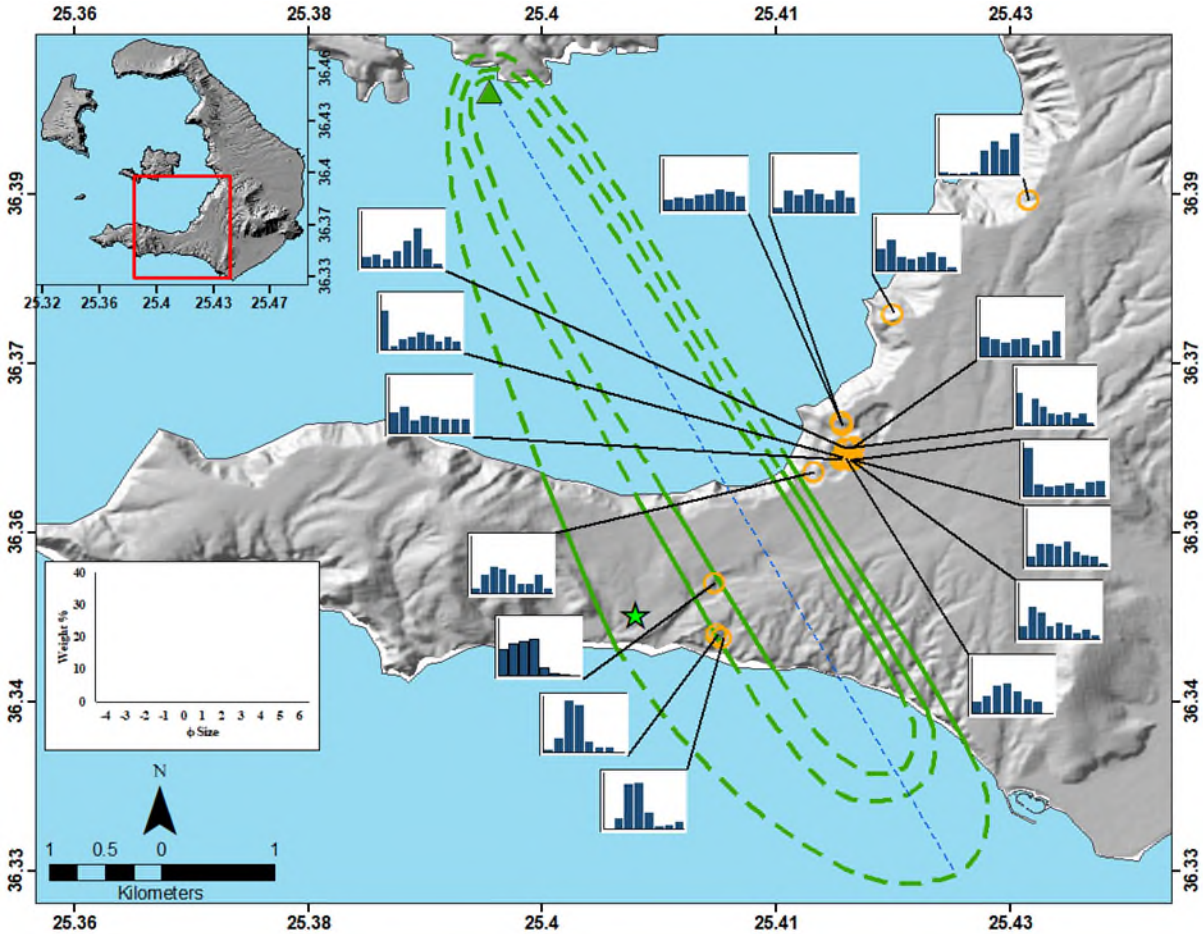

Figure 22 Grain-size distribution graphs of samples analyzed from Pulse 3. Isopach lines are denoted by the green lines where the dashed lines being inferred. Orange circles indicate sample locations with the black lines showing the grain-size distribution graph associated with the sample. Blue dashed line indicates the dispersal axis. Grain-size distributions of the samples collected to the north-northeast of the dispersal axis indicates deposition by pyroclastic density currents. Basemap DEM from Paraskevas et al. (2019).

Sieve analyses were carried out on seventeen medial to distal samples collected from the third layer, Pulse 3 (**Figure 22**; **Table 7**). Grain-size distribution, median grain size, and sorting indicate three of the samples collected from Pulse 3 were of ash-fall depositional processes (**Figures 22** and **23**) These deposits are generally coarse ash (median diameter -0.64 to 0.27) and very well sorted ($\sigma\phi$ is 1.22 to 1.64) (**Figure 23**). Grain-size analyses of the ash-fall deposit samples shows unimodal distribution with a main mode ranging between 0ϕ and 1ϕ (**Figure 22**). The median grain size fines with increasing distance from the inferred vent location (**Figure 23**). Generally, the deposit becomes better sorted with increasing distance from the inferred vent location (**Figure**

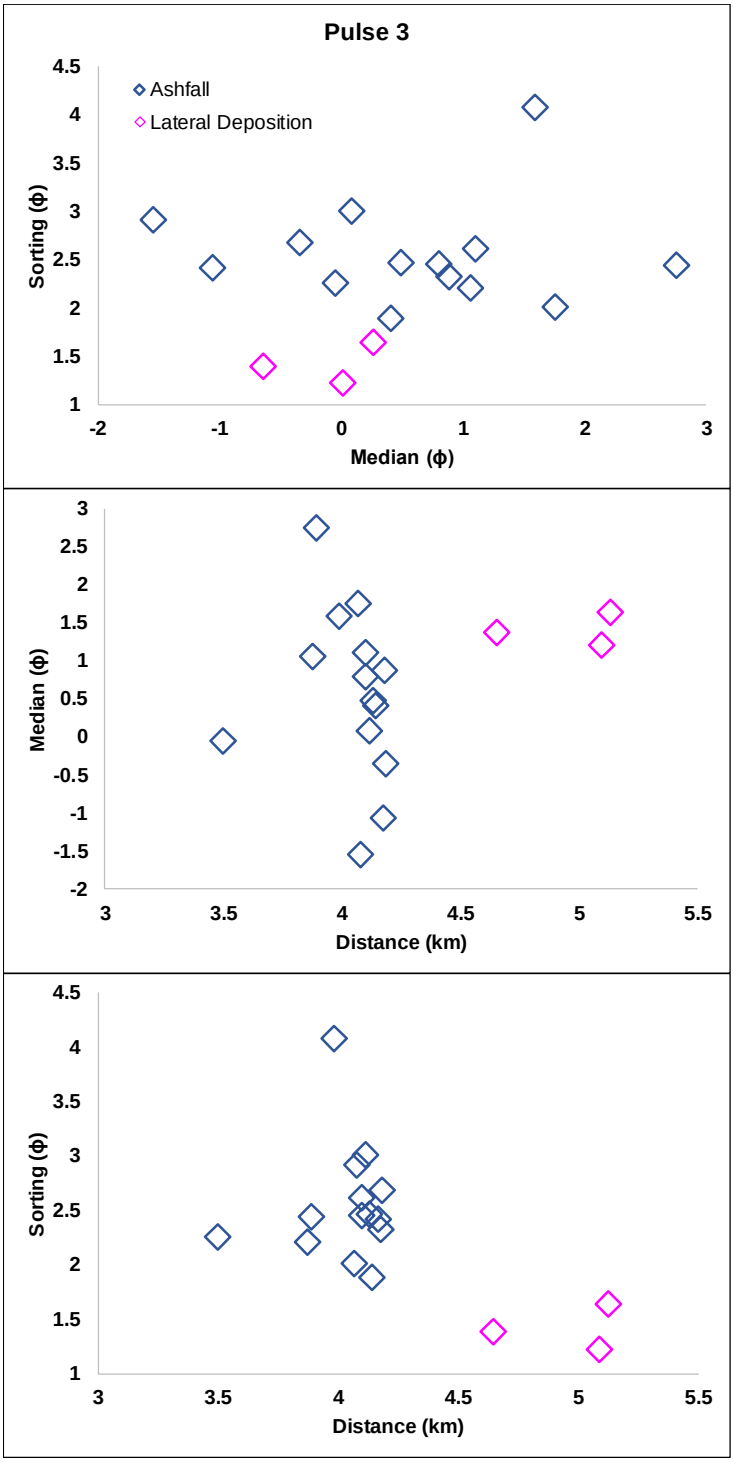

Figure 23 Grain-size characteristics of the Pulse 3 deposit. Top: Median diameter vs sorting; Middle: Distance from vent vs median diameter; and Bottom: Distance from vent vs sorting.

23). These characteristics and trends of the Pulse 3 samples supports an ash-fall depositional process.

The remaining samples were collected from the Akrotiri Quarry and further north along the caldera wall (**Figure 22**). These samples show high variability in grain size (unimodal to trimodal), median grain size (-1.54 to 2.75), and sorting (σ_ϕ is 1.89 to 4.08). These highly variable characteristics within the same area and at the same distance from the inferred vent indicate lateral deposition such as a PDC. As Pulses 1 and 2 indicate either lateral deposition or erosion, it is suggested since Pulse 1 was not observed at the front of the quarry and Pulse 2 is also thicker at a higher elevation and at the back of the quarry that Pulse 3 produced a PDC at an azimuth of 331°.

Sieve analyses were carried out on twenty-six (26) samples collected from the fourth layer, Pulse 4 (**Figures 24**; **Table 8**). Pulse 4 deposits are medium lapilli to coarse ash (median diameter -1.39 to 0.81) and very well sorted to poorly sorted (σ_ϕ is 0.80 to 2.59).

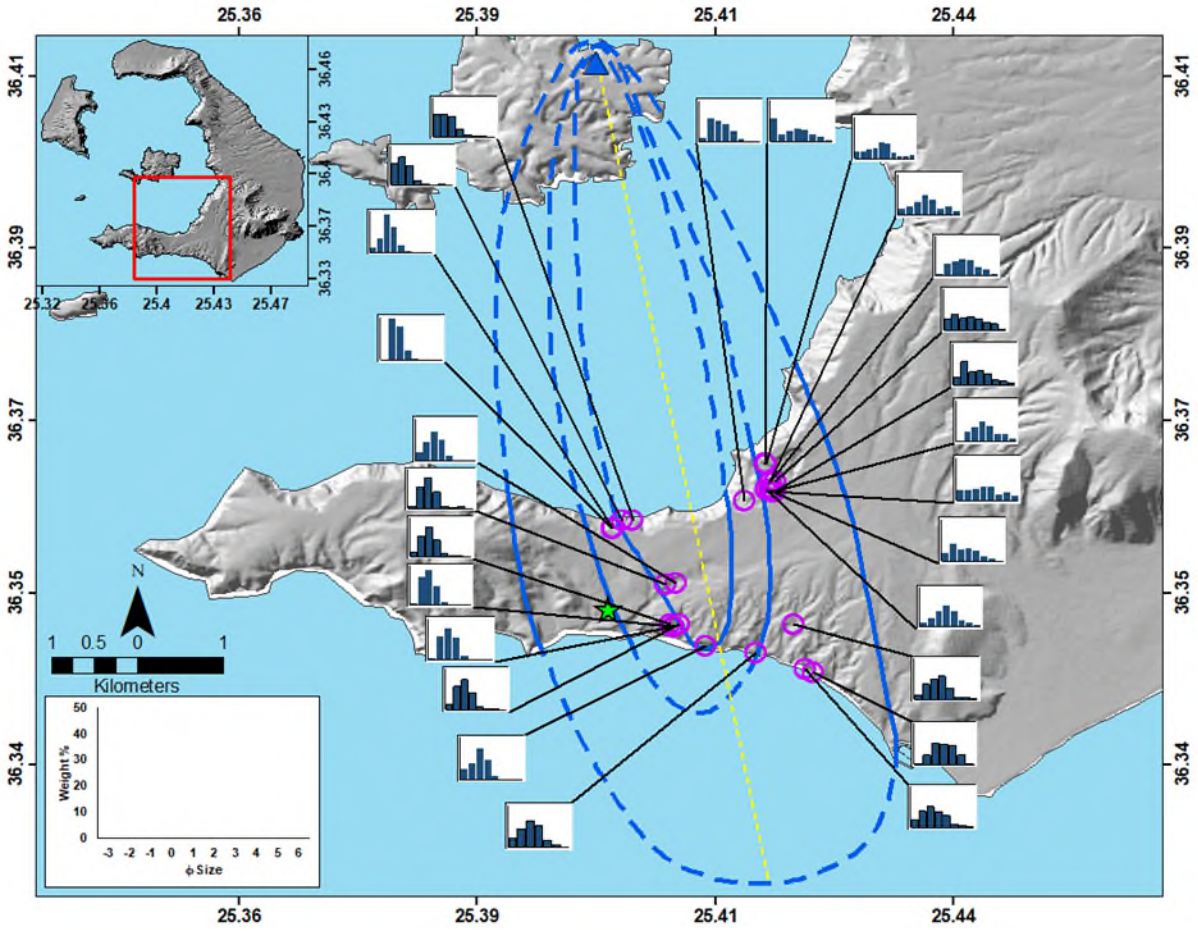

Figure 24 Grain-size distribution graphs of samples analyzed from Pulse 4. Isopach lines are denoted by the blue lines where the dashed lines being inferred. Purple circles indicate sample locations with the black lines showing the grain-size distribution graph associated with the sample. Yellow dashed line indicates the dispersal axis. Basemap DEM from Paraskevas et al. (2019).

Grain-size analyses of Pulse 4 shows a unimodal and bimodal distribution of the samples analyzed. Sixteen (16) of the samples show a unimodal distribution with a main mode ranging from -1ϕ to 1ϕ. The remaining ten (10) samples show a bimodal distribution with a main mode ranging from -2ϕ to 1ϕ and a second mode ranging from 1ϕ to 6ϕ. Similar to Pulses 1 through 3, the bimodal distribution is confined to most of the samples collected within the Akrotiri quarry. Unlike the rest of the samples to the south and west, these samples are not depleted of fines indicating agglutination in the fall deposits.

At a distance between 4.9 to 5.5 km from vent, the median grain-size ranges from -1.36 to 0.81 and the sorting ranges from very well sorted to poorly sorted (**Figure 25**). Generally, the samples become finer with increasing distance from vent at 6 km and more poorly sorted (**Figure 25**). As the median grain size of the deposit becomes finer, the deposit is more poorly sorted (**Figure 25**).

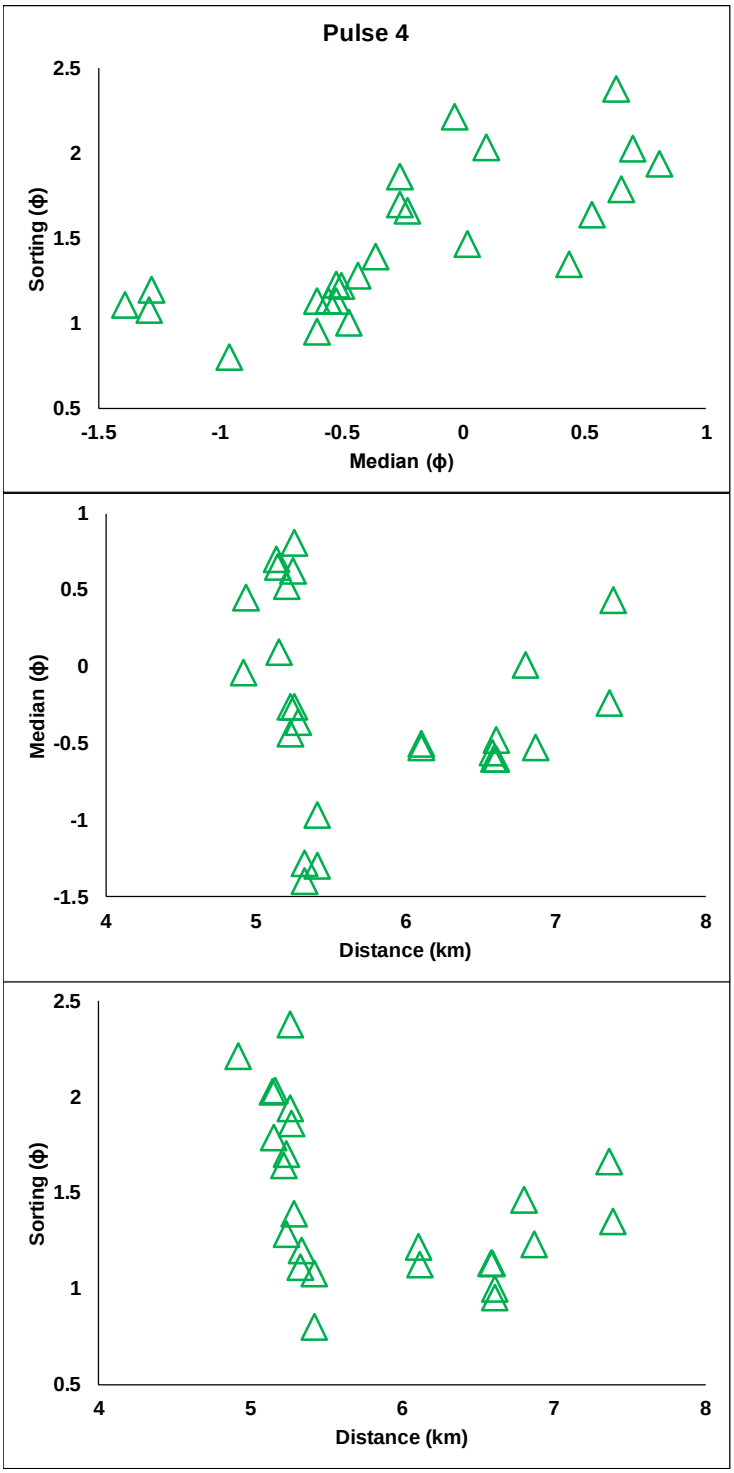

Figure 23 Grain-size characteristics of the Pulse 3 deposit. Top: Median diameter vs sorting; Middle: Distance from vent vs median diameter; and Bottom: Distance from vent vs sorting.

Table 8 Grain-size parameters for Pulse 4 samples.

Sample ID	Inferred Vent Distance (km)	x_ϕ	ϕ_{50}	σ_ϕ
071818-01D	4.9	-0.03	-0.04	2.21
062419-08D	4.9	0.36	0.45	2.59
062419-02D	5.1	0.85	0.70	2.03
062419-03D	5.2	0.71	0.65	1.79
071818-02D	5.2	0.21	0.10	2.03
062419-07D	5.2	0.53	0.53	1.64
062419-06D	5.2	-0.13	-0.26	1.70
071718-04D	5.2	-0.45	-0.43	1.28
062419-05D	5.2	0.74	0.63	2.38
062419-04D	5.3	1.04	0.81	1.94
071818-03D	5.3	-0.04	-0.26	1.86
062419-01D	5.3	-0.25	-0.36	1.39
071418-03D	5.3	-1.34	-1.39	1.11
071418-04D	5.3	-1.27	-1.28	1.20
062219-01D	5.3	-1.26	-1.29	1.08
062219-03D	5.4	-0.91	-0.96	0.80
061819-01D	5.4	-0.52	-0.50	1.22
071718-01D	6.1	-0.48	-0.52	1.13
071718-02D	6.6	-0.53	-0.55	1.13
071718-03D	6.6	-0.57	-0.60	1.13
062319-01D	6.6	-0.56	-0.60	0.95
062319-02D	6.6	-0.46	-0.47	1.00
072018-05D	6.6	-0.01	0.02	1.47
062319-05D	6.8	-0.57	-0.52	1.23
072018-04D	6.9	-0.12	-0.23	1.66
072018-03D	7.4	0.48	0.44	1.35

4.3 Tephra Componentry, Morphology, and Ratios

Analysis of components was undertaken on seventy-four (74) samples: ten (10) samples collected from layer 1, twenty-one (21) samples collected from layer 2, seventeen (17) samples collected from layer 3, and twenty-six (26) samples collected from layer 4. Three main categories were distinguished in each layer: lithic clasts, pumice, and crystals plus glass. There are several types of lithics, the two primary types are: (a) angular black glassy lava fragments from the Therasia series; and (b) angular red pumice from the Cape Riva eruption 22 kya. The crystals are dominantly angular, very fine grained (<1 mm) sanidine fragments and secondary crystals depending on the sample location. Samples collected along the coastline contain some salt crystals from wave action and evaporation. The glass fragments are angular, very fine grained (<1 mm), shiny fragments.

Analysis of Pulse 1 samples indicate the componentry is dominated by lithics with pumice and minor crystals/glass (**Figure 26**; **Table 9**). In samples where pumice dominates the coarser clast

componentry, the pumice exponentially decreases in the finer material. In cases where, samples contain only lithic fragments for -2ϕ, pumice increases in the -1ϕ grain size and tapers off in the finer grain sizes. The two samples collected from the Akrotiri quarry contain relatively equal portions of pumice and lithics for -2ϕ with pumice decreasing in the -1ϕ grain size before increasing for 0ϕ. This supporting lateral deposition or erosion of these two deposits and the abrasion of coarse pumice being deposited as finer pumice. Angular crystal/glass fragments appear in three samples at 0ϕ, while all samples contained crystal/glass fragments at 1ϕ which is also when lithics dominates the componentry in most samples. Samples collected from Akrotiri quarry contain more pumice and less glass or crystal fragments.

The Pulse 2 samples consist of pumice and lithics with some crystals/glass (**Figure 27**; **Table 10**). Pumice dominants the coarser grain sizes (-3ϕ to -1ϕ) while the finer grain sizes (0ϕ to 1ϕ) are comprised primarily of lithics (>50%) in most samples which is following the trend of Pulse 1. The two samples collected from Akrotiri quarry contains a wide range of pumice in the -2ϕ grain size but contains between 10 to 20% pumice in the -1ϕ grain size. The pumice content in these two samples increases in the finer material of 0ϕ and 1ϕ. Similar to Pulse 1, angular crystal/glass fragments were not seen in some samples above 0ϕ and most samples contained crystal/glass fragments at 1ϕ.

Pulse 3 samples are dominated by pumice with lithics and very little crystals/glass (**Figure 28**; **Table 11**). Pumice dominates the componentry of all phi sizes (>60%) in most samples. Very minor (<1%) amounts of crystals/glass appear in four of the samples analyzed at the 0ϕ size. In the samples suggested as fall deposits, pumice dominates the componentry in the -2ϕ grain size and decreases in the finer material. Whereas the remaining samples of lateral deposition remains generally consistent in pumice content at all grain sizes.

Pulse 4 samples, similar to Pulse 2, consists of pumice and lithics with some crystals/glass (**Figure 29**; **Table 12**). Pumice dominates the coarser grain sizes (-2ϕ to -1ϕ) while the finer grains (0ϕ to 1ϕ) are comprised primarily of lithics (>50%) in most samples. Crystals/glass is present in some of the samples at 0ϕ and present in most samples at 1ϕ. Samples collected from the fourth pulse contain more crystals/glass than the first three layers.

Table 9 Componentry ratios for Pulse 1 based on grain size -2ϕ to 1ϕ in one phi intervals. The abbreviations 'P', 'L', and 'C/G' means Pumice, Lithic, and Crystals and/or Glass, respectively. The results listed are in percent by number.

Sample ID	Inferred Vent Distance (km)	-2 Phi			-1 Phi			0 Phi			+1 Phi			Total		
		P	L	C/G	P	L	C/G	P	L	C/G	P	L	C/G	P	L	C/G
071418-03A	3.8	77.8	22.2	0.0	61.9	38.1	0.0	24.1	75.9	0.0	14.1	81.2	4.7	19.5	77.3	3.1
062219-03A	3.9	0.0	100.0	0.0	52.9	47.1	0.0	19.5	80.5	0.0	17.6	77.9	4.6	18.7	78.0	3.3
062219-01A	3.9	0.0	0.0	0.0	56.5	43.5	0.0	34.2	63.2	2.6	13.0	87.0	0.0	18.5	81.0	0.5
062419-01A*	4.2	30.0	70.0	0.0	24.6	75.4	0.0	47.7	52.3	0.0	40.2	57.4	2.5	40.0	58.3	1.7
062419-04A*	4.2	50.0	50.0	0.0	2.3	77.3	0.0	58.7	41.3	0.0	66.7	30.6	2.8	60.7	37.6	1.7
061819-01A	4.7	0.0	100.0	0.0	51.5	48.5	0.0	46.3	53.7	0.0	26.2	72.3	1.5	32.5	66.5	1.1
071718-02A	5.1	28.6	71.4	0.0	68.8	31.2	0.0	45.5	54.5	0.0	20.8	73.8	5.4	28.6	67.5	3.9
062319-01A	5.1	100.0	0.0	0.0	93.1	6.9	0.0	54.3	42.9	2.9	16.5	74.8	8.7	26.1	66.5	7.4
062319-02A	5.1	0.0	100.0	0.0	33.3	66.7	0.0	27.8	72.2	0.0	30.9	66.7	2.5	30.2	68.0	1.7
062319-05A	5.5	0.0	0.0	0.0	30.0	70.0	0.0	21.2	75.8	3.0	35.1	54.1	10.8	32.3	58.6	9.1

*Samples collected from Akrotiri Quarry.

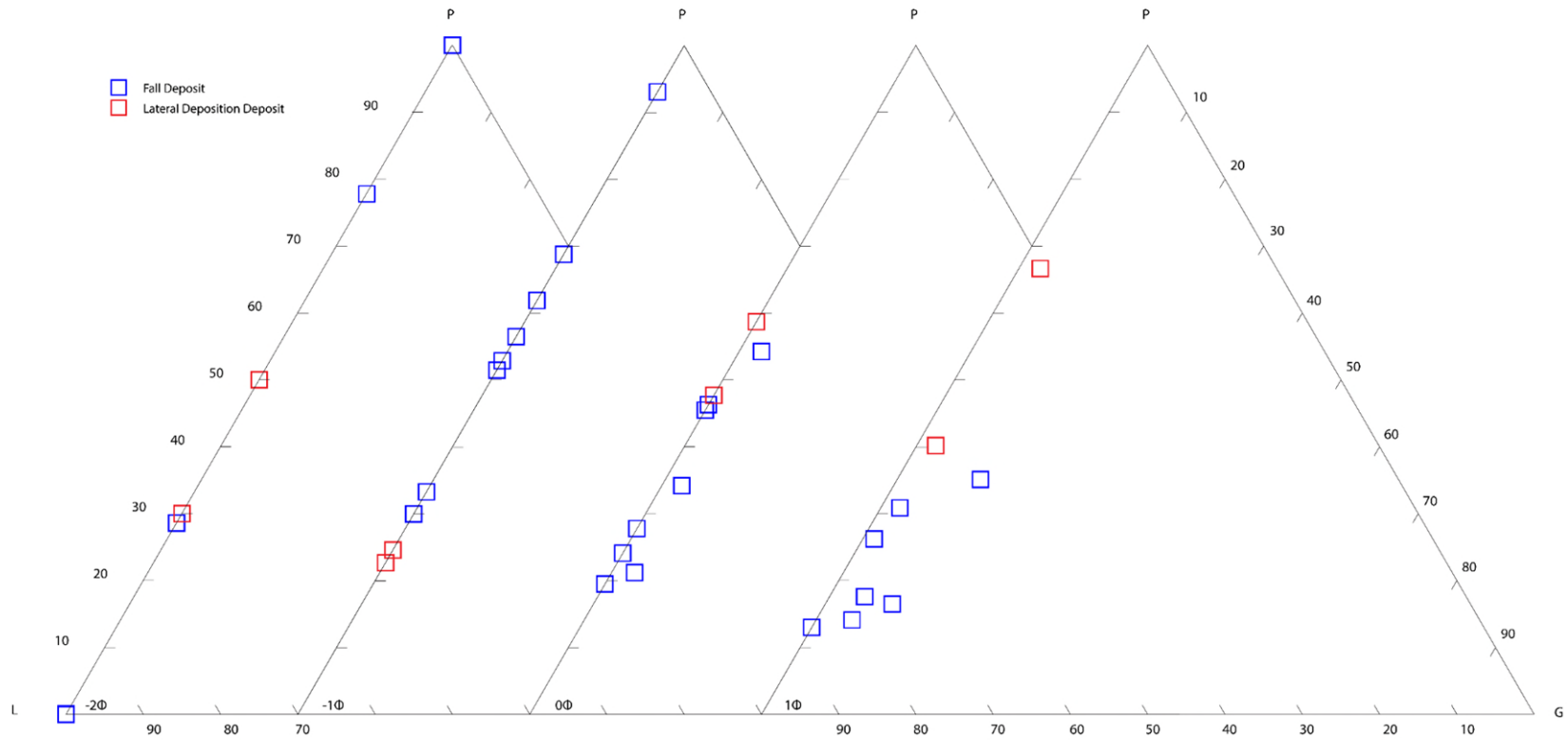

Figure 26 Relative proportion of pumice (P), lithics (L), and glass/crystals (G) as a function of the grain size (-2ϕ to 1ϕ) in the different deposition deposits of Pulse 1. Percentages are based on the number of grains of each component in the sample.

Table 10 Componentry ratios for Pulse 2 based on grain size -2ϕ to 1ϕ in one phi intervals. The abbreviations 'P', 'L', and 'C/G' means Pumice, Lithic, and Crystals and/or Glass, respectively. The results listed are in percent by number.

Sample ID	Inferred Vent Distance (km)	-3 Phi			-2 Phi			-1 Phi			0 Phi			+1 Phi			Total		
		P	L	C/G	P	L	C/G	P	L	C/G	P	L	C/G	P	L	C/G	P	L	C/G
071418-03B	3.7	0.0	0.0	0.0	95.3	4.7	0.0	76.1	23.9	0.0	33.3	65.3	1.3	25.6	60.5	14.0	46.5	48.6	4.9
071418-04B	3.7	0.0	0.0	0.0	100.0	0.0	0.0	82.7	17.3	0.0	35.9	64.1	0.0	18.4	75.0	6.6	35.2	61.6	3.3
062219-03B	3.8	100.0	0.0	0.0	96.8	3.2	0.0	87.8	12.2	0.0	60.2	39.4	0.4	28.4	56.7	14.9	55.2	39.8	4.9
062219-01B	3.8	100.0	0.0	0.0	100.0	0.0	0.0	89.6	10.4	0.0	58.9	40.4	0.7	37.5	51.6	10.9	60.9	35.2	4.0
071818-01B*	3.9	0.0	0.0	0.0	25.0	75.0	0.0	14.3	85.7	0.0	45.0	52.5	2.5	44.0	54.0	2.0	40.1	58.1	1.8
062419-07B*	4.1	100.0	0.0	0.0	83.3	16.7	0.0	18.2	81.8	0.0	52.0	48.0	0.0	68.4	24.5	7.1	66.6	27.3	6.1
061819-02B	4.6	100.0	0.0	0.0	100.0	0.0	0.0	85.5	14.5	0.0	47.6	52.4	0.0	45.5	54.5	0.0	57.8	42.2	0.0
061819-01B	4.6	100.0	0.0	0.0	100.0	0.0	0.0	89.2	10.8	0.0	42.8	56.6	0.7	10.7	75.0	14.3	43.8	51.5	4.8
071718-01B	4.9	0.0	0.0	0.0	90.0	10.0	0.0	70.0	30.0	0.0	29.8	70.2	0.0	20.6	70.6	8.8	28.1	66.7	5.3
071718-02B	5.0	0.0	0.0	0.0	98.9	1.1	0.0	90.5	9.5	0.0	38.2	41.2	20.6	40.0	41.0	18.3	66.5	26.4	7.1
071718-03B	5.0	0.0	0.0	0.0	98.9	1.1	0.0	91.9	8.1	0.0	22.2	77.8	0.0	35.3	52.9	11.8	59.6	36.3	4.1
062319-01B	5.0	0.0	0.0	0.0	100.0	0.0	0.0	80.8	19.2	0.0	39.7	60.3	0.0	42.9	47.1	10.0	47.3	48.5	4.2
062319-02B	5.1	0.0	0.0	0.0	100.0	0.0	0.0	91.2	8.8	0.0	34.5	62.8	2.7	45.0	49.0	6.0	46.5	49.4	4.1
062319-05B	5.4	100.0	0.0	0.0	96.0	4.0	0.0	91.0	9.0	0.0	48.0	52.0	0.0	61.8	36.3	2.0	60.2	39.0	0.8
062319-18B	5.4	100.0	0.0	0.0	100.0	0.0	0.0	69.2	30.8	0.0	53.3	64.1	0.6	65.0	29.0	6.0	56.7	39.5	3.9
072018-05B	5.5	0.0	0.0	0.0	100.0	0.0	0.0	70.9	29.1	0.0	22.0	76.3	1.7	27.8	59.3	13.0	41.5	53.2	5.3
071718-04B	5.7	0.0	0.0	0.0	100.0	0.0	0.0	94.7	5.3	0.0	57.1	42.9	0.0	48.4	39.1	12.5	59.2	33.3	7.4
072018-02B	5.9	0.0	0.0	0.0	100.0	0.0	0.0	77.7	22.3	0.0	22.9	77.1	0.0	59.6	29.8	10.6	52.1	44.4	3.5
072018-04B	6.1	0.0	0.0	0.0	97.4	2.6	0.0	86.8	13.2	0.0	12.5	82.5	5.0	49.0	34.7	16.3	50.1	42.1	7.8
072018-03B	6.1	0.0	0.0	0.0	98.1	1.9	0.0	94.1	5.9	0.0	24.6	69.6	5.8	54.5	34.1	11.4	57.4	38.2	4.4
072018-01B	6.3	0.0	0.0	0.0	100.0	0.0	0.0	82.3	17.7	0.0	36.6	57.3	6.1	36.0	57.3	6.7	49.9	45.5	4.6

*Samples collected from Akrotiri Quarry.

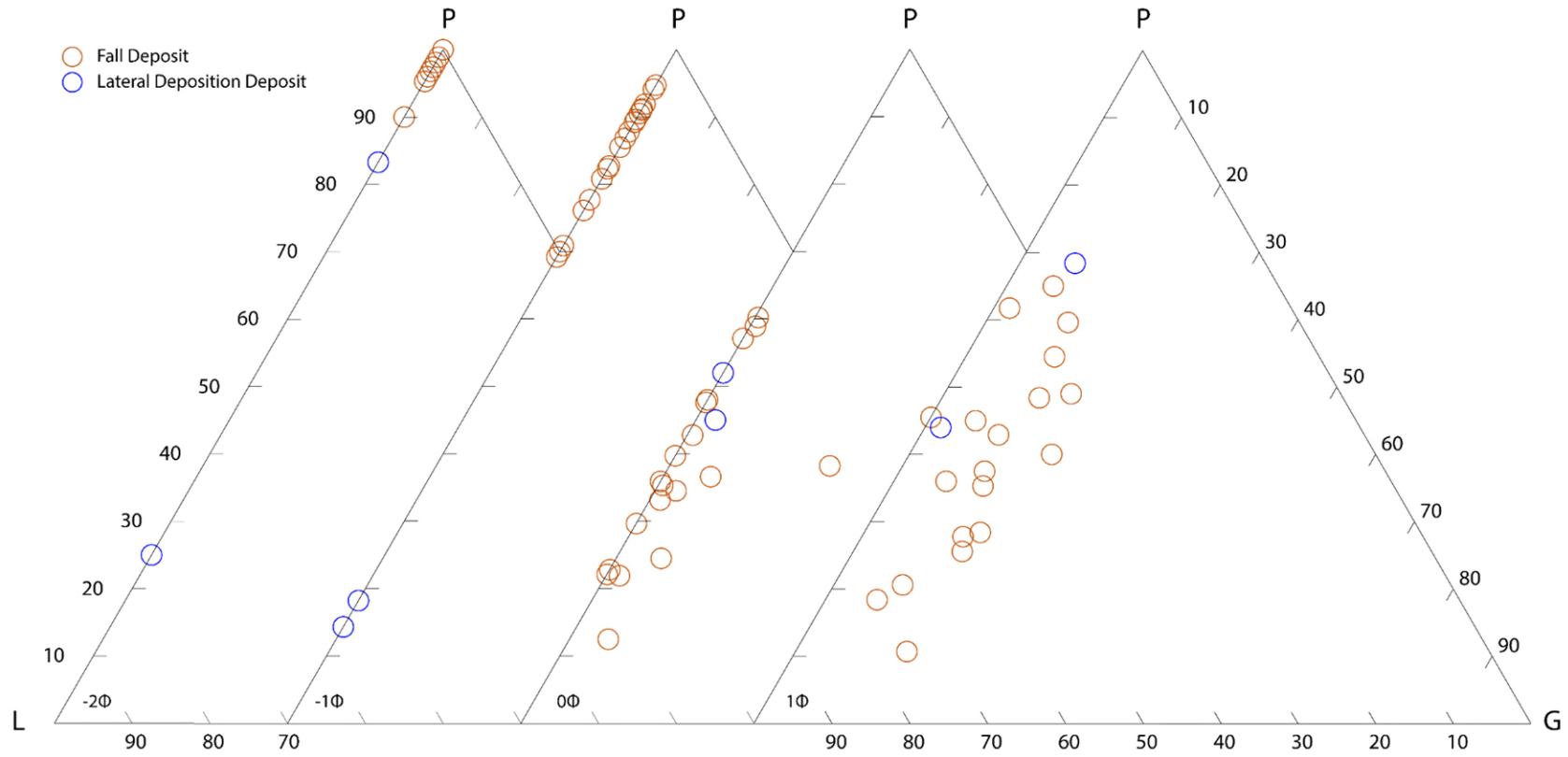

Figure 27 Relative proportion of pumice (P), lithics (L), and glass/crystals (G) as a function of the grain size (-2ϕ to 1ϕ) in the different deposition deposits of Pulse 2. Percentages are based on the number of grains of each component in the sample.

Table 11 Componentry ratios for Pulse 3 based on grain size -2ϕ to 1ϕ in one phi intervals. The abbreviations 'P', 'L', and 'C/G' means Pumice, Lithic, and Crystals and/or Glass, respectively. The results listed are in percent by number.

Sample ID	Inferred Vent Distance (km)	-2 Phi			-1 Phi			0 Phi			+1 Phi			Total		
		P	L	C/G	P	L	C/G	P	L	C/G	P	L	C/G	P	L	C/G
062419-09C*	3.5	83.3	16.7	0.0	95.2	4.8	0.0	99.4	0.6	0.0	92.9	5.5	1.6	94.3	4.5	1.2
071818-01C*	3.9	100.0	0.0	0.0	78.4	21.6	0.0	82.2	17.8	0.0	73.3	24.0	2.7	76.1	22.1	1.8
062419-08C*	3.9	0.0	0.0	0.0	100.0	0.0	0.0	84.8	13.9	1.3	88.5	10.4	1.1	88.1	10.8	1.1
062519-01C*	4.0	0.0	0.0	0.0	71.4	28.6	0.0	97.1	2.9	0.0	76.4	2.7	20.9	78.9	3.5	17.6
062419-02C*	4.1	66.7	33.3	0.0	100.0	0.0	0.0	96.4	3.6	0.0	93.1	6.9	0.0	93.9	6.2	0.0
062419-03C*	4.1	84.6	15.4	0.0	86.5	13.5	0.0	86.0	14.0	0.0	70.2	29.2	0.6	75.6	24.0	0.4
071818-02C*	4.1	60.0	40.0	0.0	89.2	10.8	0.0	94.7	5.3	0.0	81.6	16.3	2.0	85.1	13.5	1.4
062419-01C*	4.1	100.0	0.0	0.0	78.6	21.4	0.0	61.3	38.8	0.0	66.0	32.4	1.5	65.6	33.2	1.2
062419-07C*	4.1	100.0	0.0	0.0	93.3	6.7	0.0	68.8	30.7	0.6	36.8	57.7	5.5	48.5	47.6	3.9
071818-04C*	4.1	88.9	11.1	0.0	78.0	22.0	0.0	75.7	24.3	0.0	62.3	34.4	3.3	67.5	30.4	2.1
062419-06C*	4.1	100.0	0.0	0.0	94.4	5.6	0.0	89.2	10.8	0.0	64.6	34.2	1.3	73.3	25.9	0.8
062419-05C*	4.2	100.0	0.0	0.0	93.1	6.9	0.0	87.1	12.4	0.5	65.6	33.9	0.5	72.9	26.7	0.4
062419-04C*	4.2	100.0	0.0	0.0	96.4	3.6	0.0	96.3	3.7	0.0	97.2	2.8	0.0	97.0	3.0	0.0
071818-03C*	4.2	58.3	41.7	0.0	74.2	25.8	0.0	76.9	23.1	0.0	63.4	25.4	11.3	68.3	25.0	6.7
071718-01C	5.0	100.0	0.0	0.0	95.1	4.9	0.0	53.2	46.8	0.0	24.4	62.2	13.3	58.3	37.0	4.8
071718-02C	5.1	100.0	0.0	0.0	55.6	44.4	0.0	39.1	60.0	0.9	42.0	54.5	3.5	41.4	55.9	2.7
062319-02C	5.1	100.0	0.0	0.0	85.2	14.8	0.0	68.3	31.7	0.0	63.4	34.3	2.3	65.3	33.1	1.6

*Samples collected from Akrotiri Quarry.

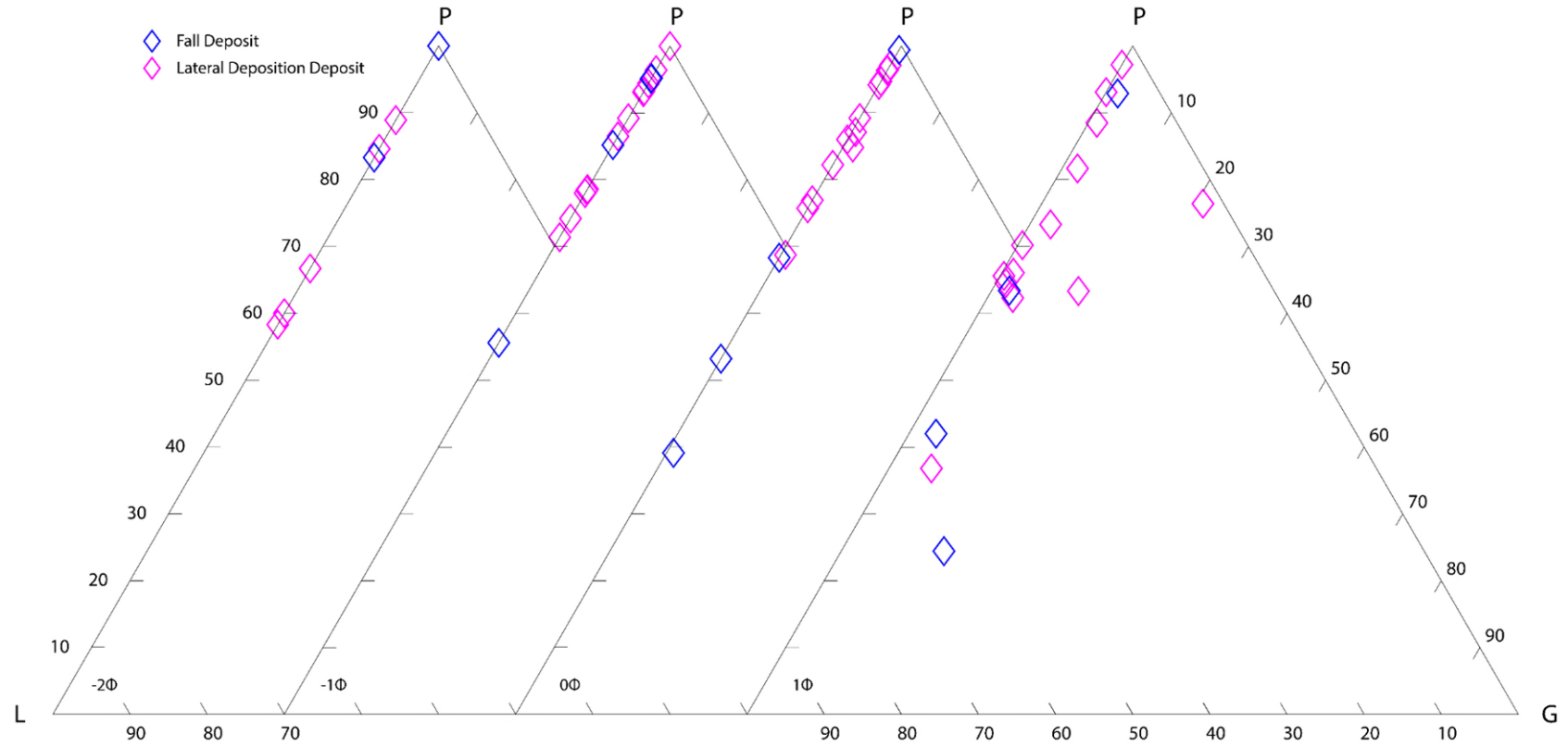

Figure 27 Relative proportion of pumice (P), lithics (L), and glass/crystals (G) as a function of the grain size (-2ϕ to 1ϕ) in the different deposition deposits of Pulse 3. Percentages are based on the number of grains of each component in the sample.

Table 12 Componentry ratios for Pulse 4 based on grain size -2ϕ to 1ϕ in one phi intervals. The abbreviations 'P', 'L', and 'C/G' means Pumice, Lithic, and Crystals and/or Glass, respectively. The results listed are in percent by number.

Sample ID	Inferred Vent Distance (km)	-2 Phi			-1 Phi			0 Phi			+1 Phi			Total		
		P	L	C/G	P	L	C/G	P	L	C/G	P	L	C/G	P	L	C/G
071818-01D	4.9	40.0	60.0	0.0	83.7	16.3	0.0	63.2	36.8	0.0	31.0	55.2	13.8	67.7	22.7	9.6
062419-08D	4.9	66.7	33.3	0.0	89.3	10.7	0.0	61.0	39.0	0.0	46.9	49.7	3.4	51.9	45.7	2.4
062419-02D	5.1	0.0	100.0	0.0	69.6	30.4	0.0	57.5	42.5	0.0	53.5	39.5	7.0	55.7	40.6	3.7
062419-03D	5.2	100.0	0.0	0.0	77.4	22.6	0.0	82.9	17.1	0.0	51.8	41.8	6.4	62.5	33.3	4.1
071818-02D	5.2	66.7	33.3	0.0	62.3	37.7	0.0	59.5	37.8	2.7	31.5	53.7	14.8	63.6	22.2	14.3
062419-07D	5.2	66.7	33.3	0.0	68.4	31.6	0.0	47.7	52.3	0.0	35.5	60.5	3.9	40.4	57.0	2.6
062419-06D	5.2	0.0	100.0	0.0	65.6	34.4	0.0	62.0	38.0	0.0	48.8	43.6	7.6	52.0	42.2	5.8
072018-04D	5.2	100.0	0.0	0.0	40.8	59.2	0.0	51.4	25.7	22.9	47.2	43.4	9.4	66.2	17.3	16.5
071718-04D	5.2	85.7	14.3	0.0	54.5	45.5	0.0	21.6	72.5	5.9	17.0	54.7	28.3	34.0	44.4	21.6
062419-05D	5.3	66.7	33.3	0.0	81.6	18.4	0.0	66.5	33.5	0.0	56.7	37.5	5.8	60.9	35.4	3.8
062419-04D	5.3	100.0	0.0	0.0	84.0	16.0	0.0	73.4	26.6	0.0	41.6	43.4	15.0	52.3	37.5	10.1
071818-03D	5.3	28.6	71.4	0.0	66.0	34.0	0.0	59.7	40.3	0.0	37.7	49.2	13.7	65.4	25.6	9.0
062419-01D	5.3	66.7	33.3	0.0	47.2	52.8	0.0	42.6	56.1	1.4	44.1	48.5	7.4	43.8	52.2	4.0
071418-03D	5.3	90.4	9.6	0.0	37.6	62.4	0.0	11.1	88.9	0.0	25.7	68.6	5.7	37.9	59.9	2.2
071418-04D	5.3	88.9	11.1	0.0	44.2	55.8	0.0	25.3	71.3	3.4	18.1	76.6	5.3	41.4	52.6	6.0
062219-01D	5.4	33.3	66.7	0.0	43.1	56.9	0.0	15.6	84.4	0.0	25.0	75.0	0.0	22.8	77.2	0.0
062219-03D	5.4	100.0	0.0	0.0	24.2	75.8	0.0	16.2	83.8	0.0	55.1	36.7	8.2	31.6	65.4	3.0
061819-01D	6.1	50.0	50.0	0.0	55.5	44.5	0.0	26.3	73.7	0.0	32.8	67.2	0.0	36.4	63.6	0.0
071718-01D	6.6	75.0	25.0	0.0	45.8	54.2	0.0	18.2	81.8	0.0	26.1	72.5	1.4	46.3	52.4	1.3
071718-02D	6.6	66.7	33.3	0.0	43.7	56.3	0.0	38.2	61.8	0.0	51.1	44.7	4.3	59.5	37.7	2.8
071718-03D	6.6	100.0	0.0	0.0	51.6	48.4	0.0	36.0	64.0	0.0	31.3	68.8	0.0	55.9	44.1	0.0
062319-01D	6.6	100.0	0.0	0.0	55.0	45.0	0.0	24.7	75.3	0.0	42.7	52.0	5.3	35.0	62.0	2.5
062319-02D	6.6	100.0	0.0	0.0	50.4	49.6	0.0	30.8	69.2	0.0	50.0	43.9	6.1	39.9	57.8	2.3
072018-05D	6.8	81.8	18.2	0.0	43.0	57.0	0.0	39.1	60.9	0.0	27.8	61.9	10.3	51.8	39.0	9.2
062319-05D	6.9	100.0	0.0	0.0	61.1	38.9	0.0	31.3	68.7	0.0	61.9	37.2	0.9	50.5	49.0	0.5
072018-03D	7.4	100.0	0.0	0.0	28.1	71.9	0.0	23.3	76.7	0.0	42.9	53.1	4.1	55.8	40.1	4.1

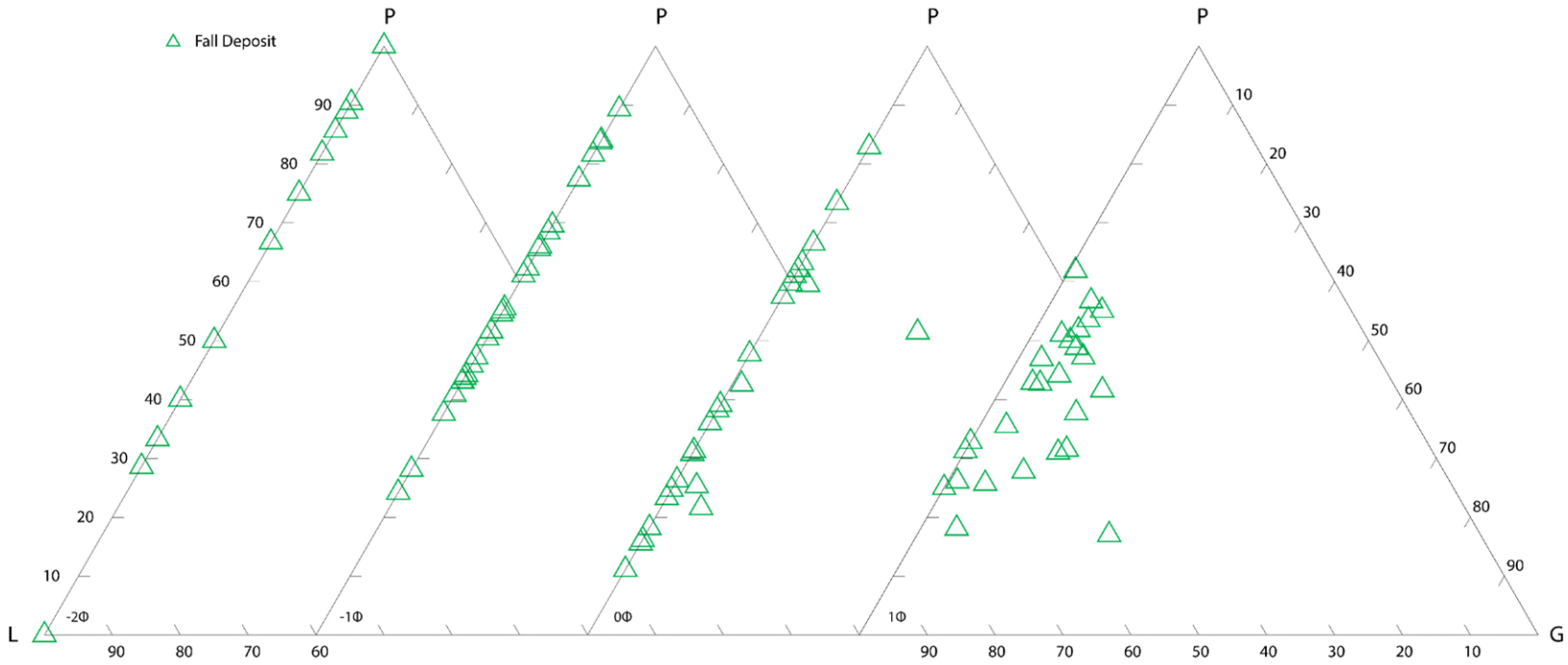

Figure 28 Relative proportion of pumice (P), lithics (L), and glass/crystals (G) as a function of the grain size (-2ϕ to 1ϕ) in the deposits of Pulse 4. Percentages are based on the number of grains of each component in the sample.

5.0 Discussion

5.1 Eruption Dynamics

The precursory deposit has been divided into four layers representing four eruptive pulses, which can be individually sampled and measured only in the medial-distal locations. In proximal regions, these layers could not be measured or sampled as these deposits were destroyed or buried during the LBA eruption. Size grading is most commonly interpreted in terms of steadiness of the eruption column dynamics but can also be influenced by wind shifts and inclination of the column or jet (Houghton and Carey 2015). Mapping deposits, visual observations, grain-size, and componentry of deposits aid in the identification of the eruption style for the deposits.

Volcanic plumes are produced by a variety of explosive eruptions ranging from Hawaiian and subplinian and Plinian to phreatoplinian eruptions. Plumes form from jets of gas and pyroclasts, in this case lithics and pumice, as they entrain and heat air and atmospheric moisture and continue to rise buoyantly. During Hawaiian and Strombolian style eruptions, the rapid expansion of gas fragments ejects adjacent molten magma clots and ash, plus minor amounts of lithics (Taddeucci et al. 2015). The deposits from Hawaiian and Strombolian eruptions are relatively coarse grained, well sorted, and locally dispersed (Taddeucci et al. 2015) ruling Hawaiian and Strombolian style eruptions out for the four pulses of the precursory eruption.

Three types of pyroclastic fall deposits can be distinguished on broad lithological grounds: (1) scoria- fall deposits; (2) pumice-fall deposits; and (3) ash-fall deposits (Cas and Wright 1987). The four precursory deposits have been identified as pumice ash-fall deposits. Pumice-fall deposits form widely dispersed sheets and are the sub-plinian, Plinian, and phreatoplinian deposits in Walker's (1973) classification scheme (Cas and Wright 1987). Ash-fall deposits can be formed by a wide range of pyroclastic processes including phreatomagmatic eruptions, vulcanian eruptions, and phreatic eruptions. Minor precursory explosive phreatic or phreatomagmatic eruptions are common prior to a caldera-forming eruption (Branney and Acocella 2015).

5.1.1 Pulse 1

Layer 1, the basal layer in the precursor stratigraphic sequence, is composed of a light brown, ash-rich tephra dominated by lithics with white pumice and minor amounts of crystals/glass. The isopach map, grain size distribution, and pumice/lithic/crystal ratios indicate there are two separate

depositional processes, ashfall and lateral deposition or erosion, that occurred during Pulse 1. Mantle bedding is characteristic for ashfall deposits on plane-parallel beds and follow preexisting relief on slope angles up to 25° to 30° (Houghton and Carey 2015). In most exposures, Pulse 1 showed mantling bedding with little to no variation in thickness. The presence or absence of fine-scale stratification indicates whether the eruption was non-sustained or sustained (Houghton and Carey 2015). No bedding structures or stratification were observed in Pulse 1 which was also a very-short-lived eruption based on the very thin (<1 cm) deposit.

Therefore, mapping and isopach maps, grain size, and lithic/pumice/ratios were crucial in determining the depositional processes of Pulse 1. Pulse 1 deposits were mapped within a narrow elliptical band on the Akrotiri peninsula with a thinning to the southeast (**Figure 13**) and no evidence of erosion in most areas where the precursory deposits were observed. The exception was in the Akrotiri quarry where Pulse 1 was observed in two locations (**Figures 11**, **13**, and **18**). Pulse 1 was observed in the back of the quarry and slightly to the southwest with a measured thickness of 0.5 cm and 1 cm, respectively. Between these two locations, Pulse 1 was not observed as an existing stratigraphic layer indicating a secondary depositional process.

Tephra accumulated on a landscape modified by cultural use including towns and agricultural fields, as is demonstrated by various cultural debris buried beneath this precursor layer now disclosed during archaeological fieldwork. Molds of plant stems, approx. 2-3 cm thick, have been found along with leaf imprints documenting Bronze Age plants that were smothered by the tephra. Outcrops along with the modern southern coast expose this basal precursory layer in fine detail recording mantling structures around large rocks or slump structures off slides of boulders. Such features would have been presumably easily eroded by wind and rain, thus inferring the lack of a hiatus and weather-related erosional events after post-deposition of this layer and overlying layers – it is thus clear that deposition during the initial pulse of the precursory eruption occurred during a brief period without strong winds and rain.

Grain size distribution of samples collected from Pulse 1 also supports the two depositional processes. Most of the samples show unimodal distribution, a depletion of fines, well sorting, and a fining in median grain size with distance from vent indicating ashfall. While grain-size distribution indicates a depletion of fines, most samples are comprised of more than 50% of grains smaller than 1 mm. In general, good sorting is an important criterion for distinguishing ash fallout

from PDCs (Walker 1971). Most fallout tephra deposits have sorting values between 1 and 2, with most around 1.4 (Fisher and Schmincke 1984). Most of Pulse 1 has sorting values ranging between 0.8 and 1.6 (**Table 5**) well within the range of sorting values for most fallout tephra deposits.

Pumice/lithic/crystal ratios (**Figure 26**; **Table 9**) indicate these samples of ashfall origin contain an abundance of lithic fragments (>58%) with the highest lithic content samples being less than 4 km from the inferred vent location. The abundance of lithic clasts is an indicator of the competence and stability of the rocks forming the vent or conduit walls, as well as fluctuations of the pressure in the conduit (Houghton and Carey 2015). Phreatic eruptions also produce lithic ash-fall deposits (Cas and Wright 1987). Phreatic eruptions occur when head and water combine to fragment preexisting volcanic materials and hurl the resulting tephra into the sky (Siebert et al. 2015). Since these well sorted, unimodal, tephra fallout samples contain an abundance of lithic fragments indicates a phreatic eruption.

Grain size distribution of the two samples from Akrotiri quarry show bimodal distribution, a wide range of grain sizes (-2ϕ to 5ϕ), poor sorting, and a wide range between median grain size within a very short distance between the two points (**Table 5**). Pumice/lithic/crystal ratios also vary significantly between these two points with an abundance of pumice in the finer material (**Figure 26**; **Table 9**). Poor sorting ($\sigma_\phi > 2$) generally indicates lateral deposition such as a PDC (Cas and Wright 1987). PDCs are strongly influenced by topography and prefer to channel down valleys and swamping topographic depressions (Brown and Andrews 2015). The lack of Pulse 1 between the inferred vent location and the back of the quarry does not support the deposit being of PDC origin, but rather from erosion where larger pumice clasts abraded into finer pumice and deposited at these two locations.

Distribution and isopachs of layer thickness indicate a layer distributed in a narrow elliptical band to the southeast with a maximum thickness of 1 cm and an estimate volume of 0.20 to 7.7 x 10^{-3} km^3 deposited. Isopachs, grain size distribution, and pumice/lithic/crystal ratios infer: (1) a vent placement to the north-northwest just south of the vent inferred for the succeeding Plinian eruption (Bond and Sparks 1976; Heiken and McCoy 1984; Druitt et al 2019); (2) tephra distribution by atmospheric winds blowing to the south-southeast akin to modern Etesian winds; (3) deposition

during dry and calm atmospheric conditions with no evidence of erosion by either strong winds or rain; and (4) a short-lived phreatic eruption.

5.1.2 Pulse 2

This initial phreatic eruption switched to a slightly more magmatic eruption during the second pulse as indicated by the shift in specifically the pumice and lithic ratios with an increase in pumice and a slight decrease in lithic content. Layer 2 is a white, lapilli-rich tephra with relatively equal proportions of pumice and lithics with minor amounts of crystals/glass. Like Pulse 1, isopachs, grain size distribution, and pumice/lithic/crystal ratios of Pulse 2 indicate there are two separate depositional processes, ashfall and lateral deposition or erosion. In most exposures, Pulse 2 showed mantling bedding with little to no variation in thickness within a single exposure. No bedding structures or stratification were observed in Pulse 2 which was also a short-lived sustained eruption based on the thin (<4.5 cm) deposit and lack of internal structures.

Isopachs, grain size, and lithic/pumice/crystal ratios were critical in determining the depositional processes for Pulse 2. Pulse 2 deposits were mapped within a narrow elliptical band on the Akrotiri peninsula with a thinning to the southeast and within the same regions as Pulse 1 (**Figure 14**) and no evidence of erosion in most areas where the precursory deposits were observed. The exception was in the Akrotiri quarry where Pulse 2 was observed in two locations (**Figures 11**, **14**, and **20**). Like Pulse 1, Pulse 2 was observed in the back of the quarry and the northernmost wall of the quarry at a slightly higher elevation. Pumice from Pulse 2 was observed occasionally as single grains at the base of Pulse 3 within the quarry suggesting Pulse 2 had at one point been at that location but was eroded.

Grain size distribution of samples collected from Pulse 2 also supports the two depositional processes. Most of the samples show unimodal distribution with some minor bimodality in some samples, a depletion of fines, well sorting, and a fining in median grain size with distance from vent indicating ashfall. Sub-plinian to phreatoplinian deposits generally show polynomial grain size distribution (Cioni et al 2015). Most of Pulse 2 has sorting values ranging between 1.2 to 1.8 (**Table 6**) which is well within the range of sorting values for most fallout tephra deposits.

Pumice/lithic/crystal ratios (**Table 10**) indicate these samples of ashfall origin contain a relatively equal proportion of pumice and lithic fragments. Plinian eruptions discharge a mixture of gas and particles including juvenile and lithic material from a vent at high speed (Cioni et al 2015). As

there is still an abundance of lithic fragments in Pulse 2 samples, this indicates the continued unstability of the vent or conduit walls.

Grain size distribution of the two samples from Akrotiri quarry show bimodal and trimodal distribution, a wide range of grain sizes (-3ϕ and 5ϕ), poor sorting, and a wide range between median grain sizes within a short distance between the two points (**Table 6**). Pumice/lithic/crystal ratios also vary significantly between these two points with an abundance of pumice in the finer material (**Figure 27**; **Table 10**). Like Pulse 1, the lack of Pulse 2 between the inferred vent location and the back of the quarry does not support the deposit being of PDC origin, but rather from erosion where larger pumice clasts abraded into finer pumice and deposited at these two locations.

Distribution and isopachs of layer thickness indicate a narrow elliptical band distributed to the southeast, similar to the first pulse, with a maximum thickness of 4.5 cm and an estimated volume of 0.9 to 4.7 x 10^{-4} km^3 was erupted. Isopachs, grain size, and pumice/lithic/crystal ratios infer: (1) a vent placement nearby to the initial vent clearing pulse of the precursory eruptions; (2) tephra distribution by atmospheric winds blowing to the south-southeast; (3) deposited during dry and calm atmospheric conditions with no evidence of erosion by either strong winds or rain; and (4) a subplinian eruption.

5.1.3 Pulse 3

Pulse 3, immediately following pulse 2, is a yellowish brown with some red-brown staining, ash-rich tephra comprised of equal portions of pumice and lithic fragments with trace amounts (< 2%) crystals/glass in the tephra fallout deposit. Isopachs, grain size distribution and pumice/lithic/crystal ratios indicate there are two separate depositional processes occurred during Pulse 3. In all exposures, Pulse 3 showed mantling bedding with little to no variation in thickness within an exposure. No bedding structures or stratification was observed in Pulse 3 which was also a short-lived eruption based on the thin (<4 cm) deposit.

Isopachs, grain size, and lithic/pumice/ratios were critical in determining the depositional processes of Pulse 3. Pulse 3 deposits were mapped south of the modern town of Fira and on the Akrotiri peninsula (**Figure 15**) with no evidence of erosion in area where the precursory deposits were observed. The thickest observations for Pulse 3 was along the caldera rim, south of Fira and north of the Akrotiri peninsula (**Figure 11**, **15**, and **22**). Unlike Pulses 1 and 2, Pulse 3 was observed throughout the quarry with no break in deposition. While directional bedding structures

like crossbedding are a common feature of PDCs, the Pulse 3 deposit is too thin to identify any internal bedding structures. And where the deposit is thickest, the exposure is perpendicular to the inferred travel direction of the PDC based on the inferred vent location from tephra fallout isopachs (**Figure 15**).

Grain size distribution of samples collected from Pulse 3 supports two depositional processes. The samples closest to the archaeological site show unimodal and bimodal distribution, relatively depleted of fines (< 3ϕ), well sorted, and a fining in median grain size with distance from vent which indicates tephra fallout. Phreatomagmatic eruptions form poorly sorted and fine-grained deposits even close to source (Houghton et al 2015). This arises from two key processes: (1) additional fragmentation during magma-water interaction leading to increased ash production, and (2) wet aggregation of ash which rapidly scavenges fine-grained particles out of the atmosphere (Houghton et al. 2015; Cas and Wright 1987; Heiken and Wohletz 1985). The maximum size of experimental phreatomagmatic explosion debris is 2 to 3 mm, non-explosive debris are coarser

Figure 30 Pulse 2 and 3 deposits draping an old agricultural wall. Pulse 2 deposits are incorporated in the base of the Pulse 3 deposits. Picture taken from an exposure within the Akrotiri Quarry.

grained, with the finest debris <1 μm (Heiken and Wohletz 1985). Explosive phreatomagmatic eruption deposits have a median grain size of 1 or 2 mm, which is also the median grain size of many magmatic tephra deposits (Heiken and Wohletz 1985).

Pumice/lithic/crystal ratios (**Table 11**) indicate these samples of ashfall origin contain a relatively equal proportion of pumice and lithic fragments. As there is still an abundance of lithic fragments in Pulse 3 samples, this indicates the continued unstability of the vent or conduit walls.

Grain size distribution of the samples from Akrotiri quarry and to the north show polymodal distribution, a wide range of grain sizes (-3ϕ to 6ϕ), poor sorting, and a wide range between median grain sizes within the quarry (**Table 7**). Pumice/lithic/crystal ratios also vary significantly between these samples with an abundance of pumice (> 65%) in most samples and at all grain sizes (**Figure 28**; **Table 11**). PDCs can carry a wide variety of material including pumice, and lithic clasts, and debris picked up by the current (Brown and Andrews 2015). Particles within a PDC range in size from micron-sized ash particles up to boulder-sized pumice or lithic clasts (Brown and Andrews 2015). Ash particles are commonly angular and/or platy, while pumice and lithic clasts can be more equant in shape (Brown and Andrews 2015). In general, PDCs are poorly to very poorly sorted with sorting values greater than 2 (Cas and Wright 1985; Brown and Andrews 2015). Within the Akrotiri quarry, pumice from Pulse 2 was observed mixed in with the Pulse 3 deposit indicating the PDCs eroded the Pulse 2 deposits and incorporated the deposits within the flow (**Figure 30**).

Molds of plant stems, approx. 2-3 cm thick, have been found along with leaf imprints documenting Bronze Age plants that were smothered by the tephra (**Figure 31**). These molds were observed within the Akrotiri quarry along with small holes, approx. 1-2 cm in diameter.

Distribution and isopachs of layer thickness indicate a narrow elliptical band of tephra fallout distributed to the southeast, similar to the first two pulses, with a maximum thickness of 1 cm and an estimated volume of 3.0 to 3.5 x 10^{-4} km^3 was erupted. Isopachs, grain size, and pumice/lithic/crystal ratios infer: (1) a vent placement nearby to the first two pulses of the precursory eruptions; (2) tephra distribution by atmospheric winds blowing to the south-southeast; (3) deposited during dry and calm atmospheric conditions with no evidence of erosion by either strong winds or rain; and (4) a phreatomagmatic eruption producing PDCs which traveled in an easterly direction.

Figure 31 Imprint of a leaf in the Pulse 3 deposits observed in the Akrotiri quarry.

5.1.4 Pulse 4

After a brief hiatus, pulse 4, the final phase of the precursory eruption, is a light gray, lapilli-rich tephra with equal portions of lithics and pumice and small amounts of crystal fragments. Grain-size distribution of the Pulse 4 deposits indicate a unimodal distribution with many of the samples depleted of fines, especially in the distal region (**Figure 24**; **Table 8**). In distal, ash-dominated regions of the volcanic cloud, aggregation of the airborne fine ash particles (<250 μm) frequently occurs due to electrostatic attraction or wet cohesion explaining the lack of finer material in the distal region (Houghton and Carey 2015). Sorting of the pulse 4 deposit ranges from well sorted to poorly sorted though the deposit is better sorted with distance from vent. Pumice/lithic/crystal ratios vary significantly throughout the deposit (**Figure 29**; **Table 12**), also indicating aggregation of both lithic and pumice fragments.

Distributions and isopachs of layer thickness indicate a narrow elliptical band distributed to the south with a maximum thickness of 2.5 cm and an estimated volume of 0.73 to 5.0 x 10^{-3} km^3 was

erupted. Isopachs, grain-size distribution, and pumice/lithic/crystal ratios infer: (1) a shift in vent placement to the north-northwest closer to the vent inferred for the succeeding Plinian eruption (Bond and Sparks 1976; Heiken and McCoy 1984; Druitt et al 2019); (2) tephra distributed by atmospheric winds blowing to the south-southeast; (3) deposited during dry and calm atmospheric conditions with no evidence of erosion by either strong winds or rain; and (4) a phreatic eruption. The gradational contact from precursory pulse 4 into Bo1 suggest this pulse of the precursory was a preliminary vent opening for the succeeding Plinian eruption which gradually shifted into the more explosive phase.

5.2 Inferred Cultural Response to the Precursory Eruptions

As previously stated in **Section 2.1.1**, Santorini is in a seismically active region with the subduction of the African plate beneath the Aegean plate. Thus, one can infer the Therans were familiar with seismicity which is clear from earthquake and repairs to buildings during various episodes during the Neolithic to LBA (Marthari 1990; Palyvou 1984; Doumas 1978, 1983). This includes a major destructive episode approximately a century before the eruption which caused significant damage to buildings, identified by archaeologists as the Seismic Destruction Level (SDL; Marthari 1990). As minor earthquakes most likely occurred prior to the onset of the precursory eruption, the inferred human response to the uptick in earthquake activity was not alarming, just a nuisance.

All four layers from the precursory eruption have been observed and mapped at the Akrotiri archaeological excavation on the south coast of Thera (Marinatos 1999; McCoy unpublished). The first three layers were found intact in external spaces between buildings. The absence, in some areas, or disruptions to these layers by man or weather events strongly implies abandonment of Akrotiri prior to the precursor eruption, or from other activity such as earthquakes, gases, ground deformation, etc. The occurrence of seismic activity is seen in minor damage to buildings (Marinatos 1999).

Isopachs, grain-size distribution, and pumice/lithic/crystal ratios indicate the first pulse (maximum thickness of 1 cm) was a short-lived phreatic explosion which was most likely alarming to the Therans. They perhaps went indoors to wait out the eruption, maybe even started to gather valuables incase the eruption continued. The first pulse continued into the second pulse (maximum thickness 4.5 cm), which was a minor sub-plinian eruption based on isopachs, grain-size

Figure 32 Beds pulled into a town square during repairs to damaged buildings between the third and fourth pulse of the precursory eruption.

distribution, and pumice/lithic/crystal ratios. This is most likely when the Therans retreated to their boats and began paddling for Crete or other nearby islands. By the time pulse 3 started, it is speculated the inhabitants had fully abandoned the island.

A slight pause in eruptive vent activity is inferred following pulse 3 prior to pulse 4, as occupants apparently returned for repairs such as at Building Gamma at the Akrotiri excavation (Doumas 1983; Marinatos 1999). Sweeping and clearing of precursory layers 1, 2, and 3 along with building debris and rubble were piled into a small plateia outside of Building Gamma, layer 4 deposits draped these piles (Marinatos 1999; McCoy, unpublished). Beds were pulled out in town squares during these clearing and repair efforts (**Figure 32**; Doumas 1983; Marinatos 1999; McCoy, unpublished). There is some evidence of campfires in the plateia near Building Gamma (McCoy, unpublished).

An abrupt and rapid departure of these returned inhabitants prior to, or during the start of pulse 4 seems clear from archaeological observations: beds left outside; partially re-plastered and repaired internal walls; pots filled with plaster in them containing mixing sticks and brushes. Sharp stratigraphic contacts of layer 4 on layer 3 as well as on the swept piles of layers 1-3 substantiates

the rapid renewal of vent activity during this final phase of the precursory eruption. That these inhabitants successfully escaped the island is documented by the lack of victims found buried beneath these precursory and the succeeding Plinian phase deposits.

As precursory pulse 4 grades into Bo_1, it is suggested precursory pulse 4 was an initial phase of Bo1. As no casualties have yet been found along this stratigraphic contact indicates that there was adequate time for those who returned to Akrotiri to escape. Ancient (and modern) Akrotiri is on the water thus getting to boats could have been quick. In the Bronze Age, their only means of escape off the island would have been by boat – the marine fresco/wall-painting found in the West House at the Akrotiri excavation portrays the typical boat of that period, and the propulsion was mainly by rowing and paddling (Doumas 1983).

5.3 Theran Culture Relocation During and After the Main Eruption

As archaeological investigations at Akrotiri and elsewhere on islands in the Thera archipelago have yet to uncover any human remains beneath or within the volcanic tephra from the eruption, it seems clear that there was adequate time for the Therans who returned to Akrotiri to escape (Doumas 1983; Marinatos 1999). Yet, archaeological sites on nearby islands, especially Crete, do not indicate a population influx with Theran crafts at the time of the LBA eruption (Driessen and Macdonald 2000). Thus, the question of where these Therans evacuated to remains.

In the Bronze Age, their only means of escape off the island would have been by boat. Ancient (and modern) Akrotiri was on the water thus getting to boats would be quick. Excavations of the West House at Akrotiri recovered a marine fresco/wall-painting which portrays the typical boat of that period, and indicates propulsion was mainly by rowing and paddling (Doumas 1983). Broodbank (2013) estimates paddling would result in a velocity of 50 to 60 km/day (or 1.7 to 2.1 km/hr), perhaps a bit faster when escaping a volcanic eruption.

As previously mentioned, Bo_1 generated a sustained plume estimated at a height of 36 ± 5 km (Johnston et al 2014) with an estimated accumulation rate of 3 cm/min for a duration of 1-8 hour(s) (Sparks and Wilson 1990). Pumice deposited on the sea around Thera, likely formed enormous rafts of floating pumice which drifted on surface currents throughout the Aegean and eastern Mediterranean Seas. Pumice rafts are common phenomenon which have been observed from explosive submarine eruptions and volcanic island eruptions. A similar phenomenon occurred

during the 1883 Plinian eruption of Krakatau as recorded by eyewitness accounts (Carey et al 1996).

Wilson (1978) estimates the entire main eruption lasted a minimum of 18 hours with the first nine hours assigned to the first two main eruption phases, thus within a few hours the vent dynamics would have changed to highly explosive characteristics and produced PDCs. These flows can traverse the sea surface for long distances which is well documented at historic eruptions as well as from volcanological research of past Plinian-type eruptions (Carey et al. 1996; Dufek et al. 2007; and others) and experimental observations (Freundt 2003). Given the velocity of paddling, at the time of this change in eruption character, the Therans were at most between 13.6 and 16.8 km away from the raging volcano and its rain of pumice and ash of Bo_1 (**Figure 33**).

The most compelling observations from the 1883 eruption of Krakatauu and PDCs traversing the sea surface is the large number of burn fatalities (~2,000 people) along the southeast coast of Sumatra in the district of Katimbang, ~40 km from the Krakatau caldera and separated by the waters of the Sunda Straits (Carey et al. 2000). Additional evidence of PDCs travelling over the sea surface can be found in the logs of several ships that were in the Sunda Straits region during the time of the eruption (Carey et al. 1996, 2000). The *Loudon* was en route to Telok Betong on the coast of Sumatra from Anjer. The *Charles Bal* was in passage through the Sunda Straits from the southeast to northwest during the eruption.

On the afternoon of August 26, 1883, the main eruption began when a Plinian eruption column rose to an elevation of at least 25 km with the generation of localized PDCs (Sigurdsson et al. 1991; Carey et al. 1996). At some point in the early morning of August 27, the eruption dynamics shifted from a convecting eruption column to a dominantly collapsed column with the production of large-volume PDCs (Self 1992; Carey et al. 1996). Significant evidence, from eyewitness accounts to the geological record, exists for the occurrence of one or more widespread pyroclastic flows traveled over the sea surface during the climatic phase of the Krakatau eruption on the morning of August 27. Deposits on the islands of Sebesi, Sebuku, Lagoendi, and the coast of Sumatra were laid down by PDCs that traveled over the sea surface for at least 40 km and perhaps as much as 80 km (Carey et al 1996, 2000).

During the eruption, a major event occurred at about 10 a.m. on August 27 when the largest explosion was generated at the volcano. While the exact timing of the event is uncertain, Carey et

al. (1996) assumed the event took place at 10 a.m. in order to calculate the travelling velocity of the PDCs. It has been suggested this major event corresponds with the time of peak eruption intensity and the start of the caldera collapse (Sigurdsson et al. 1991; Self 1992; Carey et al. 1996).

The velocity of the flow can be estimated from ship reports and its ability to surmount topographic barriers. Carey et al. (1996) assumed the main flow was generated at the time of the largest explosion (10 a.m. on August 27), then the difference between the explosion and the arrival of hurricane force winds at the ships provides an estimate of the flow velocity. The *Loudon*, located 65 km from Krakatau, noted hurricane force winds at 10:30, thus yielding a velocity of 260 km/hr (or 4.3 km/min) (Carey et al. 1996). Meanwhile, the *Charles Bal*, also located 65 km from Krakatau, recorded the large explosion occurring at 10:15 a.m. with hurricane force winds at 10:30 a.m., yielding a similar velocity of 260 km/hr (Carey et al. 1996). Thus, the discrepancy in the timing of the explosion results in a factor of two uncertainty for the velocity. If the gas-works record is used for the explosion, the velocity of the flow would be 130 km/hr (or 2.2 km/min) (Carey et al. 1996). Another method Carey et al. (1996) used for velocity estimation is to use the dynamics of the flow as inferred by the surmounting of topographic barriers. Field observations of Sebesi island show the flow passed over the highest peak at an elevation of 800 m of the island (Carey et al. 1996). Thus, Carey et al. (1996) used the relationship:

$$v^2 = gh \tag{6}$$

where v is velocity, g is the gravitational acceleration, and h is the height of the obstacle, to calculate a velocity of 320 km/hr (or 5.3 km/min).

Assuming a duration of 8 hours for Bo_1, paddling velocity of 1.7 to 2.1 km/hr, and pristine paddling conditions that is no retardation from thick pumice rafts, the Therans had paddled a distance between 13.6 and 16.8 km (**Figure 33**) before the change to a highly explosive characteristic that produced PDCs. Using the Carey et al. (1996) calculation of the 1883 PDCs of Krakatau and assuming a constant travelling velocity across the sea surface, one can calculate the time it took for the PDCs to reach the Therans in their boats (**Figure 34**): perhaps incinerated at sea within 3 to 8 minutes explaining the lack of evidence of Theran craft and a population influx at archaeological sites throughout the southern Aegean Sea, specifically Crete.

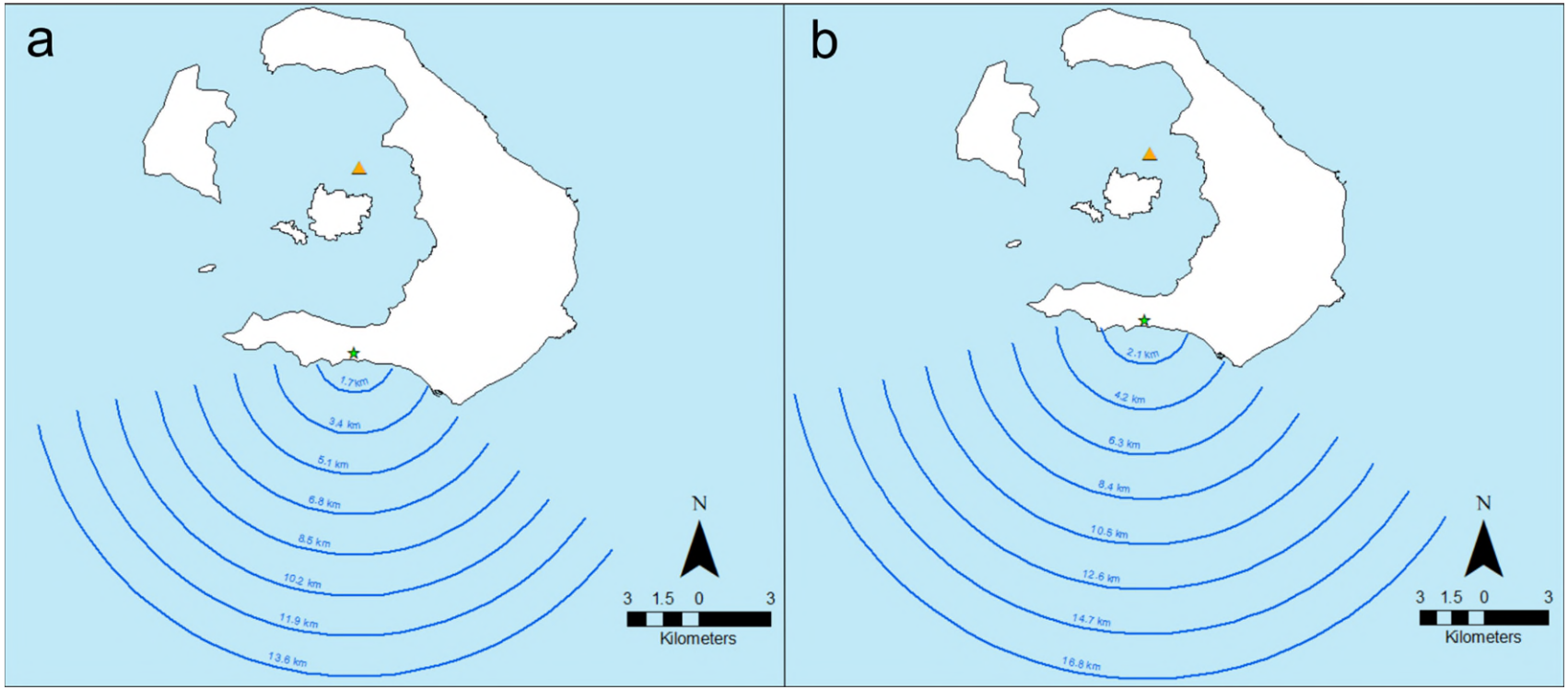

Figure 33 Distance Therans paddled from Santorini. (a) Paddling at 1.7 km/hr, the Therans were 13.8 km and (b) at 2.1 km/hr, the Therans were 16.8 km from the island before the Plinian eruption changed eruption dynamics containing pyroclastic density currents. The blue lines represent the approximate location of the Therans after each hour of paddling.

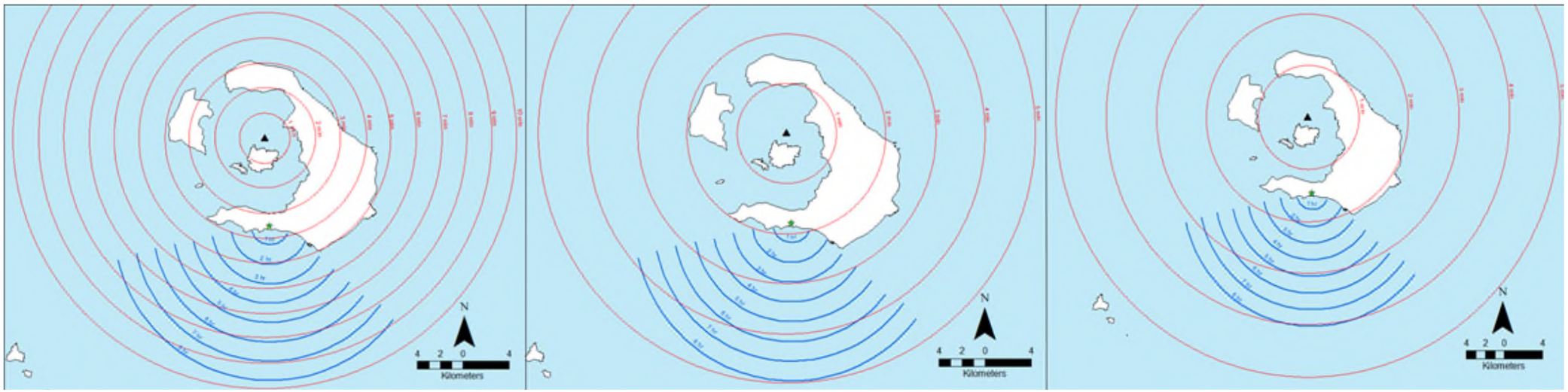

Figure 32 Paddling at a rate of 1.7 km/hr, the Therans are approximately 13.6 km from the island. Pyroclastic density currents (PDCs) traveling at a velocity of (a) 130 km/hr reaches the Therans in 9 to 10 minutes; (b) 260 km/hr reaches the Therans in 5 minutes; and (c) 320 km/hr reaches the Therans in 4 minutes. The blue lines represent the approximate location of the Therans after each hour of paddling. The red lines represent the approximate location of the PDCs after each minute of travel.

6.0 In Summary

Precursory phenomenon frequently provides advance warning of pending volcanic eruptions via tectonic or landscape disruptions, effusive activity, seismicity and changes in existing geothermal systems. Precursory phenomena preceding one of the largest eruptions in the last 10,000 years on a global bases (VEI 7; Johnston et al 2014) – and certainly in the Aegean was identified by Heiken and McCoy (1990). This thesis revisited the eruption dynamics of this phase including re-mapping of the deposits, and collection and laboratory analysis of samples, and also inferred the cultural response to this precursory phenomenon and the relocation of the Theran culture during and after the eruption.

In summary, the precursory eruptive activity consists of four distinct pulses. These layers are in sharp stratigraphic contact with the underlying paleosol and internally indicate a minimal "time gap" between each pulse except between pulses 3 and 4. As seen from archaeological evidence, A brief hiatus long enough for the Therans to return to the island and start repairs to damaged buildings occurred between pulse 3 and 4 as seen from archaeological evidence. This hiatus is estimated to have lasted between a few days to perhaps a month. Isopachs, grain size, and componentry of the first three pulses and fourth pulse indicates:

1. A vent placement to the north-northeast, just south of the vent inferred for the succeeding Plinian eruption (Bond and Sparks 1976; Heiken and McCoy 1984; Druitt et al 2019);
2. Tephra distribution by atmospheric winds blowing to the south-southeast;
3. Deposition during dry and calm atmospheric conditions with no evidence of erosion by either strong south-southeast winds or rain; and
4. A phreatic eruption shifting to a sub-plinian eruption then shifting to a phreatomagmatic eruption producing PDCs. A brief hiatus occurred after Pulse 3 before Pulse 4 which was a phreatic eruption.

The inference is that (a) this precursory activity was so unusual and intense, the inhabitants were adequately stunned and left; and (b) the precursory activity continued almost abated into the main catastrophic eruption, not allowing wholescale return and reoccupation of the island, though some returned but left again immediately prior, or during the opening phase of the main eruption.

Escape would have been through a sea clogged with floating pumice, an expected consequence of the eruption characteristics and dynamics of Bo_1, thus retarding distances paddled. Estimates are that the entire main eruption took a minimum of 18 hours (Wilson 1978) – with the first nine hours assigned to the first two main eruption phases, thus with a few hours the vent dynamics would have changed to highly explosive characteristics and produced PDC. These flows traverse the sea surface for long distances which is well documented at historic eruptions as well as from volcanological research of past Plinian-type eruptions. Thus, one may assume these escaping Therans were incinerated at sea.

7.0 References

Anadon, P., Canet, C., Friedrich, W.L. (2013). *Aragonite stromatolitic buildups from Santorini (Aegean Sea, Greece): geochemical and paleontological constraints of the caldera paleoenvironment prior the the Minoan eruption (ca 3600 yr BP).* Sedimentology, 60, 1128-1155.

Angelier, J., Lyberis, N., Le Pichon, X., Barrier, E., and Huchon, P. (1982). *The tectonic development of the Hellenic arc and the Sea of Crete: a synthesis*. Tectonophysics, 86, 159-196.

Athanassas, C.D., Bourles, D.L., Braucher, R., Druitt, T. H., Nomikou, P., and Leanni, L. (2016). *Evidence from cosmic ray exposure (CRE) dating for the existence of a pre-Minoan caldera on Santorini, Greece*. Bulletin of Volcanology, 78, 1-13.

Baillie, C.G.L. (1990). *Irish Tree Rings and an Event in 1628 BC*. In: Hardy, D. A. (ed), Thera and the Aegean World III, v. 3, London, The Thera Foundation, 160-166.

Bentacourt, P.P. (1987). *Dating the Aegean Late Bronze Age with radiocarbon*. Archaeometry, 29, 45-49.

Blott, S.J., and Pye, K. (2001). *Gradistat: a grain size distribution and statistics package for the analysis of unconsolidated sediments*. Earth Surface Processes and Landforms, 26, 1237-1248.

Bonadonna, C., and Costa, A. (2012) *Estimating the volume of tephra deposits: a new simple strategy.* Geology, 40, 415-418.

Bonadonna, C., and Houghton, B.F. (2005). *Total grainsize distribution and volume of tephra fall deposits*. Bulletin of Volcanology, 67, 441-456.

Bond, A., and Sparks, R. S. J. (1976). *The Minoan eruption of Santorini, Greece*. Journal of the Geological Society of London, 132, 1-16.

Branney, M., and Acocella, V. (2015). *Calderas*. In: Sigurdsson, H., Houghton, B., McNutt, S., Rymer, H., Stix, J. (Eds), The encyclopedia of volcanoes. Elsevier, 299-315.

Broodbank, C. (2013). *The Making of the Middle Sea: A History of the Mediterranean from the Beginning to the Emergence of the Classical World*. London: Oxford University Press.

Brown, R.J., and Andrews, G.D.M. (2015). *Deposits of pyroclastic density currents*. In: Sigurdsson, H., Houghton, B., McNutt, S., Rymer, H., Stix, J. (Eds), The encyclopedia of volcanoes. Elsevier, 631-648.

Carey, S., Sigurdsson, H., Mandeville, C., and Bronto, S. (1996). *Pyroclastic flows and surges over water: an example from the 1883 Krakatau eruption*. Bulletin of Volcanology, 57, 493-511.

Carey, S., Sigurdsson, H., Mandeville, C., and Bronto, S. (2000). *Volcanic hazards from pyroclastic flow discharge into the sea: Examples from the 1883 eruption of Krakatau, Indonesia*. In: McCoy, F. W., and Heiken, G. (ed), Volcanic Hazards and Disasters in Human Antiquity: Boulder, Colorado, Geological Society of America Special Paper 345.

Cas, R.A.F., and Wright, J.V. (1987). *Volcanic Successions: Modern and Ancient*. London: Allen and Unwin Publishers.

Cherubini, P., Humbel, T., Beeckman, H., Gärtner, H., Mannes, D., Pearson, C., Schoch, W., Tognetti, R., and Lev-Yadun, S. (2013). *Olive tree-ring problematic dating: A comparative analysis on Santorini (Greece).* PLoS One, 8, e54730.

Cherubini, P., Humbel, T., Beeckman, H., Gärtner, H., Mannes, D., Pearson, C., Schoch, W., Tognetti, R., and Lev-Yadun, S. (2014). *The olive-branch dating of the Santorini eruption*. Antiquity, 88, 267-291.

Cioni, R., Pistolesi, M., and Rosi, M. (2015). *Plinian and Subplinian eruptions.* In: Sigurdsson, H., Houghton, B., McNutt, S., Rymer, H., Stix, J. (Eds), The encyclopedia of volcanoes. Elsevier, 519-536.

Dimitriadis, I., Karagianni, E., Panagiotopoulos, D., Papzachos, C., Hatzidimitrious, P., Bohnhoff, M., Rische, M., Meier, T. (2009). *Seismicity and active tectonics at Coloumbo Reef (Aegean Sea, Greece): Monitoring an active volcano at Santorini Volcanic Center using a temporary seismic network.* Tectonophysics, 465, 136-149.

Doumas, C. (1978). *The stratigraphy of Akrotiri.* In: Doumas, C. (ed), Thera and the Aegean World I. London: Thera and the Aegean World, 777-782.

Doumas, C. (1983a). *The excavations at Thera and the Aegean Late Bronze Age*. Endeavour, 7, 144-149.

Doumas, C. (1983b). *Thera: Pompeii of the Ancient Aegean*. London: Thames and Hudson.

Doumas, C. (2010). *Akrotiri*. In: E.H. Cline (ed.), The Oxford handbook of the Bronze Age Aegean (ca. 3000-1000BC), Oxford, Oxford University Press, 752-761.

Downey, W.S., and Tarling, D.H. (1984). *Archaeomagnetic dating of Santorini volcanic eruptions and fired destruction levels of late Minoan civilization.* Nature, 309, 519-523.

Driessen, J., and Macdonald, C.F. (1997). *The Troubled Island: Minoan Crete Before and After the Santorini Eruption* (Aegaeum 17). Liège: Université de Liège.

Driessen, J., and Macdonald, C.F. (2000). *The eruption of the Santorini volcano and its effects on Minoan Crete*. In: McGuire, W.G., Griffiths, D.R., Hancock, P.L. and Steward, I.S. (ed.) The Archaeology of Geological Catastrophes, Geological Society, London, 171, 81-93.

Druitt, T.H. (1985). *Vent evolution and lag breccia formation during the Cape Riva eruption of Santorini, Greece*. Journal of Geology, 93, 439-454.

Druitt, T. H. (2014). *New insights into the initiation and venting of the Bronze-Age eruption of Santorini (Greece), from component analysis*. Bulletin of Volcanology, 76, 1-21.

Druitt, T. H., and Francaviglia, V. (1990). *An ancient caldera cliff line at Phira, and its significance for the topography and geology of Pre-Minoan Santorini*. In: Hardy, D. A. (ed), Thera and the Aegean World III, v. 2: Earth Sciences, London, The Thera Foundation, 362-370.

Druitt, T. H., and Francaviglia, V. (1992) *Caldera formation on Santorini and the physiography of the islands in the late Bronze Age*. Bulletic of Volcanology, 54, 484-493.

Druitt, T. H., McCoy, F.W., Vougioukalakis, E. (2019). *The Late Bronze Age eruption of Santorini volcano and its impact on the ancient Mediterranean world*. Elements, 15, 185-190.

Druitt, T. H., Mellors, R. A., Pyle, D. M., and Sparks, R. S. J. (1989). *Explosive volcanism on Santorini, Greece*. Geological Magazine, 126, 95-126.

Druitt, T. H., Mellors, R. A., Pyle, D. M., and Sparks, R. S. J., Lanphere, M., Davies, M., and Barriero, B. (1999). *Santorini Volcano*. Geological Society of London Memoir 19.

Dufek, J., and Bergantz, G.W. (2007). *Dynamics and deposits generated by the Kos Plateau Tuff eruption: Controls of basal particle loss on pyroclastic flow transport.* Geochemistry Geophysics Geosystems, 8, Q12007.

Eriksen, U., Friedrich, W. L., Buchardt, B., Tauber, H., and Thomsen, M.S. (1990) *The Stronghyle Caldera: Geological, palaeontological and stable isotope evidence from radiocarbon dated stromatolites from Santorini*. In: Hardy, D. A. (ed), Thera and the Aegean World III, v. 2: Earth Sciences, London, The Thera Foundation, 139-150.

Evans, A.J. (1928). *The Palace of Minos.* Volume 2. London: Macmillan.

Fabbro, G.N., Druitt., T.H., and Scaillet, S. (2013) *Evolution of the crustal magma plumbing system during the build-up to the 22-ka caldera-forming eruption of Santorini (Greece).* Bulletin of Volcanology, 75, 767.

Fisher, R.V., and Schmincke, H.U. (1984) *Pyroclastic Rocks*. Springer-Verlag, Berlin, Germany.

Folk, R.L., and Ward, W.C. (1957). *Brazos river bar: a study of the significance of grainsize parameters*. Journal of Sedimentary Petrology, 27, 3-26.

Freundt, A. (2003). *Entrance of hot pyroclastic flows into the sea: Experimental observation.* Bulletin of Volcanology, 65, 144-164.

Friedrich, W. L. (2009). *Santorini: Volcano, Natural History, Mythology*. Denmark: Aarhus University Press, 85-90.

Friedrich, W. L., Wagner, P., and Tauber, H. (1990). *Radiocarbon dated plant remains from the Akrotiri Excavation on Santorini, Greece*. In: Hardy, D. A. (ed), Thera and the Aegean World III, v. 3, London, The Thera Foundation, 188-196.

Friedrich, W. L., and Heinemeier, J. (2009). *The Minoan eruption of Santorini radiocarbon dated to 1613±13 BC – geological and stratigraphic considerations.* In: D.A. Warburton (ed.) Time's up! Dating the Minoan eruption of Santorini: Acts of the Minoan Eruption Chronology Workshop, Sandbjerg, November 2007, Athens: Danish Institute at Athens, 56-63.

Friedrich, W. L., Kromer, B., Friedrich, M., Heinemeier, J., Pfeiffer, T., and Talamo, S. (2006). *Santorini Eruption Radiocarbon Dated to 1627-1600 B.C.* Science, 312, 548.

Friedrich, W.L., Kromer, B., Friedrich, M., Heinemeier, J., Pfeiffer, T., and Talamo, S. (2009). *Santorini eruption radiocarbon dated to 1627-1600 BC: further discussion.* In: S.W. Manning and M.J. Bruce (ed.) Tree-rings, kings, and Old World archaeology and environment: papers presented in honor of Peter Ian Kuniholm, Oxford and Oakville (CT): Oxbow, 293-298.

Fytikas, M., Innocenti, F., Manetti, P., Mazzuoli, R., Peccerillo, A. And Villari, L. (1984). *Tertiary to Quarternary evolution of volcanism in the Aegean region*. In: Dixon, J. E. And Robertson, A. H. F. (eds.) The Geological Evolution of the Eastern Mediterranean. Geological Society, London, Special Publications, 17, 687-699.

Hammer, C. U., Clausen, H. B., Friedrich, W. L., and Tauber, H. (1987). *The Minoan eruption of Santorini in Greece dated to 1645 BC?* Nature, 328, 517-519.

Heiken, G.H., and McCoy, F. W. (1984). *Caldera development during the Minoan eruption, Thera, Cyclades, Greece*. Journal of Geophysical Research, 89, 8441-8462.

Heiken, G.H., and McCoy, F. W. (1990). *Precursory activity to the Minoan eruption, Thera, Greece*. In: Hardy, D.A. (eds) Thera and the Aegean World III, v2: Earth Sciences, London, The Thera Foundation, 79-88.

Heiken, G.H., and Wohletz, K. (1985). *Volcanic Ash*. University of California Press, Los Angeles, California.

Higgins, M.D., and Higgins, R. (1996). *A geological companion to Greece and the Aegean*. Cornell University Press, Ithica, New York, 187-199.

Hölfmayer, F. (2012). *The date of the Minoan Santorini eruption: quantifying the "offset"*. Radiocarbon, 54, 435-448.

Houghton, B., and Carey, R.J. (2015). *Pyroclastic fall deposits.* In: Sigurdsson, H., Houghton, B., McNutt, S., Rymer, H., Stix, J. (Eds), The encyclopedia of volcanoes. Elsevier, 599-618.

Houghton, B., White, J.D.L., and Van Eaton, A.R. (2015). *Phreatomagmatic and related eruption styles.* In: Sigurdsson, H., Houghton, B., McNutt, S., Rymer, H., Stix, J. (Eds), The encyclopedia of volcanoes. Elsevier, 537-552.

Jackson, J. A. (1994) *Active tectonics of the Aegean region.* Annual Review of Earth and Planetary Sciences, 22, 239-271.

Jenkins, S.F., Barsotti, S., Hincks, T.K., Neri, A., Phillips, J.C., Sparks, R.S.J., Sheldrake, T., and Vougioukalakis, G. (2015). *Rapid emergency assessment of ash and gas hazard for future eruptions at Santorini Volcano, Greece.* Journal of Applied Volcanology, 4, 1-22.

Johnston, E.N., Sparks, R.S.J., Phillips, J.C., and Carey, S. (2014). *Revised estimates for the volume of the Late Bronze Age Minoan eruption, Santorini, Greece.* Journal of Geological Society, 171, 583-590.

Jussert, S., and Sintubin, M. (2017). *Minoan Earthquakes Breaking the Myth through Interdisciplinarity*. Leuven University Press, Leuven, Belgium.

Karatson, D., Gertisser, R., Telbisz, T., Vereb, V., Quidelleur, X, Druitt, T., Nomikou, P., and Kosik, S. (2018). *Towards reconstruction of the lost Late Bronze Age intra-caldera island of Santorini, Greece.* Scientific Report, 8, 7026.

Keller, J., Rehren, TH., and Stadlbauer, E. (1990). *Explosive volcanism in the Hellenic Arc: a summary and review.* In: Hardy, D.A. (eds) Thera and the Aegean World III, v2: Earth Sciences, London, The Thera Foundation, 13-26.

Klawonn, M., Houghton, B.F., Swanson, D.A., Fagents, S.A., Wessel, P., and Wolfe, C.J. (2014). *From field data to volumes: constraining uncertainties in pyroclastic eruption parameters.* Bulletin of Volcanology, 76, 839-855.

Klontza-Jaklova, V. (2016). *What's wrong? Hard science and humanities – tackling the question of the absolute chronology of the Santorini eruption.* Maxarykova Univerzita.

Knappett, C., Evans, T., and Rivers, R. (2008). *Modelling maritime interaction in the Aegean Bronze Age.* Anitquity, 82, 1009-1024.

Knappet, C., Rivers, R., and Evans, T. (2011). *The Theran eruption and Minoan partial collapse: new interpretations gained from modelling the maritime network.* Antiquity, 85, 1008-1023.

Kuniholm, P.I. (1990). *Overview and assessment of the evidence for the date of the eruption of Thera*. In: Hardy, D. A. (ed), Thera and the Aegean World III, v. 3, London, The Thera Foundation, 13-18.

Kuniholm, P. I., Kromer, B., Manning, S. W., Newton, M., Latini, C. E., and Bruce, M. J. (1996). *Anatolian tree rings and the absolute chronology of the eastern Mediterranean.* Nature, 381, 780-783.

LaMarche, V. C. Jr., and Hirschboeck, K. K. (1984) *Frost rings in trees as records of major volcanic eruptions*. Nature, 307, 121-126.

Manning, S.W. (1988). *The Bronze Age eruption of Thera: absolute dating, Aegean chronology and Mediterranean cultural interrelations*. Journal of Mediterranean Archaeology, 1, 17-82.

Manning, S.W. (1990). *The eruption of Thera: Date and implications*. In: Hardy, D. A. (ed), Thera and the Aegean World III, v. 3, London, The Thera Foundation, 29-40.

Manning, S.W. (1999). *A test of time: the volcano of Thera and the chronology and history of the Aegean and East Mediterranean in the mid second millennium BC.* Oxford: Oxbow.

Manning, S.W. (2007). *Clarifying the 'high' v. 'low' Aegean/Cypriot chronology for the mid second millennium BC: assessing the evidence, interpretive frameworks, and current state of the debate*. In: Bietak, M and Czerny, E. (ed.) The Synchronisation of civilisations in the Eastern Mediterranean in the Second Millennium B.C. III. Vienna: Verlag der Österreichischen Akademie der Wissenschaften, 101-137.

Manning, S.W. (2009). *Beyond the Santorini eruption: some notes on dating the Late Minoan IB period on Crete, and implications for Cretan-Egyptian relations in the 15th century BC (and especially LM II).* In: Warburton, D.A. (ed.) Time's up! Dating the Minoan eruption of Santorini: Acts of the Minoan Eruption Chronology Workshop, Sandbjerg, November 2007, Athens: Danish Institute at Athens, 207-226.

Marinatos, S. (1999). *Excavations at Thera I-VII*. Athens: The Archaeological Society at Athens.

Marthari, M. (1990). *The chronology of the last phases of Akrotiri in light of the evidence from the West House pottery groups*. In Hardy, D.A. (eds) Thera and the Aegean World III, v.3: Chronology, London, The Thera Foundation, 57-69.

McClelland, C., and Thomas, R. (1990). *A paleomagnetic study of Minoan Age tephra from Thera*. In: Hardy, D.A. (eds) Thera and the Aegean World III, v2: Earth Sciences, London, The Thera Foundation, 129-138.

McCoy, F.W. and Heiken, G. (2000). *The Late-Bronze Age explosive eruption of Thera (Santorini), Greece: Regional and local effects*. In: McCoy, F.W., and Heiken, G. (eds) Volcanic Hazards and Disasters in Human Antiquity: Boulder, Colorado, Geological Society of America Special Paper 345.

McKenzie, D. P. (1970). *Plate tectonics of the Mediterranean region*. Nature, 226, 239-243.

Mercier, J. L., Sorel, D., and Vergely, P. (1989). *Extensional tectonic regimes in the Aegean basins during the Cenozoic*. Basin Research, 2, 49-71.

Newhall, C. G., and Self, S. (1982). *The volcanic explosivity index (VEI): an estimate of explosive magnitude for historical volcanism*. Journal of Geophysical Research, 87, 1231-1238.

Nomikou, P. (2003). *Santorini and Nisyros: similarities and differences between the two calderas of the modern Aegean Volcanic Arc.* CIESM Workshop on "Human records of recent geological evolution in the Mediterranean Basin – historical and archaeological evidence" Santorini 22-25 October 2003, Greece: CIESM Workshop Monographs, 24, 103-108.

Nomikou, P., Druitt, T. H., Hübscher, C., Mather, T. A., Paulatto, M., Kalnins, L. M., Kelfoun, K., Papanikolaou, D., Bejelou, K., Lampridou, D., Pyle, D. M., Carey, S., Watts, A. B., Weiß, B., and Parks, M.M. (2016). *Post-eruptive flooding of Santorini caldera and implications for tsunami generation*. Nature Communications, 7, 1-10.

Paliou, E. (2011). *The communicative potential of Theran murals in Late Bronze Age Akrotiri: applying viewshed analysis in 3D townscapes*. Oxford Journal of Archaeology, 30, 247-272.

Palyvou, C. (1984). *The destruction of the town at Akrotiri, Thera at the beginning of the LC I: rebuilding activities*. In: MacGillivray, J.A., and Barber, R.L.N. (eds) The Prehistoric Cyclades. Edinburgh: Department of Classical Archaeology, 134-147.

Pang, K. D., Keston, R., Srivastava, S. K., and Chou, H.-H. (1989). *Climatic and hydrologic extremes in early Chinese history: possible causes and dates.* (abs.) EOS, 70, 1095.

Paraskevas, M., Paradissis, D., Raptakis, C., Nomikou, P., Hooft, E.E., Papanikolaou, D. (2019). *Geodetic and geophysical approach of the gravitational field in Santorini Volcanic Group*. May 2019, JISDM 2019, DOI: 10. 13140/RG.2.2. 15196.03209

Pearson, C.L., Brewer, P.W., Brown, D., Heaton, T.J., Hodgins, G.W.L., Jull, A.J.T., Lange, T., and Salzer, M.W. (2018). *Annual radiocarbon record indicates 16th century BCE date for the Thera eruption*. Science Advances, 4, eaar8241.

Pearson, C., Salzer, M., Wacker, L., Brewer, P., Sookdeo, A., and Kuniholm, P. (2020). *Securing timelines in the ancient Mediterranean using multiproxy annual tree-ring data*. Proceedings of the National Academy of Sciences, 117, 8410-8415.

Pfeiffer, T. (2001). *Vent development during the Minoan eruption (1640 BC) of Santorini, Greece, as suggest by ballistic blocks*. Journal of Volcanology and Geothermal Research, 106, 229-242.

Pichler, H., and Friedrich, W. L. (1980). *Mecanism of the Minoan eruption of Santorini*. In: Doumas, C. (ed.) Thera and the Aegean World II: London, The Thera Foundation, 15-30.

Pichler, H. and Kussmaul, S. (1980). *Comments on the accompanying geological map and profiles of the Santorini Islands*. In: Doumas, C. (ed), Thera and the Aegean World II: London, The Thera Foundation, 413-427.

Piper, D.J.W., and Perissoratis, C. (2003). *Quaternary neotectonics of the South Aegean arc*. Marine Geology, 198, 259-288.

Pyle, D.M. (1989). *The thickness, volume and grainsize of tephra fall deposits*. Bulletin of Volcanology, 51, 1-15.

Pyle, D.M. (1990). *New estimates for the volume of the Minoan eruption*. In: Hardy, D. A. (ed), Thera and the Aegean world III, v. 2: Earth Sciences: London, The Thera Foundation, 113-121.

Pyle, D.M. (1995). *Assessment of the minimum volume of tephra fall deposits*. Journal of Volcanology and Geothermal Research, 69, 379-382.

Pyle, D.M. (2000). Sizes of volcanic eruptions. In: Sigurdsson, H. (ed.) Encyclopedia of Volcanoes. Academic Press, San Diego, CA, 263-269.

Ramsey, C.B., Manning, S.W., and Galimberti, M. (2004). *Dating the volcanic eruption at Thera*. Radiocarbon, 46, 325-344.

Reck, H. (1936). *Santorini: Der Werdegang eines Inselvulkans und sei ausbruch 1925-1928*. Berlin, D. Reimer.

Schachermeyr, F. (1978). *Akroriti-first maritime republic?* In: Doumas, C. (ed), Thera and the Aegean World I. London: Thera and the Aegean World, 423-428.

Schoch, M. (1995). *Die minoische Chronologie: Moglichkeiten und Grenzen konventioneller und naturwissenschaflicher Methoden, Meinz.*

Self, S. (1992). *Krakatau revisited: the course of events and interpretation of the 1883 eruption.* Geology Journal, 28.2, 109-121.

Siebert, L., Cottrell, E., Venzke, E., Andrews, B. (2015). *Earth's volcanoes and their eruptions: An overview*. In: Sigurdsson, H., Houghton, B., McNutt, S., Rymer, H., Stix, J. (Eds), The encyclopedia of volcanoes. Elsevier, 239-256.

Sigurdsson, H., Carey, S., Mandeville, C., and Bronto, S. (1991). *Pyroclastic flows of the 1883 Krakatau eruption*. EOS, 72, 377-392.

Sotirakopoulou, P. (1990). *The earliest history of Akrotiri: the Late Neolithic and Early Bronze Age phases*. In: Hardy, D. A. (ed), Thera and the Aegean World III, v. 3, London, The Thera Foundation, 41-48.

Sparks, R. S. J. (1979). *The Santorini eruption and its consequences*. Endeavour, 3, 27-31.

Sparks, R.S.J., and Wilson, C. J. N. (1990). *The Minoan deposits: a review of their characteristics and interpretation*. In: Hardy, D. A. (ed), Thera and the Aegean World III, v. 2: Earth Sciences: London, The Thera Foundation, 89-99.

Taddeucci, J., Edmonds, M., Houghton, B., James, M.R., and Vergniolle, S. (2015). *Hawaiian and Strombolian Eruptions*. In: Sigurdsson, H., Houghton, B., McNutt, S., Rymer, H., Stix, J. (Eds), The encyclopedia of volcanoes. Elsevier, 485-504.

Thorpes-Scholes (1978). *Akrotiri: Genesis, Life and Death*. In: Doumas, C. (eds) Thera and the Aegean World I, London, Thera and the Aegean, 437-449.

Vespa, M., Keller, J., and Gertisser, R. (2006). *Interplinian explosive activity of Santorini volcano (Greece) during the past 150,000 years*. Journal of Volcanology and Geothermal Research 153, 262-286.

Walker, G.P.L. (1971). *Grain-size characteristics of pyroclastic deposits*. Journal of Geology, 79, 696-714.

Walker, G.P.L (1973). *Explosive volcanic eruptions – a new classification scheme*. Geol Rundsch, 62, 431-446.

Warren, P.M. (2006). *The date of the Thera eruptions in relation to Aegean-Egyptian interconnections and the Egyptial historical chronology*. In: Czerny, E., Hein, I., Hunger, H., Melman, D., Schwab, A. (ed.) Timelines. Studies in Honour of Manfred Bietak. Leuven: Peeters, 305-321.

Warren, P.M. (2009). *The date of the Late Bronze Age eruption of Santorini*. In: Warburton, D.A. (ed.) Time's up! Dating the Minoan eruption of Santorini: Acts of the Minoan Eruption

Chronology Workshop, Sandbjerg, November 2007, Athens: Danish Institute at Athens, 181-186.

Weiner, M.H. (2009). *The state of debate about the date of the Theran eruption.* In: Warburton, D.A. (ed.) Time's up! Dating the Minoan eruption of Santorini: Acts of the Minoan Eruption Chronology Workshop, Sandbjerg, November 2007, Athens: Danish Institute at Athens,197-206.

Weiner, M.H. (2012). *Problems in the measurement, calibration, analysis, and communication of radiocarbon dates (with special reference to the prehistory of the Aegean world).* Radiocarbon, 54, 423-434.

Wilson, L. (1978). *Energetics of the Minoan Eruption*. In: Doumas, C. (eds) Thera and the Aegean World I, London, Thera and the Aegean, 221-228.